



423/259



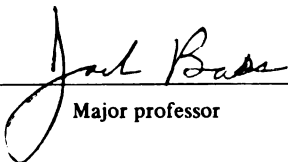
This is to certify that the  
thesis entitled  
THE MAGNETOTHERMOELECTRIC EFFECT IN SINGLE  
CRYSTAL ALUMINUM AND INDIUM AT LIQUID  
HELIUM TEMPERATURES

presented by

Barry Jay Thaler

has been accepted towards fulfillment  
of the requirements for

Ph.D. degree in Physics

  
Major professor

Date 9-14-77

THE MAGNETOTHERMOELECTRIC EFFECT  
IN SINGLE CRYSTAL ALUMINUM AND  
INDIUM AT LIQUID HELIUM TEMPERATURES

By

Barry Jay Thaler

A DISSERTATION

Submitted to  
Michigan State University  
in partial fulfillment of the requirements  
for the degree of

DOCTOR OF PHILOSOPHY

Department of Physics

1977

6107243

# ABSTRACT

## THE MAGNETOTHERMOELECTRIC EFFECT IN SINGLE CRYSTAL ALUMINUM AND INDIUM AT LIQUID HELIUM TEMPERATURES

By

Barry Jay Thaler

We have studied the effect of a transverse magnetic field  $H$  upon the low temperature absolute thermopower  $S$  of very dilute aluminum and indium based alloys. Measurements were carried out on single crystal samples at temperatures  $T$  between 1.5 and 5K and with magnetic field strengths up to 20kG. The aluminum measurements were performed on a sample grown along the [001] axis and containing 50 ppm gallium. The indium measurements were performed on several samples containing from 0 to 500 ppm added impurities, which were grown along several crystallographic axes.  $S$  of both metals consisted of both a component which was oscillatory with increasing magnetic field and a non-oscillatory component.

The non-oscillatory component of the aluminum sample was obtained for  $H$  along both the {010} and {110} families of axes. The data were consistent with the equation  $S(H,T) = A(H)T + B(H)T^3$ , allowing a separation of the electron diffusion component,



$S_d = A(H)T$ , from the phonon drag component,  $S_g(H) = B(H)T^3$ . This separation allowed determination of the quantity  $\Delta S_d = S_d(H \rightarrow \infty) - S_d(H = 0)$ . The average value of  $\Delta S_d$  for  $H$  along the crystallographically equivalent  $[100]$  and  $[010]$  axes was  $\Delta S_d = (2.23 \pm .25)T \times 10^{-8} \text{V/K}$ , in good agreement with both previous measurements on polycrystalline samples and with a calculation by Opsal and Wagner, provided that a 45% electron-phonon mass enhancement factor was included. For  $H$  along the  $\{110\}$  family of axes, a value of  $\Delta S_d = (2.0 \pm .2)T \times 10^{-8} \text{V/K}$  was obtained. This value is slightly lower than the average value of  $\Delta S_d$  along the  $\{010\}$  axes, in agreement with the calculation of Opsal and Wagner.

The non-oscillatory component of the indium data could not be unambiguously separated into electron diffusion and phonon drag components. It is concluded that this was principally due to the fact that our available temperature range was too close to the phonon drag peak. For  $T$  between 3 and 5K,  $S$  becomes more negative with increasing  $H$ . This is the antithesis of the aluminum data in this  $T$  range, and is due to  $S$  of indium being dominated by  $S_g$ . For  $T$  between 1.5 and 2.5K, the high field limit of  $S$  either gives strong evidence that it will become more positive than the lower field values or actually does become more positive. This is interpreted as showing that  $S_d$  is increasing relative to  $S_g$  with decreasing  $T$ .

The size of the oscillatory component of  $S$ ,  $S^{\text{osc}}$ , due to oscillations in the density of states at the Fermi energy is estimated for  $H$  along the  $[010]$  axis for both the  $\beta$ -orbit in aluminum and the neck orbit of the  $\beta$ -arms in indium. This estimate is several orders of magnitude smaller than the measured oscillation amplitudes of all large amplitude oscillations. We interpret this to mean that these oscillations are caused by magnetic breakdown, the only other mechanism expected to cause this oscillatory behavior.

For aluminum, the above interpretation is supported by the fact that independent magnetoresistance measurements strongly suggest that magnetic breakdown is present for  $H$  directed along the  $[010]$  axis. In addition,  $S^{\text{osc}}$  was largest for  $H$  along this axis, being an order of magnitude larger than the non-oscillatory component at 20kG. As  $H$  was rotated away from the  $[010]$  axis the oscillations decreased in magnitude, but persisted throughout the  $(001)$  plane. The oscillations had periods corresponding to those of the  $\beta$ -orbit. The field and temperature variations of the  $[010]$  oscillations were dominated by a term exponential in the ratio  $m^*(T + T_D)/H$ . Analysis using the de Haas-van Alphen procedure for determining effective masses and Dingle temperatures yields  $m^* = (0.093 \pm 0.01)m_e$  and  $T_D \approx 1-4\text{K}$ . This value of  $m^*$  agrees with the value obtained from

de Haas-van Alphen measurements for the same orbit, and corresponds to an electron-phonon mass enhancement of approximately 40%.

Large amplitude, low frequency oscillations in  $S$  were observed in indium below 2.5K for  $H$  between 10 and 20kG and directed along either the  $[010]$ ,  $[\bar{1}01]$ , or  $[1\bar{1}0]$  axes. The periods of these oscillations correspond with those obtained from de Haas-van Alphen measurements on the neck orbit of the  $\beta$ -arms of indium. Arguing by analogy, comparison of the  $[010]$  indium data with similar data for the  $[010]$  breakdown orbit in aluminum leads to the conclusion that these oscillations also arise from magnetic breakdown. This is the first evidence that there may be magnetic breakdown in indium.

TO MY PARENTS

## ACKNOWLEDGEMENTS

It is a great pleasure to acknowledge my thesis advisor Professor Jack Bass, whose suggestions and criticisms throughout the course of this research were invaluable. I would also like to thank Dr. Jon L. Opsal and Professor Robin Fletcher for numerous helpful discussions. The time donated by Dr. E.L. "Terry" Stone III and C.W. Lee in helping to make measurements is also gratefully acknowledged.

I am indebted to Z. Katsiapis for growing the Al(Ga) single crystal. Specific thanks go to Mr. B. Schumaker for preparing the alloys, and to D.R. Cady for helping with the many aspects of sample preparation. I would like to thank all the guys of the machine shop for all their design tips and help in constructing the various pieces of apparatus. I would also like to thank all the secretaries who have been associated with the Physics Department during my stay, especially the two SSMS secretaries Jean Strachan and Delores Sullivan for all their help. And last, but certainly not least, I'd like to thank Diane Spero for helping to type this thesis.

I would also like to acknowledge the financial support of the National Science Foundation.

## TABLE OF CONTENTS

	Page
List of Tables	vi
List of Figures	vii
I. INTRODUCTION	1
A. The Experimental Problem	1
B. Previous Work on the Magnetothermopower of Aluminum	2
C. The Present Thesis	4
II. EXPERIMENTAL TECHNIQUE	8
A. Voltage Measurement	8
1. Nulling Technique	8
2. Field Sweep Technique	10
B. Thermometry	14
C. Sample Preparation	20
D. Alloys	25
E. Crystal Growth	25
F. Experimental Procedure and Data Analysis	28
1. Nulling Technique Measurements of S, K, and R	28
2. Field Sweep Technique Measurements of S, K, and R	30
III. NON-OSCILLATORY THERMOELECTRIC PHENOMENA - THEORY	33
A. Electron Diffusion	33
1. General Relations	33
2. Electron-Phonon Mass Enhancement in $S_d$	40
B. Phonon Drag	48
IV. NON-OSCILLATORY THERMOELECTRIC PHENOMENA - EXPERIMENT	56
A. Aluminum	56
1. Introduction	56
2. Sample	59
3. Data and Analysis	59

	Page
3.1 Determination of the Non-Oscillatory Results	59
3.2 $\Delta A$ for H Parallel to [010] and [001]	62
3.3 $\Delta A$ for H Parallel to [011]	64
3.4 Effects of Magnetic Breakdown	65
3.5 Phonon Drag	66
4. Summary and Conclusions for Aluminum	69
B. Indium	70
1. Introduction	70
2. Data and Analysis	74
3. Umkehr effect	86
4. Summary and Conclusions for Indium	90
V. OSCILLATORY THERMOELECTRIC PHENOMENA - THEORY	92
A. Variation of the Density of States at $\epsilon_F$ with H	92
B. Estimate of S Oscillations due to Density of States Oscillations for Aluminum and Indium	95
C. Magnetic Breakdown	102
VI. OSCILLATORY THERMOELECTRIC PHENOMENA - EXPERIMENT	112
A. The Fermi Surfaces of Aluminum and Indium	112
B. Aluminum	114
1. Introduction	114
2. Experimental Procedure	116
3. Data and Analysis	116
3.1 H Parallel to [010]	116
3.2 H Along other Directions in the (100) plane	125
C. Indium	132
1. Introduction	132
2. Experimental Procedure	133
3. Data and Analysis	133
List of References	143
Appendix I : Calculation of Anisotropy of $\tau(\vec{k})$ for Al(Ga)	148
Appendix II: Determination of $\frac{\partial \sigma(\epsilon)}{\partial \epsilon}$	150

# LIST OF TABLES

Table		Page
II-1	Some characteristics of the samples used in this thesis	27
IV-1	Values of $B(H)$ for $Al(Ga)$	67
VI-1	Values of $m^*/m_e$ and $T_D$ for two orthogonal directions of the magnetic field $H$ and for different assumed values of $n$ for $Al(Ga)$	124
AI-1	Average reciprocal relaxation times for $Al(Ga)$ obtained from Sorbello's approximate phase shift model <sup>(7)</sup>	149



## LIST OF FIGURES

Figure		Page
II.1	The Superconducting Chopper-Amplifier System: a) The superconducting chopper-amplifier circuit; b) Schematic (actual size) of the device (after Averback <sup>(3)</sup> ).	9
II.2	The variation with magnetic field of the gain of an unshielded chopper-amplifier system	13
II.3	The variation with magnetic field of the gain of a shielded chopper-amplifier system	15
II.4	The Vacuum Chamber: A) lucite block, B) heat sink for resistor leads, C) sample, D) Glastic backing, E) carbon resistor, F) heater, G) cold sink (O.F.H.C. copper), H) binding post, I) flange for Pb O-ring, J) vacuum line, K) epoxy seal, L) support rod, M) vise clamp, N) sample support (brass) which is attached to the cold sink	18
III.1	$\epsilon$ vs. $k$ relations for free electrons (dashed curve) and for quasi-particles (solid curve)	46
III.2	The change of electron wavevector accompanying the annihilation of a phonon by a (a) Normal process, (b) Umklapp process (after Barnard <sup>(23)</sup> )	51
III.3	Schematic diagrams of sections through the 2 <sup>nd</sup> (upper) and 3 <sup>rd</sup> (lower) zones of Al showing electron-phonon scattering events (after Gripshover, et. al. <sup>(26)</sup> )	54

Figure		Page
IV.1	The variation of $S$ with magnetic field at 3.55K for the Al(Ga) sample. The magnetic field is directed along the [010] axis. The maxima and minima of the quantum oscillations are represented by circles, and the non-oscillatory component of $S$ is represented by the crosses	61
IV.2	The temperature dependence of the non-oscillatory component of $S$ of the Al(Ga) sample for: $H = 15\text{kG}$ and parallel to [010] (squares); $H = 15\text{kG}$ and parallel to [100] (triangles); $H = 15\text{kG}$ and parallel to [110] (crosses), $H = 0\text{kG}$ (circles). The full symbols indicate data obtained with $H$ reversed.	63
IV.3	The temperature dependence of the non-oscillatory component of $S$ for sample In(Ga) with $H$ directed along [010]	75
IV.4	The temperature dependence of the non-oscillatory component of $S$ for sample In(Ga) with $H$ directed along [001]	76
IV.5	The temperature dependence of the non-oscillatory component of $S$ for sample In(Sn)-II with $H$ directed along [001]	77
IV.6	The temperature dependence of the non-oscillatory component of $S$ for sample In(Sn)-II with $H$ directed along [110]	78
IV.7	The temperature dependence of the non-oscillatory component of $S$ for sample In(Sn)-I with $H$ rotated $12^\circ$ from the $[101]$ in the (101) plane	79
IV.8	The temperature dependence of the non-oscillatory component of $S$ for sample In(Sn)-III.	80
IV.9	The magnetic field dependence of $S$ for sample In(Sn)-II with $H$ directed along $[1\bar{1}0]$	81

Figure		Page
IV.10	The temperature dependence of the Lorenz ratio $L$ divided by the ideal Lorenz ratio $L_0$ for samples: A) In(Sn)-III, with $H$ directed along [001]; B) In(Sn)-II, with $H$ directed along [001]; C) In(Ga), with $H$ directed along [010]	84
IV.11	Variation of $S$ with rotation angle $\theta$ at $H = 10\text{kG}$ and $T = 4.7\text{K}$ for sample In-I. $H$ was rotated about the [101] axis. $\theta = 213^\circ$ corresponds to $H$ directed along [010]	87
IV.12	Variation of $R$ (upper curve) and $S$ (lower curve) with rotation angle $\theta$ at $H = 10\text{kG}$ for sample In(Sn)-I. $H$ was rotated about the [101] axis. $\theta = 202^\circ$ corresponds to $H$ directed along [010]. The $R$ curve was measured at $4.2\text{K}$ and the $S$ curve at $4.3\text{K}$	88
V.1	Variation of the Fermi surface with field, showing the increasingly spherical shape as the field becomes weaker. The field decreases going (a) to (d) (after Adams and Holstein <sup>(43)</sup> )	93
V.2	(a) Free electron orbit in a magnetic field. (b) In the periodic potential of the lattice, the orbits are reconnected at the zone boundary; but in a strong magnetic field may jump back to the free electron path (after Ziman <sup>(61)</sup> )	104
V.3	Ashcroft's 4-OPW pseudopotential model for the electron-like 3 <sup>rd</sup> zone of the Fermi surface of aluminum (after Abele and Blatt <sup>(62)</sup> )	106
V.4	Central [100] section through the aluminum Fermi surface (after Ashcroft <sup>(63)</sup> )	107
VI.1	(a) The Brillouin zone for face-centered tetragonal indium; (b) the indium free-electron model hole surface; (c) the indium third zone electron $\beta$ -arm surface (after Hughes and Shepherd <sup>(52)</sup> )	113

- VI.2 The variation of  $S$  with magnetic field at  $T = 3.55\text{K}$  for the  $\text{Al}(\text{Ga})$  sample.  $H$  is along the  $[010]$  axis. The solid line labeled  $S = 0$  represents the x-y recorder output when there is no applied temperature gradient. The broken line indicates the non-oscillatory component of  $S$ . The oscillating curve represents raw data, uncorrected for a field dependent amplification of the measuring system. The magnitude of this correction is indicated by the manner in which the  $S = 0$  curve and the broken line approach each other as  $H$  increases. When the data are corrected, these two curves are equidistant at all fields above about  $11\text{kG}$  to within experimental uncertainty 117
- VI.3 The variation of the quantity  $H^{3/2}S^{\text{osc}}/T$  (plotted on a logarithmic scale) with  $H^{-1}$  for a series of temperatures for sample  $\text{Al}(\text{Ga})$ .  $H$  was directed along  $[010]$  120
- VI.4 The variation of the quantity  $S^{\text{osc}}/T$  (plotted on a logarithmic scale) with  $H^{-1}$  for a series of temperatures for sample  $\text{Al}(\text{Ga})$ .  $H$  was directed along  $[010]$  121
- VI.5 The variation of the quantity  $H^{-3/2}S^{\text{osc}}/T$  (plotted on a logarithmic scale) with  $H^{-1}$  for a series of temperatures for sample  $\text{Al}(\text{Ga})$ .  $H$  was directed along  $[010]$  122
- VI.6 The variation with temperature of the slopes of the lines shown in Figure VI.4 for  $H$  parallel to  $[010]$  (circles) and of similar slopes of similar lines for  $H$  parallel to  $[100]$  (triangles). The upright triangles represent initial measurements with  $H$  parallel to  $[100]$ . To evaluate the effects of changes in sample treatment and alignment, after these initial measurements were completed the sample was removed from the holder, its potential leads

Figure		Page
	were removed, it was reannealed, the potential leads were reattached and the sample was returned to the holder. The resulting data are indicated by inverted triangles	123
VI.7	The variation of S with magnetic field at $T = 2.4\text{K}$ for the Al(Ga) sample. H is rotated $20^\circ$ from the [010] axis in the (001) plane. The solid line labeled $S = 0$ represents the x-y recorder output when there is no applied temperature gradient. The oscillatory curve represents raw data, uncorrected for the field dependent amplification of the measuring system	126
VI.8	The variation of S with magnetic field at $T = 2.8\text{K}$ for the Al(Ga) sample. H is along the [110] axis. The solid line labeled $S = 0$ represents the x-y recorder output when there is no applied temperature gradient. The oscillating curve represents raw data, uncorrected for the field dependent amplification of the measuring system	127
VI.9	The variation of S with magnetic field at $T = 2.3\text{K}$ for H along a series of directions in the (001) plane of the Al(Ga) sample. $0^\circ$ corresponds to H directed along [100]	129
VI.10	Variation of the oscillation period of the third zone $\beta$ -orbit with rotation angle in the (001) plane. This figure displays our present magnetothermopower data, the de Haas-van Alphen data of Larson and Gordon, (32) and the results of a pseudo-potential calculation by Ashcroft (63)	130
VI.11	The magnetic field dependence of S for H aligned along the indicated crystallographic axes. The lines labeled $S = 0$ represent the recorder output when there is no applied temperature gradient. The oscillating curves represent raw data, uncorrected for the field dependent	

Figure		Page
	amplification of the measuring system. The amplification decreases by about 30% over the field range shown. The curves for H aligned along $[101]$ and $[010]$ are from sample In(Sn)-I and the curve for H along $[110]$ is from sample In(Sn)-II	134
VI.12	The variation of the quantity $HS^{\text{osc}}/T$ (plotted on a logarithmic scale) with $1/H$ for sample In(Sn)-I at $T = 1.67\text{K}$ . H was directed along $[010]$	136
VI.13	Variation of S with rotation angle measured from the $[010]$ axis, at $H = 15\text{kG}$ for aluminum and indium single crystals. The aluminum data are from sample Al(Ga). The indium data for H rotated about the $[001]$ axis are from sample In-II and the data for H rotated about the $[101]$ axis are from sample In(Sn)-I	140

## I. INTRODUCTION

### A. The Experimental Problem

Thermoelectric effects are usually classified in one of three categories: the Seebeck, Peltier; or Thomson effects. However, all three effects are related by the Kelvin-Onsager Relations,<sup>(1)</sup> and therefore provide equivalent information. The experiments forming the basis of this thesis are measurements of the Seebeck effect. This effect is characterized by the generation of an electric field  $\vec{E}$  by means of a temperature gradient  $\vec{\nabla}T$  which is applied along an electrically isolated sample. Using dyadic notation,<sup>(2)</sup> the thermopower tensor  $\overleftrightarrow{S}$  is defined as

$$\overleftrightarrow{S} = \vec{E} (\vec{\nabla}T)^{-1} . \quad (I.1)$$

Since  $\vec{E} = -\vec{\nabla}V$ , we may write

$$\overleftrightarrow{S} = -\vec{\nabla}V(\vec{\nabla}T)^{-1} . \quad (I.2)$$

This is equivalent to

$$\overleftrightarrow{S} = -\hat{i} \frac{dV}{dT} \hat{j} \quad (I.3)$$

where  $\hat{i}$  and  $\hat{j}$  are unit vectors in the directions of the voltage and temperature differences respectively.

Since measurements are performed over paths of finite length, the experimentally measured thermopower,  $\vec{S}_{\text{exp}}$ , is defined as

$$\vec{S}_{\text{exp}} = -\hat{i} \frac{\Delta V}{\Delta T} \hat{j}$$

where  $\Delta V$  and  $\Delta T$  are measured voltage and temperature differences. If  $\Delta T \cong dT$  then  $S \cong S_{\text{exp}}$ ; this may be attained when  $\Delta T \ll T$ . Since the present measurements were performed at temperatures between 1.5 and 5K, temperature differences of approximately 0.1 to 0.3K were used. A typical value of  $S$  for aluminum or indium is  $10^{-8}$  V/K, which implies that  $10^{-8} - 10^{-9}$  V must be measured. To make measurements with 1% accuracy required a voltage sensitivity of  $10^{-10} - 10^{-11}$  V. This is not a trivial task in the presence of a large magnetic field (20kG.). However this problem can be solved by using a superconducting chopper-amplifier.

#### B. Previous Work on the Magnetothermopower of Aluminum

The thermopower is the most difficult transport property of a metal to properly calculate. A major reason for this is that thermopower is the transport property which is most sensitive to the details of the scattering processes. However, Averback found a property of the electron-diffusion component  $S_d$  of the thermopower of



aluminum which was insensitive to the scattering details and depended only on the host metal.<sup>(3,4)</sup> Using a number of polycrystalline samples of very dilute aluminum alloys, he showed that although both the zero field and high field values of  $S$  (note that  $S$  saturates in the high field limit for aluminum or any other uncompensated metal with no open orbits) varied from sample to sample, the difference between these two values,  $\Delta S_d = S_d(H \rightarrow \infty) - S_d(H = 0)$ , was approximately constant -- for all samples  $\Delta S_d/T$  varied between  $2.1 - 2.6 \times 10^{-8} \text{V/K}^2$ .

Averback and Wagner<sup>(5)</sup> calculated  $\Delta S_d$  using no adjustable parameters and obtained the value  $\Delta S_d/T = 1.6 \times 10^{-8} \text{V/K}^2$ , about 30% smaller than experiment. Some possible sources of this 30% discrepancy are:

- (1) The measurements were performed on polycrystalline samples, while the calculation is appropriate for  $H$  directed along a four-fold symmetric axis of a single crystal.
- (2) The impurities in the samples might have been anisotropic scatterers in aluminum, while the calculation assumed isotropic scattering.
- (3) The 1-OPW Fermi surface used by Averback and Wagner in their calculation might be inappropriate for comparison with experiment.
- (4) The effects of mass enhancement were not included in Averback and Wagner's calculation.

(Averback and Wagner neglected effects of electron-phonon mass enhancement because Prange and Kadanoff<sup>(6)</sup> had claimed that such effects were not present in the electronic properties of metals.)

### C. The Present Thesis

This thesis began as an attempt to measure the transverse magnetothermopower of an aluminum sample which satisfied the requirements of the calculation of  $\Delta S_d$  made by Averback and Wagner. We hoped that such measurements would isolate the source of the discrepancy between theory and experiment.

A single crystal foil, oriented so that the magnetic field could be directed along either a four-fold symmetric [010] crystallographic axis or a two-fold symmetric [110] axis, was used. This crystal contained 50ppm Ga, an impurity which should be a nearly isotropic scatterer in aluminum.<sup>(7)</sup> The data obtained for  $\Delta S_d$  with this single crystal are compared below with the data from polycrystalline samples reported by Averback, et. al.;<sup>(4)</sup> with the calculation of Averback and Wagner;<sup>(5)</sup> with an improved, 4-OPW version of this same calculation by Opsal and Wagner<sup>(8)</sup> which was stimulated by the experimental results to be described; and, finally, with the Opsal and Wagner calculation including the effects of mass enhancement.<sup>(8)</sup>

The results obtained with this aluminum single crystal stimulated us to extend magnetothermopower measurements to indium single crystals to see whether  $\Delta S_d$  behaved the same as in aluminum. It was anticipated that such measurements would be interesting because although aluminum and indium are both Group III metals, they crystallize with different structures; aluminum in a face centered cubic (FCC) structure, and indium in a face centered tetragonal (FCT) structure. The slight tetragonal distortion of indium causes some axes which are four-fold symmetric in the FCC structure to be only two-fold symmetric in the FCT structure. Thus indium would allow a study of the effects of this small distortion on  $\Delta S_d$ . Unfortunately, this study yielded results which did not allow the electron-diffusion component of the magnetothermopower to be unambiguously separated from the phonon drag component. The indium data will be presented and will be analyzed to determine the source of this lack of separation. Some indium samples exhibited a significant magnetothermopower umkehr effect; this will also be discussed.

In the process of making the aforementioned studies, giant quantum oscillations were discovered in both metals for  $H$  along a number of crystallographic directions. For  $H$  along the  $[010]$  axis in aluminum these oscillations could easily be distinguished from the noise for  $T$  between 1.7 and 4.8 K; therefore the temperature dependence of the

oscillation amplitudes was systematically studied. In indium the oscillations could only be distinguished from the noise for  $T$  between 1.5 and 2.5 K; therefore an oscillation amplitude study similar to that performed for the [010] direction in aluminum was not attempted. The experimental results will be compared with theories which predict oscillatory behavior. Also, the periods of the magnetothermopower oscillations will be compared with the same periods obtained from independent magnetoresistance or de Haas-van Alphen measurements.

The remainder of the thesis is organized as follows:

Section II provides a description of the experimental apparatus and measurement techniques.

Section III furnishes the theoretical background for the calculation of magnetothermopower. Particular emphasis is placed on the role of electron-phonon mass enhancement in thermoelectricity. In section IV the experimental results for the non-oscillatory component of the magnetothermopower for both aluminum and indium, are presented.

Section V presents the theory of the oscillatory component of the magnetothermopower. These oscillations can be caused by either oscillations in the density of states at the Fermi level, or by magnetic breakdown. Both of these pictures are developed. A simplistic calculation

is used to estimate the magnetothermopower oscillation amplitude expected from oscillations in the density of states. In section VI the experimental data for the oscillatory component of the magnetothermopower of both aluminum and indium are presented and compared with the simple calculation.

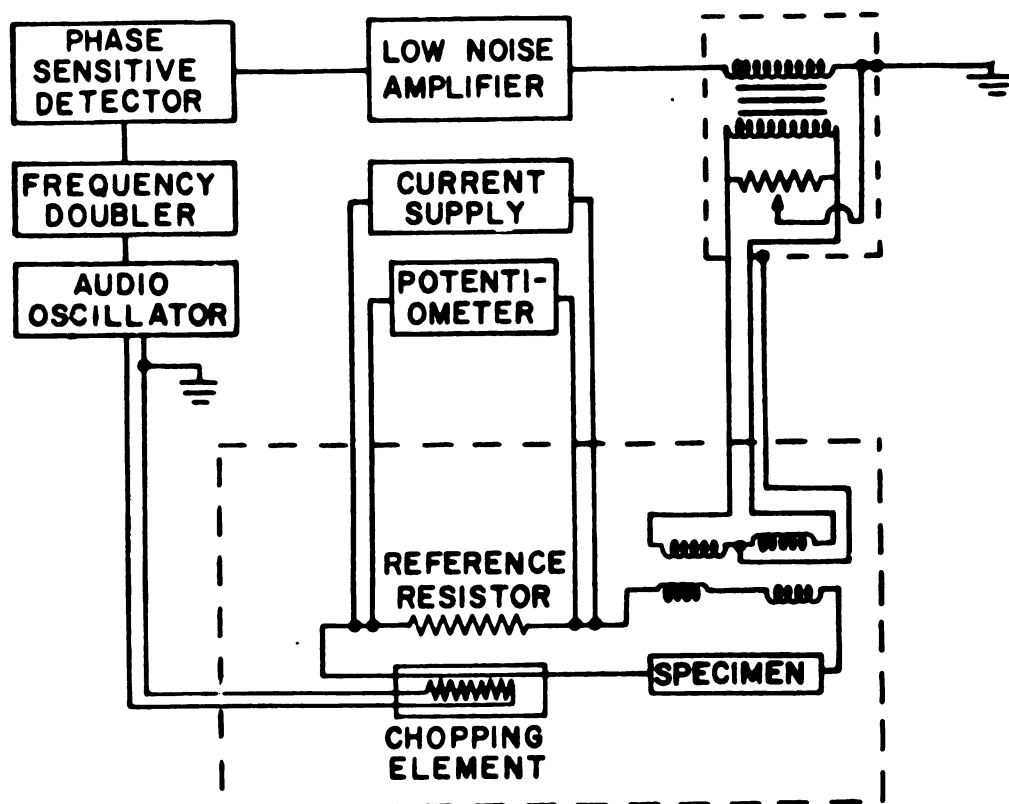
## II. EXPERIMENTAL TECHNIQUE

### A. Voltage Measurement

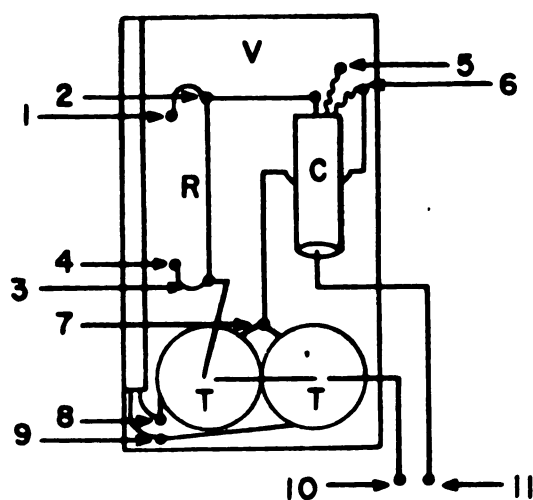
The voltage measuring system is shown in Figure II.1. This chopper-amplifier system was designed and described in detail by R.S. Averbach.<sup>(3)</sup> In view of this, only the techniques of voltage measurement will be described in this thesis. The system was operated in two modes: (1) At steady magnetic fields the signal generated by the sample was nulled out, using the chopper-amplifier as null detector, (2) In continuously varying magnetic fields the signal generated by the sample was directly measured using the chopper-amplifier as a linear amplifier. Operation in the first mode will be described in the next section entitled "Nulling Technique". Operation in the second mode will be described in the section entitled "Field-Sweep Technique".

#### 1. Nulling Technique

As can be seen from Figure II.1, the chopper-amplifier system contains a reference resistor which is in the liquid helium bath. This reference resistor was a small segment of copper wire having a resistance of about  $8\mu\Omega$ , which remained constant to within our ability to measure it ( $< 2\%$ ) at all temperatures and fields employed in these measurements.



(a)



(b)

- |        |                    |
|--------|--------------------|
| 1, 4   | Current Leads      |
| 2, 3   | Potential Leads    |
| 5      | Oscillator Lead    |
| 6, 7   | Ground             |
| 8, 9   | Secondary Leads    |
| 10, 11 | Sample Leads       |
| R      | Reference Resistor |
| T, T   | Transformers       |
| C      | Chopping Element   |
| V      | Vector Board       |

**Figure II.1: The Superconducting Chopper-Amplifier System:**  
a) The superconducting chopper-amplifier circuit; b) Schematic (actual size) of the device (after Averback<sup>(3)</sup>).

When a known current (produced by a series of 12V dry cell batteries) is passed through the reference resistor, a known voltage is generated in the chopper-amplifier circuit. This voltage is used to null out the voltage which is being generated by the sample. At null condition there will be no net current flowing in the circuit, so the panel meter (output) of the phase sensitive detector will show no deflection. The accuracy of the technique is limited by the circuit noise, which appears as a small oscillation of the needle of the panel meter. Using a time constant of 3 seconds on the phase sensitive detector (PAR model JB-4), this noise was usually  $2 - 4 \times 10^{-11} \text{V}$  in zero field and increased to  $1 - 3 \times 10^{-10} \text{V}$  at 20kG.

## 2. Field Sweep Technique

At all magnetic fields used in these experiments the output of the chopper-amplifier system was quite linear (to within 2%). So after independently calibrating the panel meter, the voltage generated by the sample was measured by reading the deflection of the needle of the panel meter. The panel meter was calibrated by passing a known current through the reference resistor under conditions where the sample was not generating a voltage, and then measuring the resulting deflection of the needle.

In addition to monitoring the output of the phase sensitive detector on the panel meter, the analog output



was fed directly into the y-axis input of an x-y recorder (HP model 7004B). Sweeping the magnetic field at a constant rate and feeding the analog output of the Hall probe gaussmeter (F.W. Bell model 660) into the x-axis, resulted in a continuous recording of the voltage generated by the sample as a function of  $H$ . Since a changing magnetic field induces a voltage within our measuring system, the magnetic field had to be swept up twice - once with the sample generating a voltage, and once with it generating zero voltage (to define a zero voltage baseline). The difference between these two lines gives the voltage generated by the sample. Data taken using this field sweep method agreed with data taken independently using the nulling technique. The field sweep technique is advantageous for recording data when the voltage generated by the sample varies rapidly with field (e.g. giant quantum oscillations).

There are two reasons why it is important not to sweep the field too rapidly:

- (1) If the field is swept at a rate such that the thermally induced voltages are changing faster than the time constants allow the circuit to respond, then the voltage variations will be smoothed out (i.e. reduction of amplitude of the quantum oscillations).
- (2) If the field is swept too fast, the voltage induced by the changing magnetic field may

cause a component of the voltage measuring system to saturate, thus giving "false" data.

The field sweep technique has some disadvantages compared to the nulling technique:

- 1) The field sweep technique offers less accuracy because the quantity of interest must be obtained by taking the difference between two lines on a recording, each of which contains noise. Additionally there may be slow variations in both the signal and the zero baseline which lead to systematic errors. Comparisons between equivalent data suggest that the field sweep technique is about a factor of three less accurate than the nulling technique.
- 2) A second problem with the field sweep technique is that the gain of the chopper-amplifier system is field dependent (at 20kG the gain can be as much as 50% less than at 10kG). Figure II.2 shows a typical field dependence of the amplification of the system. The raw data must be corrected for this field dependent gain.

Toward the end of the present thesis research, the effect of shielding the chopper-amplifier with 5 mil thick lead foil was investigated. When the shielding extended from above the chopper-amplifier to about 8cm below

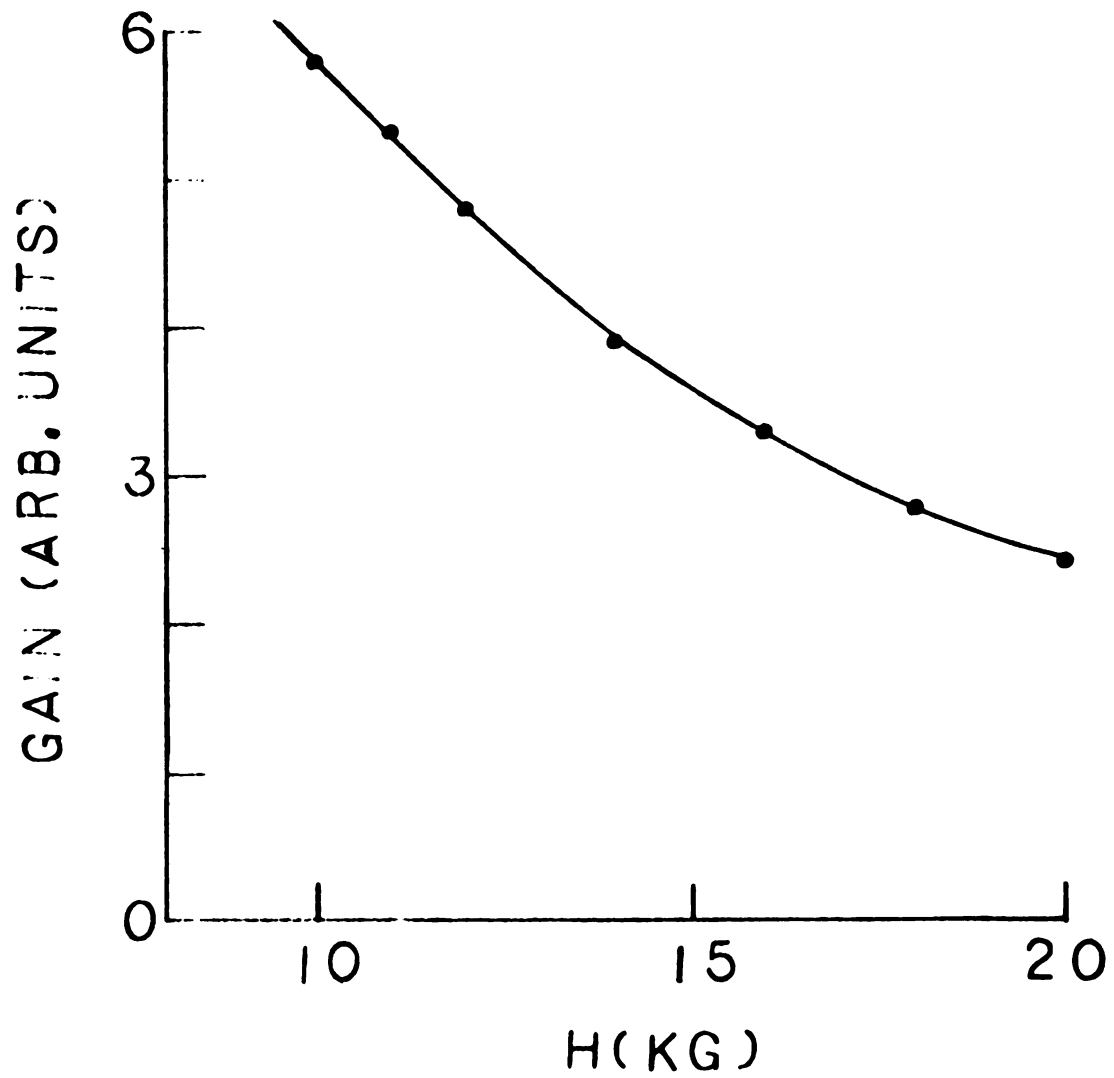


Figure II.2: The variation with magnetic field of the gain of an unshielded chopper-amplifier system.

it, the amplification factor only decreased about 10% between 10kG and 20kG, rather than the 50% obtained previously. Figure II.3 shows the field dependence of the amplification factor of a shielded chopper-amplifier system. Note that this field dependence is linear over a larger portion of the region between 10 and 20kG than it was for unshielded chopper-amplifier (see Figure II.2).

#### B. Thermometry

The temperatures of the thermocouple junctions were obtained using standard carbon resistance thermometry techniques. Nominal 100 ohm, 1/8 watt Ohmite resistors were used. These resistors are highly temperature sensitive between 1.5 and 5K, and they also have a low magnetoresistance for  $H < 20\text{kG}$ . This combination of properties makes these resistors quite satisfactory for use as thermometers.

The resistance of the carbon resistors was measured with an a.c. Wheatstone bridge.<sup>(9)</sup> The off balance signal was detected by a phase sensitive detector (PAR model HR-8). This technique had a resolution of about 0.1 ohms ( $\sim 0.0004\text{K}$  at 5K and less than  $0.0001\text{K}$  at 2K).

The circuit was arranged so that  $R_C$  (the resistance of the resistor at the cold end of the sample) and  $\Delta R$  ( $\Delta R = R_C - R_H$ , where  $R_H$  is the resistance of the resistor at the hot end of the sample) could be alternately

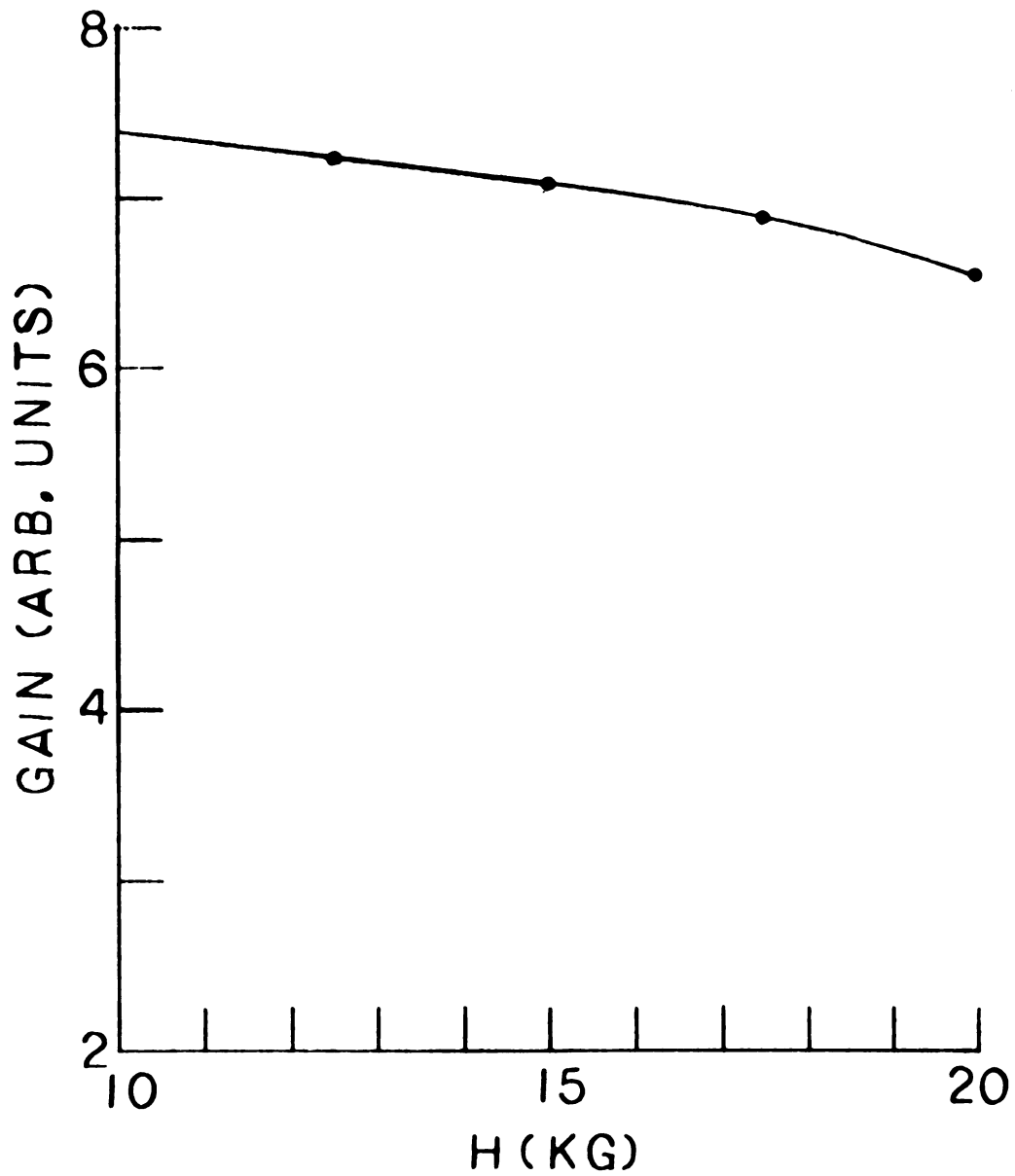


Figure II.3: The variation with magnetic field of the gain of a shielded chopper-amplifier system.

measured. From these two measurements,  $R_C$  and  $R_H$  could be deduced. As a check against self-heating, the power level of the phase sensitive detector (current source of the bridge) was varied, and the level which gave the same measured resistance as the next lower level was used.

The carbon resistors were calibrated below 4.2K against a pumped helium bath. The vapor pressure was measured by a mercury manometer, which was mounted with a silvered scale backing. The pressure could be read with an accuracy of 0.2 - 0.3 mm Hg. These pressures were corrected for hydrostatic head pressure and for the temperature dependence of the mercury density. The pressure vs. temperature relationship and the aforementioned pressure corrections were obtained from the National Bureau of Standards 1958 tables. The helium bath temperature was controlled by a Walker Manostat, which controlled to better than 0.001K above 2.5K and also between 2.0K and the  $\lambda$ -point of the liquid helium. Between the  $\lambda$ -point and 2.5K the system was somewhat less stable, presumably due to bubbling on the vacuum can surface.<sup>(3)</sup> Below 2K the pressure difference across the diaphragm of the Walker Manostat was not large enough to completely close off the pumping line; thus the temperature normally decreased slowly while the Walker Manostat was trying to control the bath temperature.

The carbon resistors were calibrated every time the cryostat was cooled, by fitting their resistances to

the equation: <sup>(10)</sup>

$$\ln R = m \left( \frac{\ln R}{T} \right)^{\frac{1}{2}} + b . \quad (\text{II.1})$$

For 100Ω Ohmite resistors, typical values of m and b were 2.31 and 4.25 respectively. The temperature could be obtained for any R by simply inverting eq. (II.1). The calibrations were usually limited to a range of about 1K. The "goodness of fit" was checked by substituting the calibration resistances into the inverse of eq. (II.1) to obtain the temperature corresponding to that resistance. The calculated temperature rarely deviated from the calibration temperature by more than 0.002K, and quite often deviated by less than 0.001K. To obtain temperatures between 4.2K and 5K, the calibration for the ranges 3.4 to 4.2K or 3.6 to 4.2K was simply extrapolated to higher temperatures. Earlier measurements using a calibrated germanium thermometer demonstrated that this procedure introduced no significant error up to about 5K. <sup>(4)</sup>

It is well known that at a given temperature the resistance of a carbon resistor slowly drifts with time. A simple method was used to correct for this drift. Before this correction is described, it would be beneficial to review the placement of heaters on the sample. Figure II.4 shows that two heaters are attached to the sample - one at either end. Aside from the connection of one end

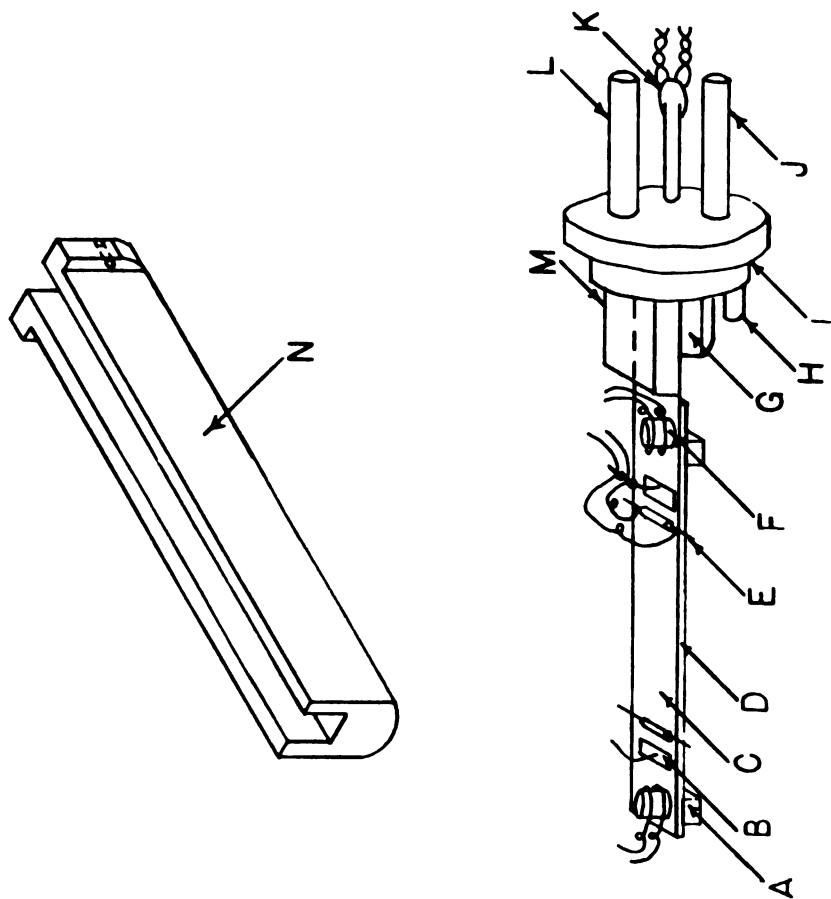


Figure II.4: The Vacuum Chamber: A) lucite block, B) sample, C) glastic backing, D) binding post, E) flange for Pb O-ring, F) carbon resistor, G) heater, H) vacuum line, I) sample support (brass) which is attached to the cold sink, J) sample support (brass) which is attached to the cold sink, K) epoxy seal, L) support rod, M) vise clamp, N) sample support (brass) which is attached to the cold sink.



of the sample to a cold sink, which is in direct contact with the helium bath, the sample is thermally isolated. The end of the sample attached to the cold sink will be called the "cold" end and the other end will be called the "hot" end. When the heater at the "hot" end of the sample (the "hot" heater) is turned on, a temperature gradient is produced along the sample; this also causes the temperature of the sample at the position of the "cold" resistor to be higher than the bath temperature. After measuring  $R_c$  and  $\Delta R$  the "hot" heater is turned off and the "cold" heater is turned on. The "cold" heater heats the sample to a uniform temperature. The heating power of the "cold" heater is adjusted so that  $R_c$  has the same value as when the sample was heated only by the "hot" heater.  $R_c$  and  $\Delta R$  are measured. The inverse of eq (II.1) is used to calculate the temperature at either end of the sample, and therefore  $T$  is determined. If the resistance of the two resistors drifts with time this drift should show up as a false temperature difference when only the "cold" heater is on. By subtracting this false temperature difference from the temperature difference obtained using only the "hot" heater, the correct  $\Delta T$  is determined. The false temperature difference was usually less than 5% for temperature differences greater than 0.03K.

If the sample is not completely isolated, the "cold" heater will produce a real temperature difference,

which should be indicated by a thermally induced voltage. In our measurements, such voltages were typically about 1% of those produced by the "hot" heater. It was therefore concluded that the real temperature difference produced by the "cold" heater was about 1% of that produced by the "hot" heater.

### C. Sample Preparation

Figure II.4 shows how the measuring probes and other apparatus were mounted on a sample. In order to have enough surface area to accommodate all these elements and also to maintain a sufficiently large temperature difference, the samples were about 7cm long, and 2 to 5mm wide. The following procedure was utilized to quickly mount the elements on the sample while introducing a minimum of cold work.

First the potential and current leads were attached. These leads were 3 mil copper-clad NbTi wire, chosen because NbTi remains superconducting at all temperatures and magnetic fields employed in these experiments. For aluminum samples, the leads were spotwelded on. In preparation for spotwelding, the sample was glued to a template using Duco Cement. The insulation and copper-cladding were removed from both ends of each NbTi wire. The leads were then varnished, using G.E.-7031 varnish, to the sample, so that one end of each lead was in position for attachment. The leads ran from these points

to the center of the sample from where each pair of leads was twisted tightly together as it led away from the sample.. The potential and current leads were then spot-welded to the aluminum sample. The sample was removed from the template by soaking in an acetone bath, and then glued to a Glastic backing, again using Duco Cement. Glastic was chosen as a backing material because it is an insulator whose thermal expansion is similar to that of a metal.

Since indium is a much softer material than aluminum, the potential and current leads were either "acid-welded" or soldered to the indium samples; this avoided the damage to the sample inherent in spotwelding. Indium has the property that when the surface is well cleaned with hydrochloric acid, it will bond to another indium surface which has been similarly prepared. This permitted NbTi leads which had been previously "wetted" with indium to be "acid-welded" to the sample. Alternatively the leads could easily be soldered to the indium samples using Rose's metal and Superior #30 liquid soldering flux. Tests showed that the data were the same for both methods of lead attachment. For both of these methods the copper-cladding was not removed from the lead ends which were to be attached to the sample. This was done because it was much easier to "wet" the copper-cladding with either indium or solder than it was to "wet"

NbTi. Since tests showed that the thermopower of indium with either method of lead attachment was zero (to within experimental uncertainty), when the indium was in the superconducting state, it is concluded that the copper-cladding did not introduce any measurable spurious voltages. Since the potential and current leads were not spotwelded to the indium samples, these samples could be glued to the Glastic backing before the leads were attached to the sample.

Once the leads were attached and the sample mounted on the Glastic, the sample was placed in a brass sample holder which held the sample parallel (to within  $1^\circ$ ) to the magnet pole pieces. The sample was isolated from the brass holder by 2 small lucite blocks, one at either end of the sample. These blocks were varnished between the Glastic and the brass holder using G.E.-7031 varnish. In the case of aluminum, one end of the sample was then mechanically clamped to the cold sink. In the case of indium, a small piece of very pure indium with about the same cross-sectional area as the sample was clamped to the cold sink, and the end extending from the clamp was melted and attached to one end of the sample. This was done to avoid the strains which would be introduced if the indium single crystal were directly clamped to the cold sink.

The other ends of the potential and current leads were then spotwelded to permanent leads which ran out of the sample chamber through an epoxy seal (which was constructed in accordance with the procedure outlined by Anderson<sup>(11)</sup>). Since the insulation and copper cladding had already been removed from the last centimeter or so of these ends, only the superconductor, NbTi, remained. Superconductors are poor thermal conductors, and therefore these leads shouldn't provide a significant heat leak. This was verified by the fact that the thermal emf generated when the sample was heated only with the "cold" heater, was typically 1% or less of that generated by the "hot" heater.

Next the carbon resistors and heaters were mounted. The insulation on the carbon resistors was ground off on one side. Cigarette paper saturated with G.E.-7031 varnish provided electrical insulation between the resistor and sample, and the varnish held the resistor in place. The leads to the resistors were 3 mil. manganin wire. To prevent large heat leaks through these leads, the manganin wires were attached to a small heat sink at a temperature within 0.01 to 0.02K of each carbon resistor before being brought out to connections external to the sample. These small heat sinks were made by varnishing several turns of the manganin wire to copper posts which were either varnished to the aluminum samples or soldered (using Cerrolow

#117 solder) to the indium samples, about 0.5cm from the carbon resistors.

The heaters were constructed by wrapping about 500 $\Omega$  of Evanohm wire ( $\sim 13\Omega/\text{cm}$ ) around a copper post and varnishing the wire to the post. The copper post was then attached to the sample in the same manner as the heat sinks. The heaters were operated using a d.c. current of 1 to 10mA.

The several leads from the heaters and resistors were soldered to permanent leads on a vector board which was mounted on the brass sample holder. The permanent resistor leads were 3 mil. managanin wire and the permanent heater leads were 38 awg. copper wire. All these leads entered the sample chamber via the vacuum line and were heat sunk by varnishing them to a copper post which was tightly screwed into the main frame of the cryostat (which was in contact with the helium bath).

Finally, the brass vacuum can was attached. The seal between the can and the sample chamber was made by squashing a Pb + 0.05%As O-ring between the can and the sample chamber with 12, 2-56  $\times$  3/8" stainless steel Allen head screws. The O-ring was made by wrapping Pb + 0.05%As wire, which had already been greased with Apiezon M grease, around the flange (see Figure II.4) and twisting it tight. Not a single O-ring prepared in this manner leaked. A few times tempered steel (black) screws were

substituted for the stainless steel screws. In almost every instance these seals leaked at 4.2K.

This entire sample preparation procedure could be completed in 1-2 days. This procedure was conceived to introduce a minimal amount of cold work to the rather delicate samples.

#### D. Alloys

Both the aluminum and indium alloys were mixed by Mr. B. Shumaker, using the procedure described by R.S. Averback.<sup>(3)</sup> The only difference in procedure was that the indium master alloys were prepared with a concentration of about 1% solute material. The "pure" aluminum was 69 grade aluminum supplied by Cominco Inc. The "pure" indium was either 69 grade indium supplied by Cominco Inc. or 59 grade indium supplied by the Indium Corporation of America. The solute materials, gallium and tin, were 69 grade. The aluminum alloys were rolled into 20 mil. thick foils, while the indium alloys were rolled into rods with a 2mm square crosssection.

#### E. Crystal Growth

The Al(Ga) single crystal was grown by Z. Katsiapis using a strain anneal technique.<sup>(12,13)</sup> Before mounting, the single crystal was annealed in air for 1 hour at 400C.

The indium crystals were grown in an atmosphere consisting of 90% argon and 10% hydrogen using a simple zone refiner and seeds of known crystallographic orientation. First the indium alloy and seed were placed in a crucible made from spectroscopically pure carbon. A heat lamp housed in an elliptical reflector was used to produce a molten zone about 1.5 to 2.5cm. long. The molten zone was first produced at the unseeded end of the indium alloy. This zone was then slowly moved along the entire length of the alloy until a small portion of the seed melted. The zone was then moved slowly away from the seed back along the entire length of the alloy. This two-pass procedure was adopted with the intention of achieving a homogeneous impurity distribution, since an odd number of passes is expected to produce an impurity concentration gradient along the sample. Once grown, the indium single crystals were not further annealed. During initial trials the indium sometimes separated into two pieces within the molten zone. This problem was eliminated by completing the etching (using concentrated HCl) and rinsing (using double distilled H<sub>2</sub>O followed by methyl alcohol) procedure between 5 and 10 minutes before the indium was placed in the crucible. The crucible was then immediately placed in a tube which was evacuated so that the argon-hydrogen atmosphere could be introduced.



All samples were characterized by X-ray (Laue) pattern analysis. Table II-1 shows the intended impurity concentration, the measured resistance ratio, RRR ( $R(300K)/R(4.2K)$ ), and the crystallographic axis along which the crystal was grown, for all crystals used in this thesis.

TABLE II-1: Some characteristics of the samples used in this thesis

SAMPLE	Nominal Impurity Conc.	RRR	Orienta- tion	Misori- enta- tion
Al (Ga)	50 ppm	1,400	[001]	< 1°
In-I	0	15,400	[101]	2°
In-II	0	4,350	[001]	3°
In (Ga)	50 ppm	7,400	[100]	-
In (Sn)-I	50 ppm	2,300	[101]	3°
In (Sn)-II	100 ppm	1,650	[110]	2°
In (Sn)-III	500 ppm	390	[110]	2°

The rather high RRR of the In(Ga) sample indicates that considerably less than 50 ppm gallium was in solution.

Single crystals were considered satisfactorily oriented when the crystallographic axis along which the sample was grown lay within a few degrees of the sample axis. The misorientation was determined from X-ray pattern analysis. The misorientation for each sample is also given in Table II-1. Since the sample holder aligned

the sample axis (not the crystallographic axis) transverse to the magnetic field, the magnetic field could not be aligned exactly along the crystallographic axes. However, in the interest of simplicity, the magnetic field will be referred to as being aligned along a given crystallographic axis when it was aligned as closely as possible to that axis.

#### F. Experimental Procedure and Data Analysis

##### 1. Nulling Technique Measurements of S, K, and R

Thermopower measurements using the chopper-amplifier as a null detector were performed in the following manner. The measurements were always begun with the helium bath at 4.2K. The "hot" heater was turned on, producing a temperature gradient along the sample, and the power was recorded. Within a few seconds the sample reached a steady state condition, and the thermally generated emf was then nulled by passing current through the standard resistor. The current necessary for nulling was recorded.  $R_C$  and  $\Delta R$  were also recorded. The "hot" heater was then turned off and the "cold" heater turned on. The power input to this heater was adjusted so that  $R_C$  had approximately the same resistance as it did when only the "hot" heater was on; this power was then recorded.  $R_C$  and  $\Delta R$  were again recorded. Sometimes a relatively small thermal emf was generated by the "cold" heater, this is probably indicative of a small heat leak.

When this occurred, this voltage was nulled and the current necessary for the nulling was recorded. When analyzing the data, this latter voltage was subtracted from the thermal emf generated by the "hot" heater. This series of measurements was repeated for a few different power inputs to the "hot" heater and at several magnetic fields.

The electrical resistance of the sample could be measured by sending an electrical current through the sample and nulling the voltage which was generated (both heaters were off when making this measurement). The electrical current and the nulling current were both recorded. To correct for "thermals" the electrical current was then reversed, the voltage was again nulled and both currents were again recorded.

The bath was pumped down in 0.2K intervals and the carbon resistors calibrated. Complete sets of the types of measurements just described were normally made at bath temperatures of 4.2, 3.0, 2.1, and 1.4K.

From the above measurements the thermally generated voltage  $V$  the temperature difference across the sample  $\Delta T$  (including the corrections described in the thermometry section), and the average temperature of the sample could be determined. With this information we could compute

$$S(H,T) = \frac{V}{\Delta T} \left. \frac{\ell_R}{\ell_V} \right|_{H,T} \quad (\text{II.2})$$

where  $\ell_R$  is the distance between the 2 carbon resistors and  $\ell_V$  is the distance between the two voltage probes.

The correction factor  $\frac{\ell_R}{\ell_V}$  was needed because the temperature difference was measured over a larger distance (10% - 30%) than the voltage difference. This correction factor assumes that the temperature gradient is uniform between the carbon resistors. As a by-product of the S measurements, the thermal conductance K is also obtained:

$$K = \frac{Q}{\Delta T} \quad (\text{II.3})$$

where Q is the power input to the "hot" heater.

Having measured the resistance of the sample R, the thermal conductance K, and the average temperature T, at which the thermal conductance was measured, the Lorenz number L can be computed from the relation

$$L = \frac{KR}{T} \frac{\ell_R}{\ell_V} \quad (\text{II.4})$$

The correction factor  $\frac{\ell_R}{\ell_V}$  is included for the same reason as when computing S. At both  $H = 0$ , and in the high field limit L should be equal to the ideal Lorentz number,  $2.443 \times 10^{-8}$  watt- $\Omega/K^2$  in the limit where elastic impurity scattering is dominant.

## 2. Field Sweep Technique Measurements of S, K, and R

Measurements utilizing the field sweep method were performed using the following procedure. The analog

output of the monitor of the lock-in amplifier in the chopper-amplifier circuit was connected to the y-axis of an x-y recorder, and the analog output of the gaussmeter was connected to the x-axis. The field was then swept up at a rate of 7G/sec. After the field had increased approximately 1kG, the "hot" heater was turned on for the remainder of the sweep. Upon completion of the sweep, the "hot" heater was turned off and the field reduced to its initial value. The field was swept up again, this time with the heater off. If initially the output on the x-y recorder had shifted from the output of the previous sweep when the heater was off, the y-axis offset was adjusted to align the two recordings.

Following completion of the second sweep, two sets of calibration measurements were made with stationary magnetic fields. First, the output signal was measured at several magnetic fields for a constant input current to the reference resistor. A smooth curve was drawn through these data points to determine the amplification factor at all fields of interest (see Figures II.2 or II.3); this determined the correction of the raw data for the field dependent gain of the measuring system. Second,  $R_c$  and  $\Delta R$  were measured in the usual manner, with the "hot" heater adjusted to the same power as during the first sweep. Since the temperature difference increased only about 10% over the field range

between 10 and 20 kG, these resistances were measured only every 1 or 2kG. These two sets of calibration measurements were made after each thermopower recording.

Eq. (II.2) was again used to calculate  $S$ . At each magnetic field,  $V$  was determined by measuring the difference between the two lines on the x-y recording and then multiplying this difference by the appropriate amplification factor.  $\Delta T$  was found by first converting the  $R_c$  and  $R$  values to temperatures and temperature differences appropriate to the calibration fields and then linearly interpolating to obtain  $\Delta T$  at intermediate fields.

### III. NON-OSCILLATORY THERMOELECTRIC PHENOMENA - THEORY

#### A. Electron Diffusion

Electron diffusion  $S_d$  refers to the thermopower that would be measured if the phonon spectrum remained in local thermal equilibrium. In section III.A.1 a general expression for  $\Delta S_d$  of any system of non-interacting fermions (e.g. free electrons or quasi-particles) will be derived. In section III.A.2 both Averback and Wagner's<sup>(5)</sup> and Opsal and Wagner's<sup>(8)</sup> results for the evaluation of this general expression will be presented. Both of these calculations neglected the effect of the electron-phonon mass enhancement. Also in section III.A.2 we shall follow the work of Bass and Opsal<sup>(14)</sup> to show how this enhancement should be included in the evaluation of the general expression for  $\Delta S_d$ .

#### 1. General Relations

The following derivation of  $S_d$  is primarily based on the work of Averback and Wagner.<sup>(5)</sup> In this section it is advantageous to define the transport coefficients (tensors) according to the following scheme:

$$\vec{J} = \vec{\sigma} \cdot \vec{E} + \vec{\epsilon} \cdot (-\vec{\nabla}T) \quad (\text{III.1})$$

$$\vec{Q} = \vec{\pi} \cdot \vec{E} + \vec{\kappa} \cdot (-\vec{\nabla}T) \quad (\text{III.2})$$

where  $\vec{J}$  and  $\vec{Q}$  are the electrical and heat currents/unit area respectively.  $\vec{S}$  is defined as  $\vec{E}(\vec{\nabla}T)^{-1} \Big|_{\vec{J}=0}$ , so that  $\vec{S}$  and  $\vec{\epsilon}$  are related by the equation

$$\vec{S} = \vec{\sigma}^{-1} \cdot \vec{\epsilon} \quad . \quad (\text{III.3})$$

We assume a system of non-interacting fermions (electrons or quasi-particles) whose motion in the presence of electric and magnetic fields is governed by the rule:

$$\hbar \frac{d\vec{k}}{dt} = e\vec{E} + \frac{e}{c} \vec{v} \times \vec{H} \quad (\text{III.4})$$

where  $\vec{v}$  is given by

$$\hbar \vec{v} = \vec{\nabla}_{\vec{k}} \epsilon_{\vec{k}} \quad (\text{III.5})$$

with  $\hbar$  = Plank's constant divided by  $2\pi$

$e$  = electronic charge

$c$  = speed of light

$\epsilon_{\vec{k}}$  = energy of an electron in state  $\vec{k}$

$$\vec{\nabla}_{\vec{k}} = \left( \frac{\partial}{\partial k_x}, \quad \frac{\partial}{\partial k_y}, \quad \frac{\partial}{\partial k_z} \right) \quad .$$

It can then be readily shown within the framework of the linearized Boltzmann equation for  $\vec{E}$  and  $\vec{Q}$  along the  $x$  axis, and  $H$  along the  $z$  axis that:

$$\sigma_{xx} = \frac{e^2}{4\pi} \int d^3\vec{k} \, v_x f'_{\vec{k},E} \quad (\text{III.6a})$$



$$\epsilon_{xx} = \frac{ek_B}{4\pi} \int d^3\vec{k} \, v_x f'_{\vec{k},T} \quad (\text{III.6b})$$

$$\pi_{xx} = \frac{ek_B T}{4\pi} \int d^3\vec{k} \, (\epsilon_{\vec{k}} - \epsilon_F) \vec{v}_x f'_{\vec{k},E} \quad (\text{III.7a})$$

$$\kappa_{xx} = \frac{k_B^2 T}{4\pi} \int d^3\vec{k} \, (\epsilon_{\vec{k}} - \epsilon_F) \vec{v}_x f'_{\vec{k},T} \quad (\text{III.7b})$$

Here  $k_B$  is Boltzmann's constant,  $\epsilon_F$  is the Fermi energy, and  $[eE f'_{\vec{k},E}]$  ( $[-k_B \vec{\nabla} T f'_{\vec{k},T}]$ ) is the non-equilibrium portion of the distribution function for an electron in state  $\vec{k}$  when only an electric field (temperature gradient) is present. The above integrals are over  $\vec{k}$  space, but we can just as easily integrate over surfaces of constant energy and then integrate over all energies. Performing this change of variable gives:<sup>15</sup>

$$\int d^3\vec{k} = \int d\epsilon \int \frac{d^2S}{\hbar v} \quad (\text{III.8})$$

where  $S$  is a surface of constant energy. For convenience  $\int d^2S$  will be written as  $\int dS$ , with the understanding that  $\int dS$  is a 2-dimensional surface integral. It is now convenient to define the function  $\psi_{\vec{k}}$  by

$$f'_{\vec{k}} = \frac{(-\partial f_{\vec{k}}^0)}{\partial \epsilon} \psi_{\vec{k}} \quad (\text{III.9})$$

where  $f_{\vec{k}}^0 = [1 + \exp(\epsilon_{\vec{k}} - \epsilon_F)/k_B T]^{-1}$ .

In the ensuing analysis the subscript  $\vec{k}$  will be dropped, except where essential for clarity. Combining equations (III.6a, 8, 9) we see that

$$\sigma_{xx} = \int d\varepsilon \left( -\frac{\partial f^0}{\partial \varepsilon} \right) \sigma_{xx}(\varepsilon) \quad (\text{III.10})$$

where

$$\sigma_{xx}(\varepsilon) = \frac{e^2}{4\pi^3} \int \frac{dS}{\hbar v} v_x \psi_E \quad (\text{III.11})$$

Combining equations (III.7a) and (III.11) we see that

$$\begin{aligned} \pi_{xx} &= \frac{k_B T}{e} \int d\varepsilon \left( -\frac{\partial f^0}{\partial \varepsilon} \right) (\varepsilon - \varepsilon_F) \sigma_{xx}(\varepsilon) \\ &= e^2 L_O T^2 \left[ \frac{d}{d\varepsilon} \sigma_{xx}(\varepsilon) \right]_{\varepsilon=\varepsilon_F} + O\left(\frac{k_B T}{\varepsilon_F}\right)^3 \end{aligned} \quad (\text{III.12})$$

where  $L_O = \frac{\pi^2 k_B^2}{3e^2}$  (the ideal Lorenz number). From the Onsager relations<sup>(16)</sup> we know that  $\overleftrightarrow{\varepsilon}(\vec{H}) = \frac{\overleftrightarrow{\pi}^+(-\vec{H})}{T}$ , so we may write

$$\overleftrightarrow{\varepsilon}(\vec{H}) = e L_O T \left[ \frac{d}{d\varepsilon} \overleftrightarrow{\sigma}^+(-\vec{H}) \right]_{\varepsilon=\varepsilon_F} \quad (\text{III.13})$$

where  $\overleftrightarrow{\sigma}^+$  is the transpose of the tensor  $\overleftrightarrow{\sigma}$ . Using the Onsager relation  $\sigma_{ij}(\vec{H}) = \sigma_{ji}(-\vec{H})$  it follows from equation (III.3) that  $S_d$  is given by:

$$S_d(\vec{H}, T) = e L_O T \overleftrightarrow{\rho}(\vec{H}) \frac{d}{d\varepsilon} \overleftrightarrow{\sigma}(\vec{H}) \quad (\text{III.14})$$

where  $\overleftrightarrow{\rho}(\vec{H})$  is the resistivity tensor,  $\overleftrightarrow{\rho}(\vec{H}) = \overleftrightarrow{\sigma}^{-1}(\vec{H})$ . It is worth noting that eq. (III.14) holds for arbitrary scattering mechanisms.

In the experimental arrangement described in section II,  $S_{\text{exp}}$  is measured under adiabatic boundary conditions (i.e.,  $\vec{Q} = (Q, 0, 0)$ ), with  $\vec{H}$  along the z-axis.

$S_{\text{exp}}$  can then be related to the components of  $\vec{S}$  by the relation

$$S_{\text{exp}} = S_{xx} + S_{xy} \frac{\nabla_y T}{\nabla_x T}, \quad (\text{III.15})$$

provided that  $H$  is along a 2-fold or higher symmetry axis. Neglecting thermoelectric contributions we see from eq. (III.2) that the quantity  $\nabla_y T / \nabla_x T$  is related to the components of the thermal conductivity tensor,  $\vec{\kappa}$ , by the relation

$$\frac{\nabla_y T}{\nabla_x T} = - \frac{\kappa_{yx}}{\kappa_{yy}}. \quad (\text{III.16})$$

Combining equations (III.15) and (III.16) we obtain

$$S_{\text{exp}} = S_{xx} - S_{xy} \frac{\kappa_{yx}}{\kappa_{yy}}. \quad (\text{III.17})$$

Evaluating the first term on the right hand side of eq. (III.17) in the high field limit gives:

$$\begin{aligned} S_{xx}(H \rightarrow \infty) &= eL_o T [\rho_{xx}(H \rightarrow \infty) \frac{d}{d\epsilon} \sigma_{xx}(H \rightarrow \infty) \Big|_{\epsilon=\epsilon_F} \\ &\quad + \rho_{xy}(H \rightarrow \infty) \frac{d}{d\epsilon} \ln \sigma_{yx}(H \rightarrow \infty) \Big|_{\epsilon=\epsilon_F} \\ &= eL_o T [O(\frac{1}{H^2}) - \frac{1}{\sigma_{xy}(H \rightarrow \infty)} \frac{d}{d\epsilon} \sigma_{yx}(H \rightarrow \infty) \Big|_{\epsilon=\epsilon_F} \\ &= eL_o T \frac{d}{d\epsilon} \ln \sigma_{xy}(H \rightarrow \infty) \Big|_{\epsilon=\epsilon_F}. \end{aligned} \quad (\text{III.18})$$

For an uncompensated metal in the high field limit

$$\sigma_{xy}(\epsilon) = \frac{[n_e(\epsilon) - n_h(\epsilon)] ec}{H} + O\left(\frac{1}{H^3}\right) \quad (\text{III.19})$$

where  $n_e(\epsilon)$  and  $n_h(\epsilon)$  are the number of electrons and holes contained within the surface at  $\epsilon$ . Noting that the electronic specific heat is just

$$\gamma T = e^2 L_O T \frac{d}{d\epsilon} [n_e(\epsilon) - n_h(\epsilon)] \Big|_{\epsilon=\epsilon_F} \quad (\text{III.20})$$

we see that eq. (III.18) reduces to

$$S_{xx}(H \rightarrow \infty) = \frac{\gamma T}{(n_e - n_h)e} \quad (\text{III.21})$$

If we now assume that the scattering is predominantly elastic, then we can use the relation

$$\vec{\kappa} = L_O \vec{\sigma} \quad (\text{III.22})$$

to evaluate the second term on the right hand side of eq. (III.17) in the high field limit and obtain

$$\begin{aligned} -S_{xy}(H \rightarrow \infty) & \frac{\kappa_{yx}}{\kappa_{yy}} \\ &= e L_O T \left[ \rho_{xx}(H \rightarrow \infty) \frac{\sigma_{xy}(H \rightarrow \infty)}{\sigma_{yy}(H \rightarrow \infty)} \frac{d}{d\epsilon} \sigma_{xy}(H \rightarrow \infty) \Big|_{\epsilon=\epsilon_F} \right. \\ & \quad \left. + \rho_{xy}(H \rightarrow \infty) \frac{\sigma_{xy}(H \rightarrow \infty)}{\sigma_{yy}(H \rightarrow \infty)} \frac{d}{d\epsilon} \sigma_{yy}(H \rightarrow \infty) \Big|_{\epsilon=\epsilon_F} \right] \\ &= e L_O T \left[ \frac{d}{d\epsilon} \ln \sigma_{xy}(H \rightarrow \infty) - \frac{d}{d\epsilon} \ln \sigma_{yy}(H \rightarrow \infty) \right] \Big|_{\epsilon=\epsilon_F} \\ &= \frac{\gamma T}{(n_e - n_h)} - e L_O T \frac{d}{d\epsilon} \ln \sigma_{yy}(H \rightarrow \infty) \Big|_{\epsilon=\epsilon_F}. \end{aligned} \quad (\text{III.23})$$

Therefore we obtain

$$S_d(H \rightarrow \infty) = \frac{2\gamma T}{(n_e - n_h)e} - eL_o T \frac{d}{d\varepsilon} \ln \sigma_{yy}(H \rightarrow \infty) \Big|_{\varepsilon=\varepsilon_F}. \quad (\text{III.24})$$

For  $H = 0$ , the tensors  $\overleftrightarrow{\kappa}$  and  $\overleftrightarrow{\sigma}$  are both diagonal. Therefore from eq. (III.14) we find

$$S_d(H = 0) = eL_o T \frac{d}{d\varepsilon} \ln \sigma_{xx}(H = 0) \Big|_{\varepsilon=\varepsilon_F}. \quad (\text{III.25})$$

From equations (III.24) and (III.25) we find that the difference between  $S_{\text{exp}}(H \rightarrow \infty)$  and  $S_{\text{exp}}(H = 0)$ ,  $\Delta S_d$ , is

$$\begin{aligned} \Delta S_d = & \frac{2\gamma T}{(n_e - n_h)e} \\ & - eL_o T \left[ \frac{d}{d\varepsilon} \ln \sigma_{yy}(H \rightarrow \infty) \sigma_{xx}(H = 0) \right] \Big|_{\varepsilon=\varepsilon_F}. \quad (\text{III.26}) \end{aligned}$$

The first term on the right hand side of eq. (III.26) is independent of the details of the scattering and is completely determined by the host metal. If the scattering can be characterized by a relaxation time,  $\tau$ , whose energy dependence is the same at both high and low fields, then  $\tau$  cancels out of the second term, in which case this term can be evaluated simply from a knowledge of the Fermi surface of the host metal. This means that although both  $S_d(H \rightarrow \infty)$  and  $S_d(H = 0)$  may depend sensitively on the details of the scattering, their difference ( $\Delta S_d$ ) should be insensitive to the nature of the scattering. Such behavior has been observed in aluminum polycrystals.<sup>(4)</sup>

## 2. Effects of Electron-Phonon Mass Enhancement on $S_d$

Equation (III.26) was first evaluated for aluminum by Averback and Wagner.<sup>(5)</sup> In accordance with the accepted theory of the time (due to Prange and Kadanoff<sup>(6)</sup>) they used a value for  $\gamma$  which was appropriate to a free electron gas having the  $\epsilon_F$  of aluminum. This is not the electron-phonon enhanced  $\gamma$  which is directly obtained from specific heat measurements. Averback and Wagner also calculated the second term on the right hand side of eq. (III.26) within a 1-OPW approximation. The resulting value of  $\Delta S_d$  was about 30% lower than the value obtained from measurements on polycrystalline aluminum samples.<sup>(3,4)</sup> However, Averback and Wagner's calculation was more appropriate for comparison with measurements made on a single crystal with the magnetic field directed along a four-fold symmetric axis (as measured in this thesis), rather than with polycrystalline measurements. The results for H directed along a four-fold symmetric axis of a single crystal aluminum sample, which will be presented in section IV.a, are in good agreement with the polycrystalline results; thus the 30% discrepancy between Averback and Wagner's calculation and experiment remains.

The fact that Averback and Wagner's calculation did not correctly predict the single crystal results led Opsal and Wagner<sup>(8)</sup> to perform an improved calculation. Within the more exact 4-OPW approximation, but still

neglecting the effect of electron-phonon mass enhancement, they evaluated eq. (III.26) for  $H$  along the four-fold symmetric  $[100]$  axis. This improved calculation increased the discrepancy between theory and experiment. To determine how much  $\Delta S_d$  might change when the axis along which  $H$  is directed is changed, they also estimated  $\Delta S_d$  for  $H$  directed along the two-fold symmetric  $[110]$  axis. They found  $\Delta S_d$  for the two-fold symmetric axis to be about 7% smaller than for the four-fold symmetric axis.

Stimulated by the continuing disagreement between theory and experiment, Opsal<sup>(14,17)</sup> then reinvestigated the question of whether mass enhancement should appear in thermoelectricity. He showed that contrary to the statements made by Prange and Kadanoff,<sup>(6)</sup> the effects of the electron-phonon mass enhancement should appear in the thermoelectricity of metals. Subsequent to Opsal's initial work,<sup>(17)</sup> Lyo<sup>(18)</sup> confirmed, from a microscopic viewpoint, that the effects of mass enhancement should appear in thermoelectricity.

To see how  $S_d$  is affected by the electron-phonon mass enhancement (which is a consequence of the electron-phonon interaction), the work of Bass and Opsal<sup>(14)</sup> will be followed. It will be shown that whereas the electrical conductivity is unenhanced, the thermoelectric power is enhanced. This will be shown for the case of elastic impurity scattering, by consistently renormalizing all

properties of the electrons to include the electron-phonon mass enhancement.

Crudely speaking, the electron-phonon interaction may be pictured as follows: An electron, by virtue of the Coulomb interaction, attracts nearby positive ions; as the electron moves through the crystal lattice it tries to drag these positive ions along with it. This is equivalent to an increase in the electron's effective mass. By dragging these positive ions along, the electron distorts the crystal lattice in its immediate neighborhood; by virtue of the long range nature of the Coulomb interaction, this distortion is "felt" by other electrons, and thus electrons which otherwise would not have been coupled are coupled together by the electron-phonon interaction. For weakly coupled electrons we get a system of non-interacting quasi-particles, described by the same wavevectors,  $\vec{k}$ , but with energy, <sup>(19)</sup>  $\epsilon_{\vec{k}}$ , given by

$$\epsilon_{\vec{k}} = \epsilon_{\vec{k}}^u + \Sigma(\epsilon_{\vec{k}}, \vec{k}) . \quad (\text{III.27})$$

$\epsilon_{\vec{k}}^u$  is simply the unperturbed band energy of the electron and  $\Sigma(\epsilon_{\vec{k}}, \vec{k})$  is the electron self energy due to electron-phonon interactions.

Now we will consider an ideal system of these quasi-particles which at low temperatures are elastically scattered by a random distribution of fixed impurities. The transport properties of these quasi-particles may be



described in terms of a mean free path  $\vec{\ell}_{\vec{k}}$  which is related to the renormalized relaxation time  $\tau_{\vec{k}}$ , by  $\vec{\ell}_{\vec{k}} = \vec{v}_{\vec{k}} \tau_{\vec{k}}$ .  $\vec{v}_{\vec{k}}$  is the velocity of a quasi-particle in state  $\vec{k}$ , and is defined by  $\vec{v}_{\vec{k}} = \frac{1}{\hbar} \vec{\nabla}_{\vec{k}} \epsilon_{\vec{k}}$ . We wish to relate the velocity of a quasi-particle to that of a free electron,  $\vec{v}_{\vec{k}}^u = \frac{1}{\hbar} \vec{\nabla}_{\vec{k}} \epsilon_{\vec{k}}^u$ . From eq. (III.27) we see that

$$\frac{1}{\hbar} \vec{\nabla}_{\vec{k}} \epsilon_{\vec{k}} = \frac{1}{\hbar} \vec{\nabla}_{\vec{k}} \epsilon_{\vec{k}}^u + \frac{1}{\hbar} \frac{\partial \Sigma}{\partial \epsilon_{\vec{k}}} \vec{\nabla}_{\vec{k}} \epsilon_{\vec{k}} + \frac{1}{\hbar} \frac{\partial \Sigma}{\partial \vec{k}}$$

or

$$\frac{1}{\hbar} \vec{\nabla}_{\vec{k}} \epsilon_{\vec{k}} = \frac{\frac{1}{\hbar} \vec{\nabla}_{\vec{k}} \epsilon_{\vec{k}}^u}{(1 - \frac{\partial \Sigma}{\partial \epsilon_{\vec{k}}})} + \frac{\frac{1}{\hbar} \frac{\partial \Sigma}{\partial \vec{k}}}{(1 - \frac{\partial \Sigma}{\partial \epsilon_{\vec{k}}})} . \quad (\text{III.28})$$

The mass enhancement parameter  $\lambda_{\vec{k}}$  is defined as  $-\frac{\partial \Sigma(\epsilon_{\vec{k}}, \vec{k})}{\partial \epsilon_{\vec{k}}}$ .

So by making use of the appropriate definitions, eq.

(III.28) may be rewritten as

$$\vec{v}_{\vec{k}} = \frac{\vec{v}_{\vec{k}}^u}{(1 + \lambda_{\vec{k}})} + \frac{\vec{\eta}_{\vec{k}}}{(1 + \lambda_{\vec{k}})} \quad (\text{III.29})$$

with the definition

$$\vec{\eta}_{\vec{k}} \equiv \frac{1}{\hbar} \frac{\partial \Sigma(\epsilon_{\vec{k}}, \vec{k})}{\partial \vec{k}} .$$

$\vec{\eta}_{\vec{k}}$  is much smaller than  $\vec{v}_{\vec{k}}^u$  (by approximately the ratio of the sound velocity to the Fermi velocity<sup>(18)</sup>), and in most cases can be neglected. We also note that at  $\epsilon_F$ ,  $\lambda_{\vec{k}}$  is always positive, so the quasi-particles will have lower velocities than the free electrons, which is what

we expected from our elementary picture of the electron-phonon interaction. Additionally, a perturbation treatment of the impurity scattering between quasi-particle states shows that  $\tau_{\vec{k}} = \tau_{\vec{k}}^u (1 + \lambda_{\vec{k}})$ .<sup>(19)</sup> Thus  $\ell_{\vec{k}} = \ell_{\vec{k}}^u + \eta_{\vec{k}} \tau_{\vec{k}}^u$ . Since  $\eta_{\vec{k}} \ll \frac{\tau_{\vec{k}}^u}{v_{\vec{k}}^u}$ , we find that  $\ell_{\vec{k}} \approx \ell_{\vec{k}}^u$ ; i.e. the mean free path is essentially unchanged by the inclusion of the electron-phonon interaction. In the interest of notational simplicity from here on the subscript  $\vec{k}$  and vector symbols will be dropped from  $\ell$ ,  $\tau$ ,  $\vec{v}$ ,  $\lambda$ , and  $\eta$ , except where essential for clarity.

Upon application of a small  $\vec{E}$  field, the system of quasi-particles may be described by the linearized Boltzmann equation<sup>(20)</sup>

$$\frac{\partial \psi}{\partial t} + e\vec{E} \cdot \vec{v} = \frac{\psi}{\tau} \quad (\text{III.30})$$

with  $\psi$  given by eq. (III.9). Rewriting eq. (III.30) in terms of unrenormalized (free-electron) variables and neglecting  $\eta$  compared to  $v^u$  gives

$$(1 + \lambda) \frac{\partial \psi}{\partial t} + e\vec{E} \cdot \vec{v}^u = \frac{\psi}{\tau^u} \quad (\text{III.30})$$

For the steady state case,  $\frac{\partial \psi}{\partial t} = 0$ , so  $\psi$  is essentially the same for both the renormalized (quasi-particle) and unrenormalized (free electron) cases; namely  $\psi = e\vec{E} \cdot \vec{v}_{\tau} \approx e\vec{E} \cdot \vec{v}_{\tau^u}^u$ . When eq. (III.10) is written in dyadic notation we see

$$\vec{\sigma}(\epsilon) = \frac{e^2}{4\pi^3\hbar} \int_{S(\epsilon)} dS \frac{\vec{v}}{v} \tau \vec{v} \quad (\text{III.31a})$$

$$\cong \frac{e^2}{4\pi^3\hbar} \int_{S(\epsilon)} dS \frac{\vec{v}^u}{v} \tau \vec{v}^u \quad (\text{III.31b})$$

where the integral is over the renormalized constant energy surface. As can be seen in Figure III.1, the  $\epsilon$  vs  $k$  relations are different for renormalized and unrenormalized cases, except at the Fermi energy. For the temperature range examined in this thesis, the electrical conductivity is simply  $\sigma(\epsilon = \epsilon_F)$ , and therefore the electrical conductivity of a metal is not affected by renormalization.

We recall from eq. (III.14) that

$$\begin{aligned} S_d &= eL_O T \left[ \frac{d}{d\epsilon} \ln \sigma(\epsilon) \right] \Big|_{\epsilon=\epsilon_F} \\ &= \frac{eL_O T}{\sigma(\epsilon = \epsilon_F)} \frac{d\sigma(\epsilon)}{d\epsilon} \Big|_{\epsilon=\epsilon_F} . \end{aligned} \quad (\text{III.14})$$

In appendix II it is shown that

$$\frac{d\sigma(\epsilon)}{d\epsilon} \Big|_{\epsilon=\epsilon_F} = \frac{e^2}{12\pi^3\hbar} \int_{S(\epsilon_F)} \frac{dS}{\hbar v} \vec{v}_k \cdot (\tau \vec{v}) . \quad (\text{AII.5})$$

Substituting in unrenormalized variables yields

$$\begin{aligned} \frac{d\sigma(\epsilon)}{d\epsilon} \Big|_{\epsilon=\epsilon_F} &= (1 + \lambda) \frac{e^2}{12\pi^3\hbar} \int_{S(\epsilon_F)} \frac{dS}{\hbar v^u} \vec{v}_k \cdot \\ &(\tau \vec{v}^u + \tau \vec{\eta}) . \end{aligned} \quad (\text{III.32})$$

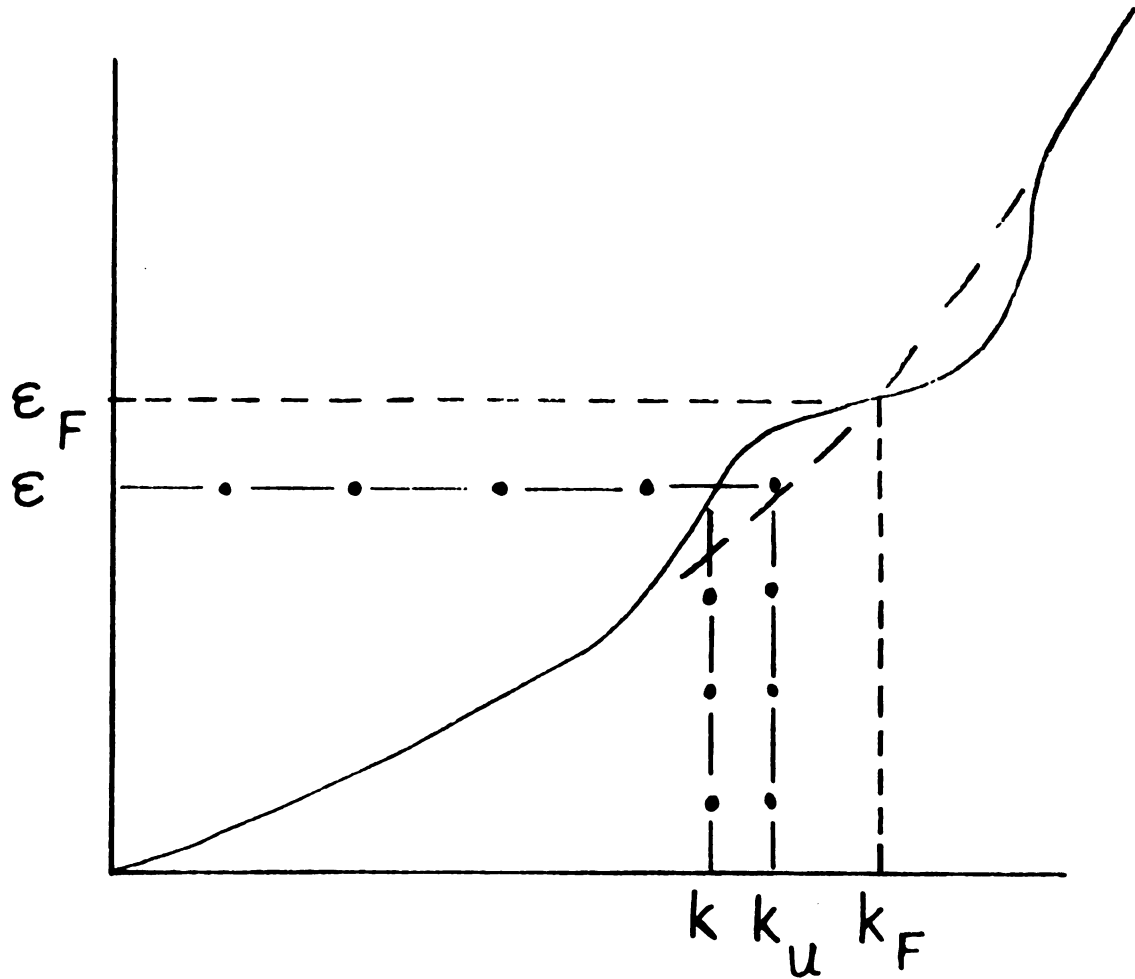


Figure III.1:  $\epsilon$  vs.  $k$  relations for free electrons (dashed curve) and for quasi-particles (solid curve).

Identifying  $\left. \frac{d\sigma^u(\epsilon^u)}{d\epsilon^u} \right|_{\epsilon^u=\epsilon_F} = \frac{e^2}{12\pi^3\hbar} \int_{S(\epsilon_F)} \frac{dS}{\hbar v^u} \vec{\nabla}_k \cdot (\vec{\tau}^u \vec{v}^u),$

$$\left. \frac{d\sigma(\epsilon)}{d\epsilon} \right|_{\epsilon=\epsilon_F} = (1 + \lambda) \left. \frac{d\sigma^u(\epsilon^u)}{d\epsilon^u} \right|_{\epsilon^u=\epsilon_F} + (1 + \lambda) \frac{e^2}{12\pi^3\hbar} \int_{S(\epsilon_F)} \frac{dS}{\hbar v} \vec{\nabla}_k \cdot (\vec{\eta} \vec{\tau}^u). \quad (\text{III.33})$$

Combining equations (III.14) and III.33) and noting that

$$S_d^u = eL_O T \left[ \left. \frac{d\sigma^u(\epsilon^u)}{d\epsilon^u} \right] \right|_{\epsilon^u=\epsilon_F} \quad \text{we obtain}$$

$$S_d = (1 + \lambda) S_d^u + s \quad (\text{III.34})$$

where

$$s = (1 + \lambda) \frac{e^2}{12\pi^3\hbar} \int \frac{dS}{\hbar v^u} \vec{\nabla}_k \cdot (\vec{\eta}_k \vec{\tau}^u).$$

Up to this point we have not considered the effect of a magnetic field on the quasi-particles. Using the semi-classical equation of motion for Bloch electrons in a magnetic field, eq. (III.4), it can be shown that the Boltzmann equation for steady state transport is not affected by renormalization,<sup>(6)</sup> so we may write in general

$$S_d(H) = (1 + \lambda) S_d^u(H) + s(H). \quad (\text{III.35})$$

Lyo<sup>(18)</sup> points out that although  $\eta/v^u$  is very small, the quantity  $[\vec{\nabla} \cdot (\vec{\eta} \vec{\tau}^u) / \vec{\nabla} \cdot (\vec{v}^u \vec{\tau}^u)]$  is not necessarily small; therefore one cannot justify neglecting

$s(H)$  compared with  $S_d(H)$ . However, it is expected that  $s(H)$  is rather insensitive to  $H$ .<sup>(18)</sup> Therefore, we see for the quantity of experimental interest,  $\Delta S_d$  ( $= S_d(H \rightarrow \infty) - S_d(H = 0)$ ) that

$$S_d \approx (1 + \lambda) \Delta S_d^u \quad (\text{III.36})$$

Equation (III.36) indicates that  $S_d$  will be enhanced by the factor  $(1 + \lambda)$ .

### B. Phonon Drag

In the preceding sections we tacitly assumed that only the electrons experienced a non-equilibrium condition, while the phonons remained in local thermal equilibrium. However, in actuality, this situation is not realized. Since there is a temperature difference across the sample, there will be a higher density of phonons at the hot end than at the cold end of the sample; therefore, a phonon flux will be created. These phonons can scatter off electrons and thereby impart a net momentum to the electron distribution. If no electrical current is permitted to flow, then an electric field acting on the electrons will be required to balance the force due to the phonon flux. Thus, a thermal emf will develop across the sample. This contribution to the thermopower is known as phonon drag,  $S_g$ .

Considering only phonon-electron scattering processes for an isotropic phonon gas, MacDonald<sup>(21)</sup> used a

simple kinetic theory approach to derive the relationship

$$S_g = \frac{1}{3N_e} C_g . \quad (\text{III.37})$$

In eq. (III.37)  $C_g$  is the lattice specific heat per unit volume, and  $N$  is the number of electrons per unit volume. At low temperatures a Debye spectrum of phonons has a  $C_g$  which exhibits a  $T^3$  behavior, so that we expect from eq. (III.37)

$$S_g \propto T^3 \quad T \ll \theta_D , \quad (\text{III.38})$$

where  $\theta_D$  is the Debye temperature of the metal. Equation (III.38) was also obtained by Hanna and Sondheimer,<sup>(22)</sup> using a more sophisticated approach involving the solution of the coupled Boltzmann equations for electrons and phonons. In deriving eq. (III.37), (and consequently eq. (III.38)) all phonon scattering processes other than phonon-electron scattering were neglected. To the extent that these other scattering events do not produce a thermal emf, eq. (III.38) overestimates  $S_g$ . To a first approximation  $S_g$  would then be reduced by a factor  $\tau_{px}/(\tau_{pe} + \tau_{px})$  yielding

$$S_g = S_0 \frac{\tau_{px}}{\tau_{pe} + \tau_{px}} . \quad (\text{III.39})$$

In eq. (III.39),  $S_0 = 1/3 (C_g/Ne)$ ,  $\tau_{pe}$  is the relaxation time for the scattering of phonons by electrons, and  $\tau_{px}$  is the relaxation time for the scattering of phonons by

everything else. At high temperatures,  $T \gg \theta_D$ ,  $\tau_{px}$  is expected to be much shorter than  $\tau_{pe}$ , both  $C_g$  (and consequently  $S_0$ ) and  $\tau_{pe}$  are independent of temperature, and  $\tau_{px}$  is inversely proportional to  $T$  (for  $T \gg \theta_D$ , the number of phonons is proportional to  $T$ ). We thus see that the phonon drag thermopower, as given by eq. (III.39), should vary inversely with temperature. At low temperatures,  $T \ll \theta_D$ ,  $\tau_{px}$  is much longer than  $\tau_{pe}$  and therefore eq. (III.39) reduces to eq. (III.38).

We will now briefly examine the effects upon  $S_g$  of some departures from the ideal free electron gas behavior which may be expected in a real metal. A real metal has Bragg reflection planes. Consequently, Umklapp scattering processes are allowed, and these can have a profound effect on  $S_g$ . To illustrate this point we consider both Normal and Umklapp scattering processes for a spherical Fermi surface.

Umklapp scattering is distinguished from Normal scattering by the appearance of a reciprocal lattice vector  $\vec{G}$  in the momentum conservation relation, i.e.,

$$\vec{k} - \vec{k}' = \vec{q} + \vec{G} \quad (\text{III.40})$$

where  $\vec{q}$  is the phonon wavevector. For a Normal scattering event  $\vec{G} = 0$ . Figure III.2(a) shows a phonon-electron Normal scattering event. From this figure we see that the change in the electron's momentum  $\Delta\vec{k}$  is in the same



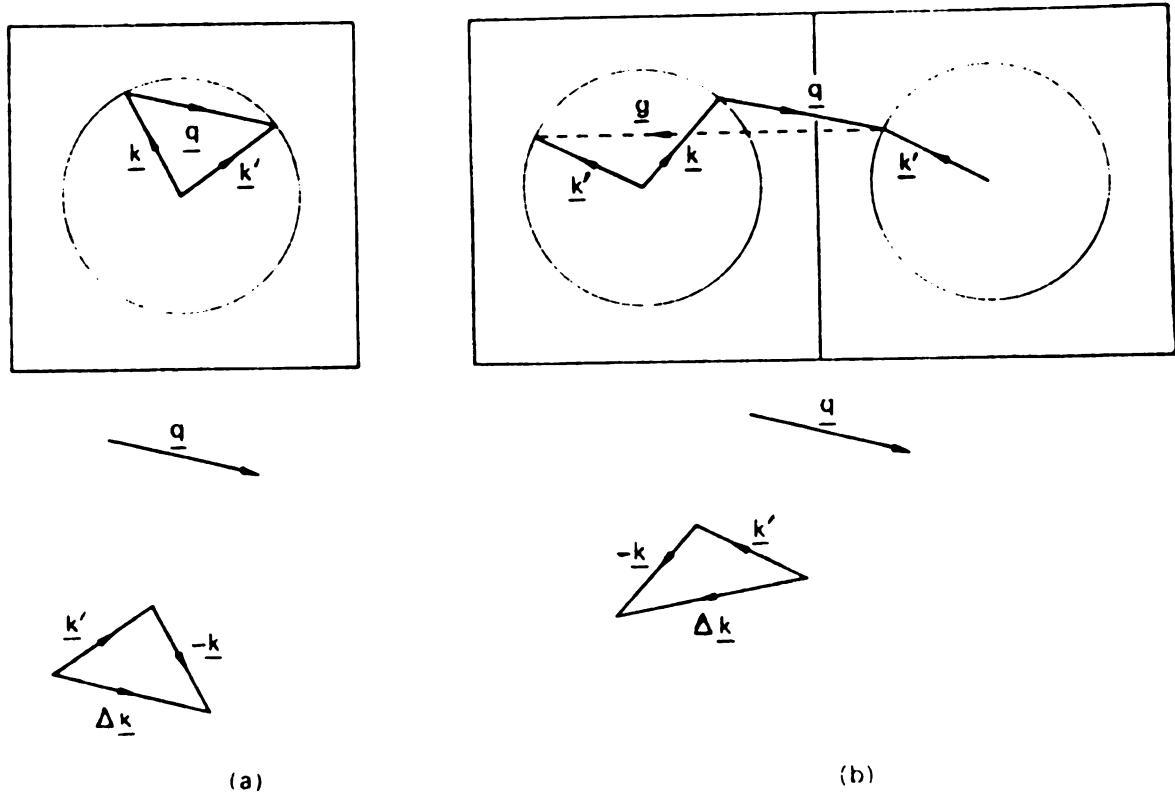


**Figure III.2:** The change of electron wavevector accompanying the annihilation of a phonon by a (a) Normal process, (b) Umklapp process (after Barnard<sup>(23)</sup>).

direction as  $\vec{q}$ . Since the electron's velocity is directed normal to the Fermi surface, i.e., in the direction of  $\vec{k}$  for the cases considered in Figure III.2  $\Delta\vec{v}$  is in the same direction as  $\vec{q}$ , so the electrons will move in the same direction as the phonon flux, (i.e. down the temperature gradient), thus contributing a negative  $S_g$ . Figure III.2(b) shows a phonon-electron Umklapp scattering event. From this figure we see that after transforming the momentum of the electron after the interaction  $\vec{k}'$  by a reciprocal lattice vector,  $\Delta\vec{k}$  is now approximately anti-parallel to  $\vec{q}$ ; thus the electron will move up the temperature gradient producing a positive  $S_g$ . So for a spherical Fermi surface, Normal scattering events produce a negative  $S_g$ , while Umklapp scattering events usually produce a positive  $S_g$ .

However, most metals, including aluminum and indium, have complex Fermi surfaces. Bailyn<sup>(24)</sup> and Ziman<sup>(25)</sup> both employed variational techniques to calculate  $S_g$  for a complex Fermi surface taking both Normal and Umklapp scattering into account. They each obtained quite general expressions for  $S_g$ . A discussion of their expressions would take us far afield from the major topics of this thesis, so only the results concerning the sign of  $S_g$  will be considered. Ziman's result leads to the approximate rule that "the contribution to  $S_g$  will be negative or positive according to whether the chord  $q$

between the points  $k$  and  $k'$  passes through occupied or unoccupied regions of the Fermi surface."<sup>(25)</sup> Bailyn's analysis leads to a similar rule.

To illustrate the significance of Ziman's rule for a complex Fermi surface, we consider aluminum, a nearly free electron-like metal. The Fermi surface areas of aluminum lie only within the second and third Brillouin zones. Figure III.3 shows a schematic representation of two dimensional slices through the second and third zones showing the occupied regions. A number of phonon-electron scattering events (both Normal and Umklapp) are indicated, and their contributions to  $S_g$  can be discussed within the framework of Ziman's criterion. In Figure III.3 all A type scattering events should contribute negatively while the B type should give positive contributions.

All the results stated so far concerning  $S_g$  have been confined to the  $H = 0$  situation. Almost all the work in the presence of a magnetic field has concentrated on the single component  $(\epsilon_{xy})_g$ . Blewer, et. al.<sup>(27)</sup> have shown for an isotropic phonon gas that

$$(\epsilon_{xy})_g = \frac{c}{H} \frac{1}{3} C_g , \quad (\text{III.40})$$

an expression which is quite similar to eq. (III.37). Contrary to the electron diffusion terms, Opsal<sup>(28)</sup> has shown that none of the phonon drag terms of the thermoelectric tensor are enhanced by the electron-phonon

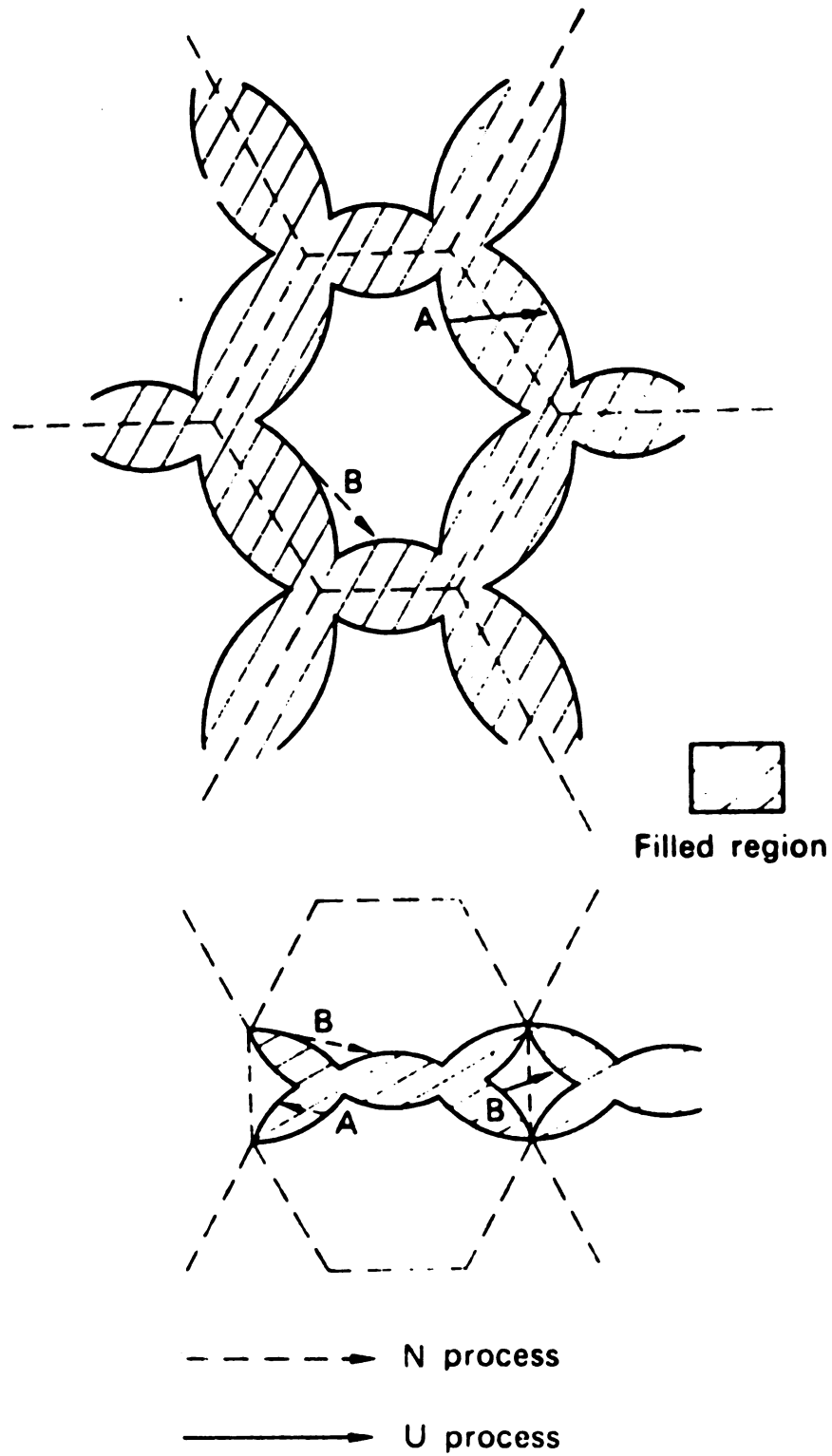


Figure III.3: Schematic diagrams of sections through the 2<sup>nd</sup> (upper) and 3<sup>rd</sup> (lower) zones of Al showing electron-phonon scattering events (after Gripshover, et. al. (26)).

interaction. Currently, calculations of the phonon drag terms of the thermoelectric tensor in the presence of a magnetic field have not been performed for a single metal.

#### IV. NON-OSCILLATORY THERMOELECTRIC PHENOMENA - EXPERIMENT

##### A. Aluminum

##### 1. Introduction

Measurements of the magnetothermopower of polycrystalline samples of "pure" aluminum and very dilute aluminum based alloys (25 ppm to 350 ppm impurity concentration) are reported by Averback<sup>(3)</sup> and Averback, et. al.<sup>(4)</sup> Their results span a temperature range between 2 and 6K, and a magnetic field range up to 20kG. The results may be summarized as follows:

(1) For all samples the data were consistent with the equation  $S(H,T) = A(H)T + B(H)T^3$ , allowing a separation of the electron diffusion thermopower component  $S_d(H,T) = A(H)T$  from the phonon drag component  $S_g(H,T) = B(H)T^3$ . This separation assumes that in the presence of a magnetic field  $S_g$  retains its zero field form i.e.  $S_g \propto T^3$ .

(2) Upon application of a transverse magnetic field  $A(H)$  (i.e.  $S_d$ ) first became more positive and then appeared to saturate in high fields.

(3) Although  $A(H = 0)$  and  $A(H \rightarrow \infty)$  varied from impurity to impurity, the quantity

$\Delta A = A(H \rightarrow \infty) - A(H = 0)$  was nearly impurity independent;  $\Delta A$  varied only from  $2.1 - 2.6 \times 10^{-8} \text{V/K}^2$ .

This insensitivity to the nature of the impurity suggests that  $\Delta S_d$  is determined primarily by the properties of the host metal aluminum.

Using no adjustable parameters, Averbach and Wagner<sup>(5)</sup> calculated  $\Delta A$  for aluminum. They obtained  $\Delta A = 1.6 \times 10^{-8} \text{V/K}^2$ , which is approximately 30% smaller than the experimental value. However, Averbach and Wagner's calculation assumed that the magnetothermopower was not influenced by the electron-phonon mass enhancement, that a 1-OPW Fermi surface would adequately describe the electronic properties of aluminum, and that the applied magnetic field was directed along an axis of four-fold symmetry in a single crystal containing an impurity which scatters electrons isotropically. The experimental results, on the other hand, had been obtained with polycrystalline samples containing impurities for which no independent information concerning scattering anisotropy is yet available. It thus seemed possible that the 30% discrepancy might arise from any of three sources:

- (1) Incompatibility between theory and experiment, in that the measurements were not performed on appropriate samples under proper conditions for comparison with the calculation.

(2) Inadequacy of a 1-OPW Fermi surface for calculation of the thermopower in aluminum.

(3) Neglect of the electron-phonon mass enhancement.

In an effort to experimentally test the viability of source (1), measurements were performed on an oriented single crystal foil of aluminum containing 50 ppm gallium. Recent calculations by Sorbello<sup>(7)</sup> indicate that gallium in aluminum should scatter electrons nearly isotropically.\* The single crystal was oriented so that the magnetic field could be directed along both the four-fold symmetric [010] axis and the two-fold [110] axis. The data obtained from this crystal will be compared with the polycrystalline data of Averbach, et. al.,<sup>(4)</sup> and also with the theory presented in the previous section.

As already indicated in section III.A.2, Opsal and Wagner<sup>(8)</sup> recently ruled out source (2), by showing that a 4-OPW Fermi surface still leaves a significant discrepancy between theory and experiment. It will be shown that source (3) is the major cause of the discrepancy between theory and experiment. The single

---

\* Sorbello showed explicitly that the scattering of the third zone electrons by gallium was isotropic to within a few percent, and indicated that the scattering of second zone electrons was also nearly isotropic. Using his phase shifts and amplitude factors, it was found that the scattering of second and third zone electrons is the same to within a few percent (see Appendix I).



crystal data can be explained by the theory of section III.A.2 provided an electron-phonon mass enhancement of 45% is used.

## 2. Sample

The aluminum foil was 0.6mm thick, 1.6mm wide, and the superconducting NbTi potential leads were 30mm apart. The crystal was oriented so that the [001] axis lay within  $1^\circ$  of the longitudinal axis of the foil and the [010] axis was rotated  $20^\circ$  from the normal to the foil. Once the sample was mounted in the sample holder, the heat current flowed along the longitudinal axis, and the magnetic field  $H$  was directed transverse to the heat current. The axis of rotation of the magnet coincided with the longitudinal axis of the sample. Therefore the magnetic field could be aligned along either the four-fold symmetric {010} family of axes or the two-fold symmetric {110} family. Thus, it was possible to determine whether  $\Delta S_d$  was sensitive to the direction of  $H$  relative to the crystallographic axes of aluminum.

## 3. Data and Analysis

### 3.1 Determination of the non-oscillatory results

In the absence of any applied magnetic field, the thermally generated voltages were measured using the nulling technique described in sec. II.A.2. However, for  $H > 10$  kG, the presence of giant quantum oscillations when  $H$  was directed along a four-fold symmetric axis<sup>(29-31)</sup>

(see section VI.A.3) made the field sweep measurement technique (see sec. I.A.3) advantageous. Figure IV.1 shows the maxima, minima, and the derived values of the non-oscillatory component of  $S$  for a typical field sweep after making the corrections outlined in sec. II.G. The non-oscillatory component of the thermopower was obtained by averaging each minimum with the average of its two adjacent maxima, and each maximum with the average of its two adjacent minima. From figures similar to Figure IV.1 the non-oscillatory of  $S$  could be extracted as a function of  $H$  at a constant temperature. As indicated in Figure IV.1, the non-oscillatory component saturated in value, to within experimental uncertainty, by  $15\text{kG}^*$ . In the ensuing analysis the  $15\text{kG}$  value will always be used as the high field limiting value of  $S$  (above  $15\text{kG}$  the measuring uncertainties increased rapidly with increasing field).

Since the thermopower oscillations are so large, small uncertainties in their magnitudes are magnified into large uncertainties in the magnitude of the non-oscillatory component. With care and patience the non-oscillatory component was extracted with an uncertainty of about 10% (at a 70% confidence level). The bulk of this uncertainty arises from slow variations of the zero baseline and from

---

\* In some cases  $S$  had not quite saturated by  $15\text{kG}$ , but the resulting small increases do not significantly change any of the conclusions reached in this thesis.

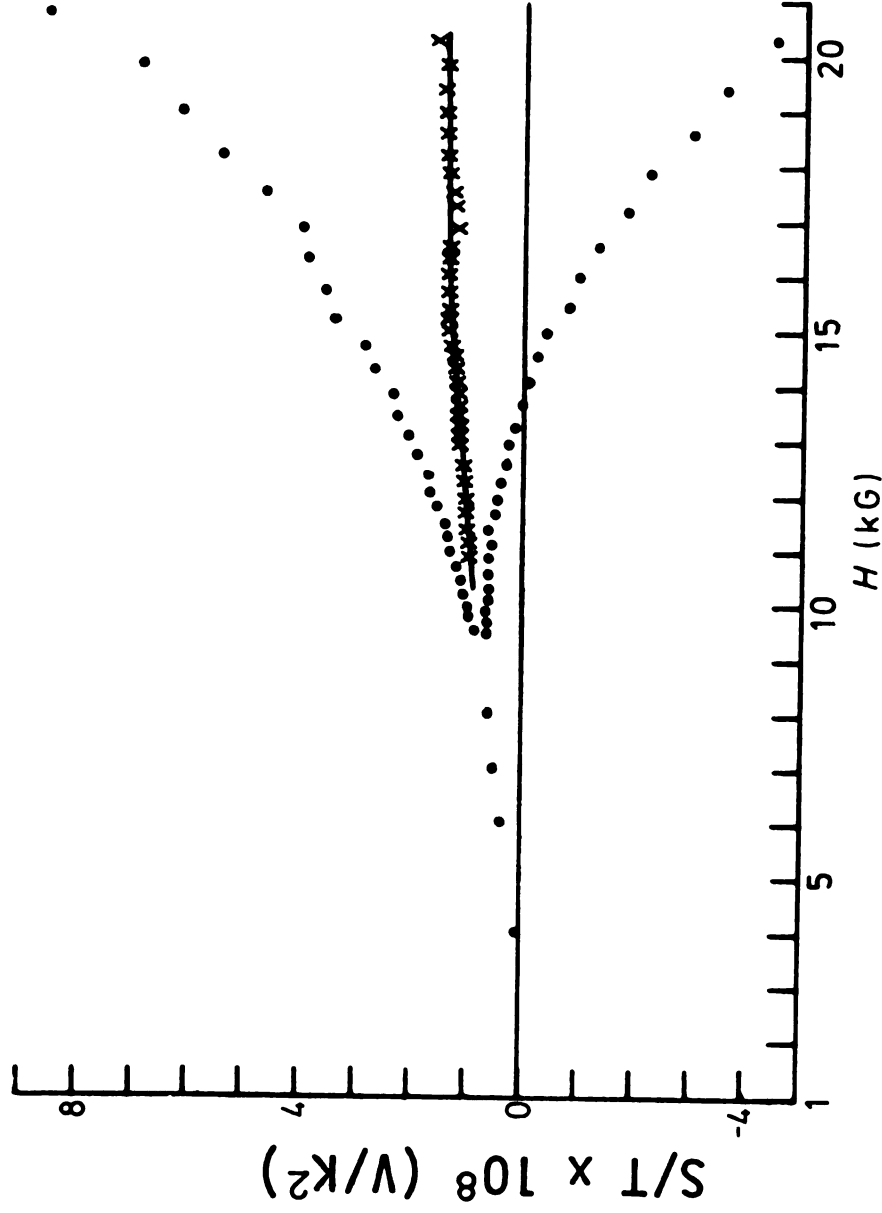


Figure IV.1: The variation of  $S$  with magnetic field at 3.55K for the Al(Ga) sample. The magnetic field is directed along the [010] axis. The maxima and minima of the quantum oscillations are represented by circles, and the non-oscillatory component of  $S$  is represented by the crosses.

electrical noise created by vibration of the sample holder in the magnetic field.

On the basis of the polycrystalline aluminum measurements by Averbach, et. al.<sup>(4)</sup> it is expected that the single crystal data should be of the form

$$S(H,T) = A(H)T + B(H)T^3 \quad (\text{IV.1})$$

Therefore if we plot  $S/T$  vs  $T^2$ , we should obtain a straight line with slope  $B(H)$  and intercept (with the  $T^2 = 0$  axis)  $A(H)$ . We are interested in the quantity

$$\frac{\Delta S_d}{T} = \Delta A = A(H \rightarrow \infty) - A(H = 0) \quad (\text{IV.2})$$

### 3.2 $\Delta A$ for H parallel to [100] and [010] axes

In Figure IV.2, the ratio of the non-oscillatory component of  $S$  to the absolute temperature  $T$  is plotted as a function of  $T^2$  for  $H = 0$  and  $H = 15\text{kG}$ . The error bars reflect the 10% uncertainty which was previously assigned to each point. In each case the data are consistent with straight lines. If there is any misalignment of the potential leads on the sample, the value of  $S$  should change when the magnetic field is reversed. To test for such an effect, measurements were made with the magnetic field both forward (open symbols) and reversed (filled symbols). To within experimental uncertainty, no systematic differences were observed. Straight lines were therefore drawn through

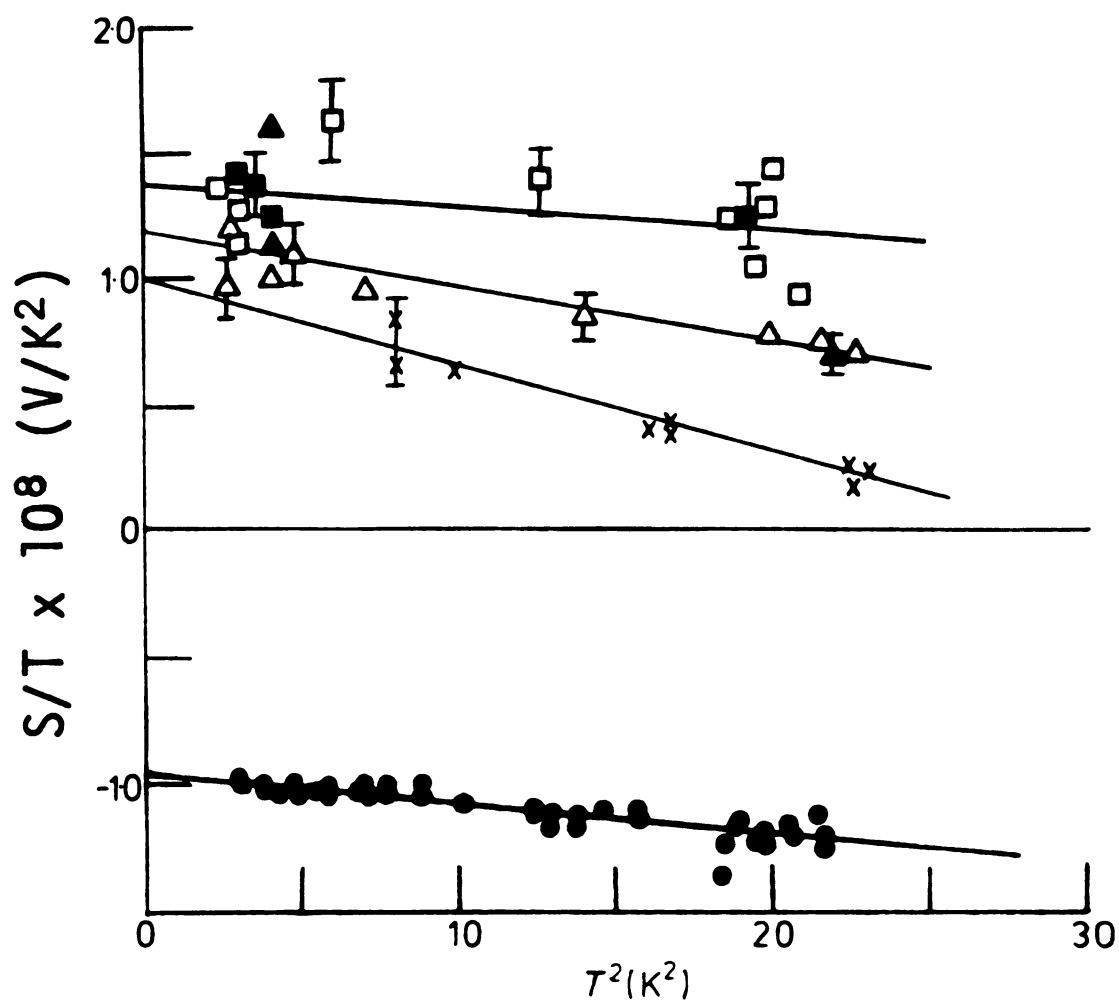


**Figure IV.2:** The temperature dependence of the non-oscillatory component of  $S$  of the Al(Ga) sample for:  $H = 15\text{kG}$  and parallel to  $[010]$  (squares);  $H = 15\text{kG}$  and parallel to  $[100]$  (triangles);  $H = 15\text{kG}$  and parallel to  $[110]$  (crosses);  $H = 0\text{kG}$  (circles). The full symbols indicate data obtained with  $H$  reversed.

all data for a given field direction. The quantity  $\Delta A$  can be obtained directly from Figure IV.2; it is simply the difference between the intercepts for  $H \rightarrow \infty$  (here taken to be 15kG) and  $H = 0$ .

To test whether the results were dependent upon the orientation of  $H$  relative to the foil axes,  $\Delta S_d$  was measured with the magnetic field along the two crystallographically equivalent [010] and [100] axes. Figure IV.2 shows that the data for these two directions are systematically different, but the differences are comparable to the uncertainties in the data. The average of the [010] and [100] values gives a "best value" of  $\Delta A = (2.23 \pm 0.25) \times 10^{-8} \text{V/K}^2$ . This average value agrees to within experimental uncertainty with the  $\Delta A$  values obtained for each direction individually.

The average value of  $\Delta A$  is in good agreement with the polycrystalline data of Averback, et. al.<sup>(4)</sup> It is also in agreement with the calculation of Opsal and Wagner,<sup>(8)</sup> provided that a 45% electron-phonon mass enhancement is included. A 45% electron-phonon mass enhancement is consistent with values inferred from both de Haas-van Alphen<sup>(32)</sup> and low temperature specific heat data<sup>(33)</sup> on aluminum.

### 3.3 $\Delta A$ for $H$ parallel to {110} axes

We have noted in section III.A.2 that Opsal and Wagner<sup>(8)</sup> predicted that  $\Delta S_d$  should be somewhat smaller for  $H$  directed along a two-fold axis than a four-fold axis

in aluminum. In this section results will be presented for H directed along each of the four, two-fold symmetric axes (the {110} family) lying in the (001) plane.

The data for H along any of the {110} axes are shown in Figure IV.2. Since the data for all four equivalent axes were the same to within the specified uncertainties, we will not distinguish between these axes in Figure IV.2. Also, for these axes the magnetothermopower oscillations were an order of magnitude smaller than for the {010} axes. This accounts for the smaller error bars in Figure IV.2. From this figure we see that  $\Delta A = (2.0 \pm 0.2) \times 10^{-8} \text{ V/K}^2$  for H along these axes. This value is about 10% smaller than that for H along the {010} axes, in agreement with the calculation by Opsal and Wagner.<sup>(8)</sup>

### 3.4 Effects of Magnetic Breakdown

The previously mentioned giant quantum oscillations in S for H along the {010} axes (Figure IV.1) are believed to arise from magnetic breakdown.<sup>(29,30)</sup> However, Opsal and Wagner's calculation of the non-oscillatory component of S completely neglects breakdown. The following argument is made against the presence of significant effects of breakdown on the non-oscillatory component.

According to Balcombe and Parker,<sup>(34)</sup> effects of magnetic breakdown should appear primarily for H in the (001) plane and should be most pronounced for H along the

[010] axis. In such a case the largest effect of breakdown on  $S$  would be expected for  $H$  along [010], a smaller effect for  $H$  along [110], and the smallest effect for polycrystalline samples. Indeed this is just what is observed for the oscillatory component: there are giant quantum oscillations for  $H$  along [010]; oscillations an order of magnitude smaller for  $H$  along [110]; and no evidence of quantum oscillations in comparable purity polycrystalline samples. On the other hand, as regards the non-oscillatory component little difference is found between the values of  $\Delta A$  for  $H$  along [010] and along [110] and both values are consistent with those obtained with polycrystalline samples by Averbach, et. al.<sup>(4)</sup> Therefore, it is concluded that magnetic breakdown does not significantly affect this component, and thus the values for  $\Delta A$  should be amenable to the calculation of Opsal and Wagner,<sup>(8)</sup> provided that the electron-phonon mass enhancement is included.

### 3.5 Phonon Drag

Besides measuring the electron diffusion contribution to  $S$ , our experiments also provide information concerning the phonon drag contribution. Recalling from eq. (IV.1) that  $S_g$  is simply  $B(H)T^3$ , it follows that the slopes of the lines in Figure IV.2 give  $B(H)$ . The values of  $B(H)$  for the aluminum single crystal are shown in Table IV-1.



Table IV-1: Values of  $B(H)$  for Al(Ga) Sample

$B(\times 10^{-10} \text{V/K}^4)$	H
$-3.2 \pm 1.5$	15kG, H    {110}
$-2.1 \pm 0.9$	15kG, H    [010]
$-0.5 \pm 1.5$	15kG, H    [100]
$-1.0 \pm 0.6$	0.0kG.

The variance of  $B$  with magnetic field and also the measured values of  $B$  are similar to the results reported by Averback, et. al.<sup>(4)</sup> The fact that  $B(H)$  is negative may indicate that the A type scattering events of Figure III.3 predominate over the B type events (see section III.B). Averback, et. al. noted that they were unable to find any quantitative feature of the variation of  $B$  with  $H$  which was impurity independent. They therefore concluded that the magnitude of the observed variation of  $B$  with  $H$  is not an intrinsic property of the host metal aluminum, but is determined primarily by the details of the scattering of electrons by impurities. No detailed explanation of the observed variation of  $B$  with  $H$  has been offered to date.

One must be cautious when interpreting  $B$  as solely a measure of phonon drag. If the scattering is partially inelastic, then the electron diffusion magnetothermopower, in the presence of a magnetic field may also contain terms which are non-linear in  $T$ .<sup>(35)</sup> If these

contributions are small compared to the linear term, then an  $S/T$  vs.  $T^2$  plot will incorporate these contributions into  $B$  (the slope). The magnitude of inelastic scattering may be estimated by examination of the variation of the Lorentz ratio with temperature. Lorentz ratio data from an aluminum sample of comparable purity by Willot<sup>(36)</sup> shows that this ratio changes about 10% between 0 and 4K. This could cause  $S_d/T$  to vary by at least several percent over this temperature range; moreover, the variation is expected to be field dependent. Since  $S/T$  varies by only 25% over this temperature range, we conclude that inelastic scattering could make a non-negligible contribution to  $B$ .

Nielson and Taylor<sup>(37)</sup> have shown that second order multiphonon scattering processes may also give a  $T^3$  contribution to  $S_d$ ; the so-called "phony phonon drag." Bourassa has estimated the size of the "phony phonon drag" for aluminum in the absence of a magnetic field and finds it to be orders of magnitude smaller than the observed values of  $B$ .<sup>(4)</sup> Currently the effect of a magnetic field on "phony phonon drag" is unknown. In conclusion, although the coefficient  $A(H)$  gives a quantitative measure of  $S_d$  in the zero temperature limit, the experimental value of  $B(H)$  does not necessarily measure only  $S_g$ . We therefore believe that a detailed theoretical analysis of  $B(H)$  solely in terms of phonon drag, may be a bit premature at this time.

#### 4. Summary and Conclusions for Aluminum

Transverse magnetothermopower measurements of a single crystal aluminum sample (containing 50 ppm Ga) have been made with H along both the {010} and {110} families of axes. In each case S was consistent with the form  $S(H) = A(H)T + B(H)T^3$ , allowing a separation of  $S_d$  from  $S_g$ , and therefore permitting a determination of the quantity  $\Delta A$ . For H along the four-fold symmetric {010} an average value of  $\Delta A = (2.23 \pm 0.25) \times 10^{-8} \text{V/K}^2$ , was obtained, and for H along the two-fold symmetric {110} axes a value of  $\Delta A = (2.0 \pm 0.2) \times 10^{-8} \text{V/K}^2$  was obtained. These values differ only slightly, and they agree with the values previously reported by Averbach, et. al.<sup>(4)</sup> for polycrystalline samples. We have argued above that these values are appropriate for comparison with the calculations of Opsal and Wagner.<sup>(8)</sup> This comparison leads to good agreement, provided that a 45% electron-phonon mass enhancement is included. A 45% enhancement factor is consistent with that independently obtained from other types of measurements. The fact that  $\Delta A$  is somewhat smaller for H along the two-fold symmetric axis than for H along the four-fold symmetric axis is also in agreement with Opsal and Wagner's calculations.

Data was also obtained for  $S_g = B(H)T^3$ . The values of B(H) are shown in Table IV-1 and agree with the values previously reported by Averbach, et. al.<sup>(4)</sup> for

polycrystalline samples. We have noted that these values of  $B(H)$  may not be solely a measure of  $S_g$ .

## B. Indium

### 1. Introduction

Indium and aluminum are both Group III metals. Aluminum crystallizes in a face centered cubic structure for which the  $\{100\}$  family of axes are all four-fold symmetric. In contrast, indium crystallizes in a face centered tetragonal structure ( $c/a = 1.08$ ) for which the  $[001]$  axis is four-fold symmetric but the  $[100]$  and  $[010]$  axes are only two-fold symmetric. Thus, it seemed quite natural to extend the magnetothermopower measurements made on aluminum, to indium single crystals for  $H$  aligned along both the  $[010]$  and  $[001]$  directions, in order to try to observe the effect of the slight tetragonal distortion on  $\Delta S_d$ .

Although the Fermi surfaces of aluminum and indium are quite similar, previous measurements of their magnetothermopowers by Caplin, et. al.<sup>(38)</sup> gave apparently different results. They measured the magnetothermopowers of aluminum and indium polycrystals over the temperature range 4.2 to 60K in magnetic fields up to 50kG. The significant difference between the results of the two metals showed up in the quantity  $\Delta S(H)$  ( $\Delta S(H) \equiv S(H) - S(H = 0)$ ). Only in aluminum did  $\Delta S(H)$  change sign from positive to negative

as the temperature was increased. In indium,  $\Delta S(H)$  remained negative at all temperatures investigated.

Using magnetic fields less than 50kG., Caplin, et. al. also noticed that  $S$  tended to saturate at high fields for  $T < 21K$  for aluminum and for  $T < 9K$  for indium. Saturation indicates that the high field limit ( $\omega_c \tau \gg 1$ ) has been reached. They also measured the thermopower of indium single crystals over the temperature range 4.2 to 300K in zero magnetic field. They observed that  $S$  was always more positive for  $\vec{V}T$  along [100] than for  $\vec{V}T$  along [001].

Averback and Bass<sup>(39)</sup> performed measurements on polycrystalline indium samples in the temperature range 2 to 5K in magnetic fields up to 20kG. Comparison of the data of Averback and Bass with that of Caplin, et. al. shows a discrepancy in the sign of  $S$ . Measurements performed during the course of this thesis indicate that the sign given by Averback and Bass is incorrect.<sup>(40)</sup> Averback and Bass also observed that  $S$  saturated in high magnetic fields. In addition, they noted that  $S$  did not fit the simple form:  $S(H,T) = A(H)T + B(H)T^3$ . Two possible reasons are:

- (1) The low temperature approximation of  $S_g$  ( $= BT^3$ ) may not be adequate. However, if elastic impurity scattering is still the major scattering mechanism then

$$S(H,T) = A(H)T + S_g(H,T) . \quad (IV.3)$$

For this case, if a term linear in  $T$  can be extracted from the data then  $S_d$  can be separated from  $S_g$  (assuming  $S_g$  does not contain a term linear in  $T$ ).

(2) If there is a significant amount of inelastic scattering, then  $S_d$  will no longer be linear in  $T$ . In this case  $S_d$  cannot be unambiguously separated from  $S_g$ .

Blatt, et. al.<sup>(41)</sup> measured the electrical resistivity of polycrystalline indium wires. The RRRs of Blatt, et. al.'s samples were comparable to the RRRs of Averback and Bass' samples. Blatt, et. al.'s data show that the electrical resistivity is strongly temperature dependent between 2.0 and 4.2K. This indicates that there is a significant amount of electron-phonon (inelastic) scattering at 4K. Thus, when the present study began it seemed possible that reason (2) could be the cause of deviation of  $S$  from the simple form of eq. (IV.1).

In this thesis, measurements similar to those of Averback and Bass were performed on oriented single crystals of dilute indium alloys. It was anticipated that added impurities would increase the electron-impurity scattering to where it would finally dominate the inelastic scattering, causing  $S_d$  to become linear in  $T$  for  $T < 5K$ , and thereby allowing a separation of  $S_d$  from  $S_g$ .

On the other hand, the alloys must be very dilute in order to reach the high field limit with  $H < 20\text{kG}$ . In addition to measuring  $S$ , both the electrical and thermal conductivities were measured as functions of  $H$  and  $T$ . This allowed calculation of the Lorenz ratio  $L$  as a function of  $H$  and  $T$ . The divergence of  $L$  from  $L_0$  ( $= 2.443 \times 10^{-8}$  watt-ohms/ $\text{K}^2$ ) gives a measure of the amount of inelastic scattering present at a given  $T$ . The variation of  $L$  with  $T$  gives a more sensitive measure of the amount of inelastic scattering than does the electrical resistivity alone.

To summarize, the aims of the magnetothermopower measurements on indium were:

- (1) To see the effect of the slight tetragonal distortion on  $\Delta S_d$  by measuring  $S$  with  $H$  aligned along both the four-fold symmetric  $[001]$  axis and the two-fold symmetric  $[010]$  axis.
- (2) In order to achieve goal (1) it is necessary to separate  $S_d$  from  $S_g$ . We hoped to do this by adding impurities to increase the electron-impurity scattering to a point where it finally dominates the inelastic scattering, causing  $S_d$  to become linear in  $T$  for  $T < 5\text{K}$ .
- (3) By extending the magnetothermopower measurements on indium down to  $1.5\text{K}$  we wanted to see whether  $\Delta S(H)$  would change sign from negative to positive as the temperature was decreased, as it does in aluminum.

## 2. Data and Analysis

Figures IV.3 - IV.8 show magnetothermopower data for a variety of indium crystals. The data are plotted in the form  $S/T$  vs.  $T^2$  at constant  $H$ . Although in some cases for a particular  $H$  the data lie on straight lines, not a single sample produced data which lay on straight lines for all  $H$ . This demonstrates that the magnetothermopower of indium, in contrast to that of aluminum, does not obey the simple form:  $S(H,T) = A(H)T + B(H)T^3$  throughout the temperature range 1.5 to 5K.

Figure IV.9 shows a plot of  $S$  vs.  $H$  at both 4.71K and 3.50K for a sample containing 100 ppm tin in indium (In(Sn)-II). The data appear to be approaching saturation, but have not reached saturation at  $H = 20\text{kG}$ . Presumably this non-saturation by 20kG stems from the fact that the sample contains 100 ppm tin; this places an upper limit of about 100 ppm on the impurity content of the indium alloys if the high field limit is to be attained with the present measuring system. The fact that the data appear to be approaching saturation, is in agreement with the behavior found by both Caplin et. al.<sup>(39)</sup> and Averback and Bass.<sup>(40)</sup>

A goal of this research was to test the hypothesis that  $S$  would fit the simple form of eq. (IV.1) throughout the temperature range 1.5 to 5K for sufficiently high impurity concentrations. Therefore measurements were



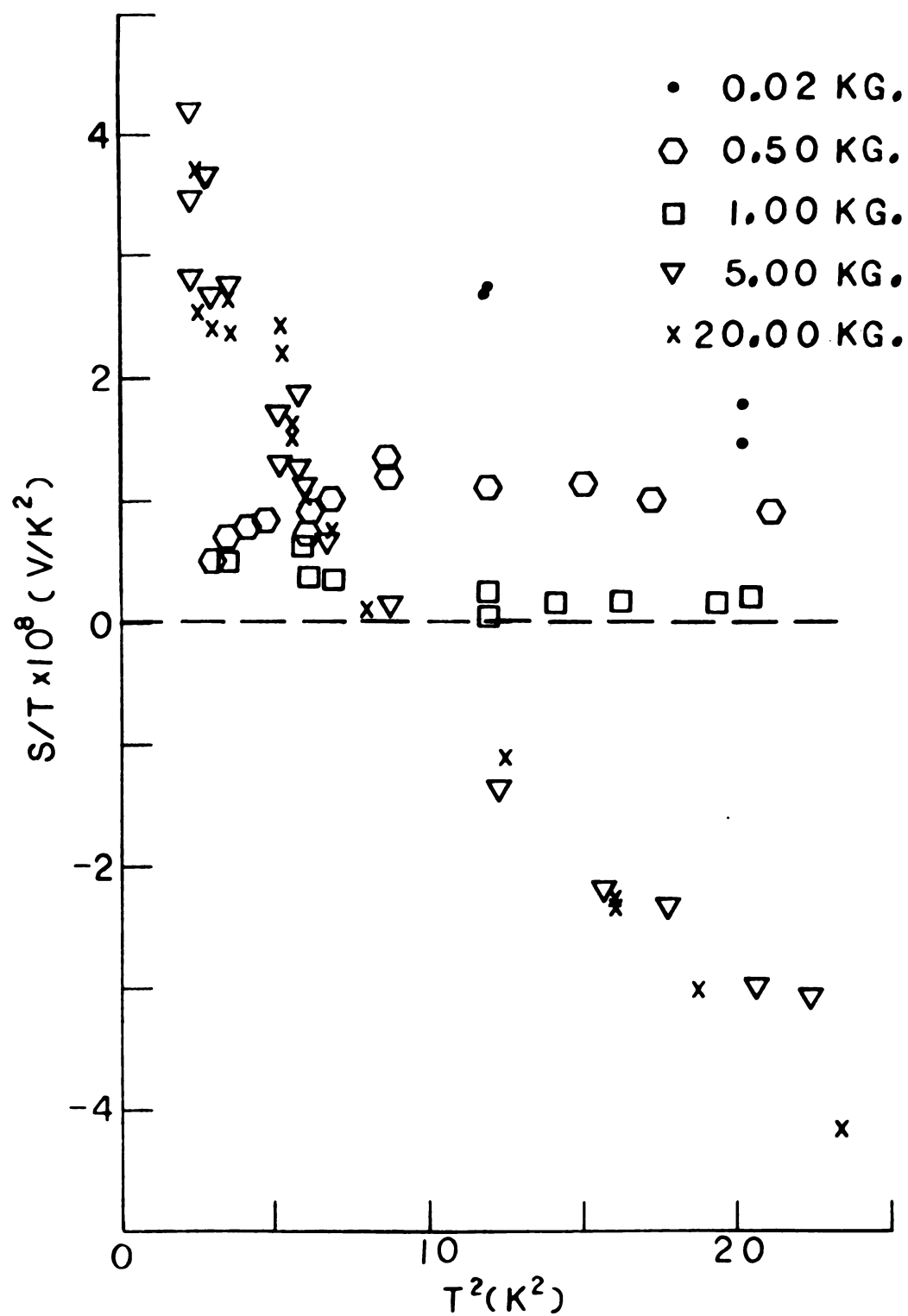


Figure IV.3: The temperature dependence of the non-oscillatory component of  $S$  for sample In(Ga) with  $H$  directed along  $[010]$ .

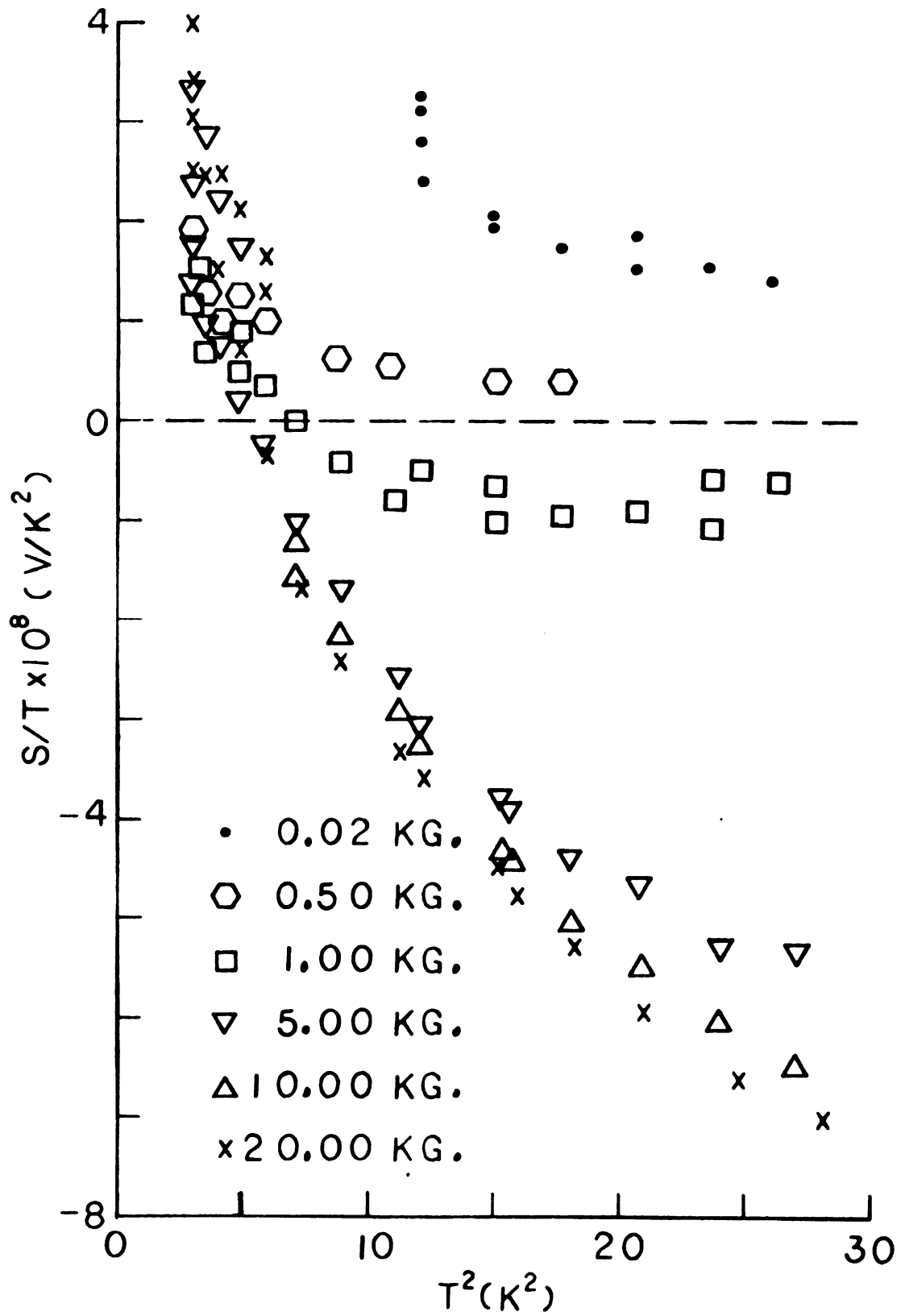


Figure IV.4: The temperature dependence of the non-oscillatory component of  $S$  for sample In(Ga) with  $H$  directed along  $[001]$ .

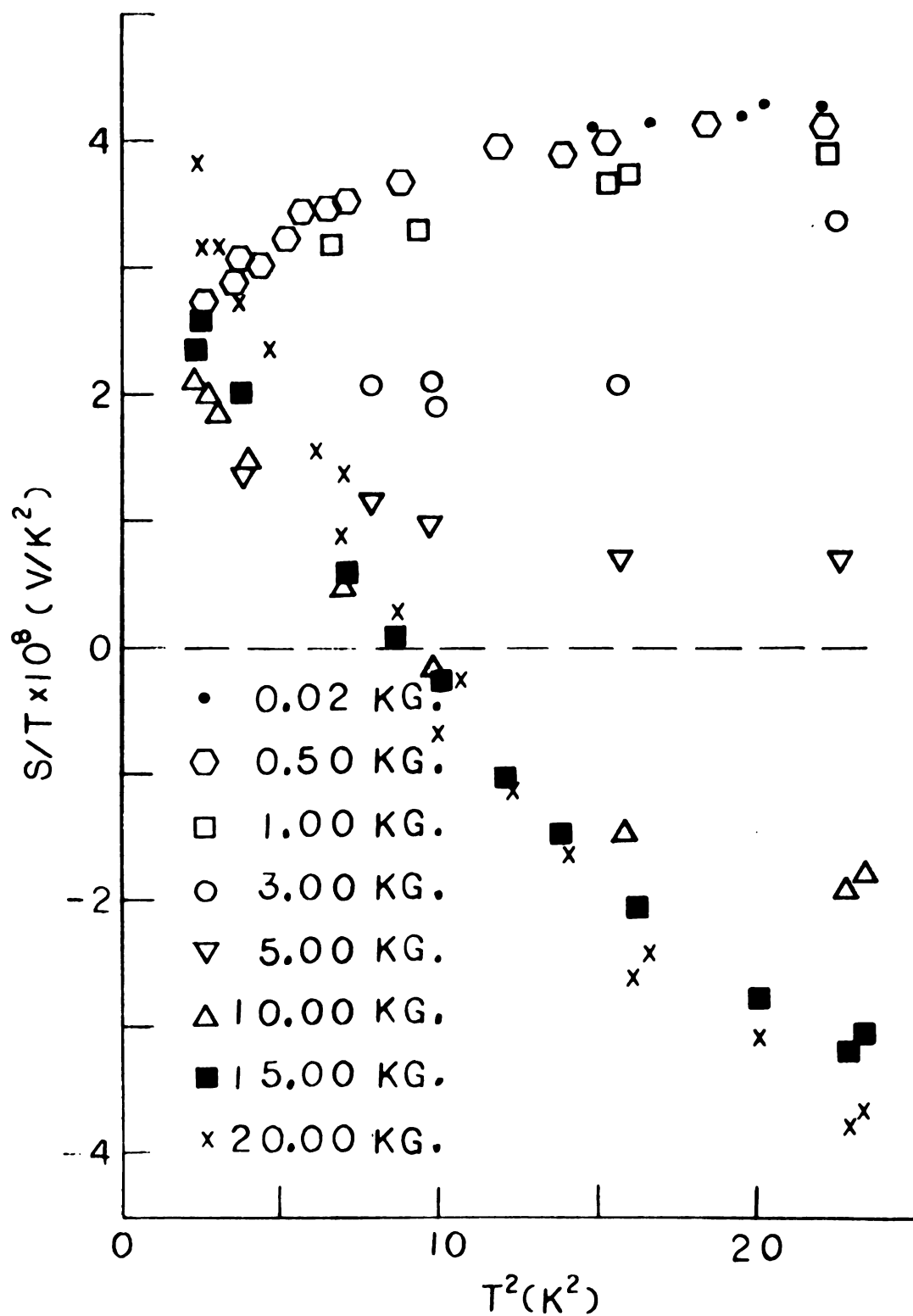


Figure IV.5: The temperature dependence of the non-oscillatory component of  $S$  for sample In(Sn)-II with  $H$  directed along  $[001]$ .

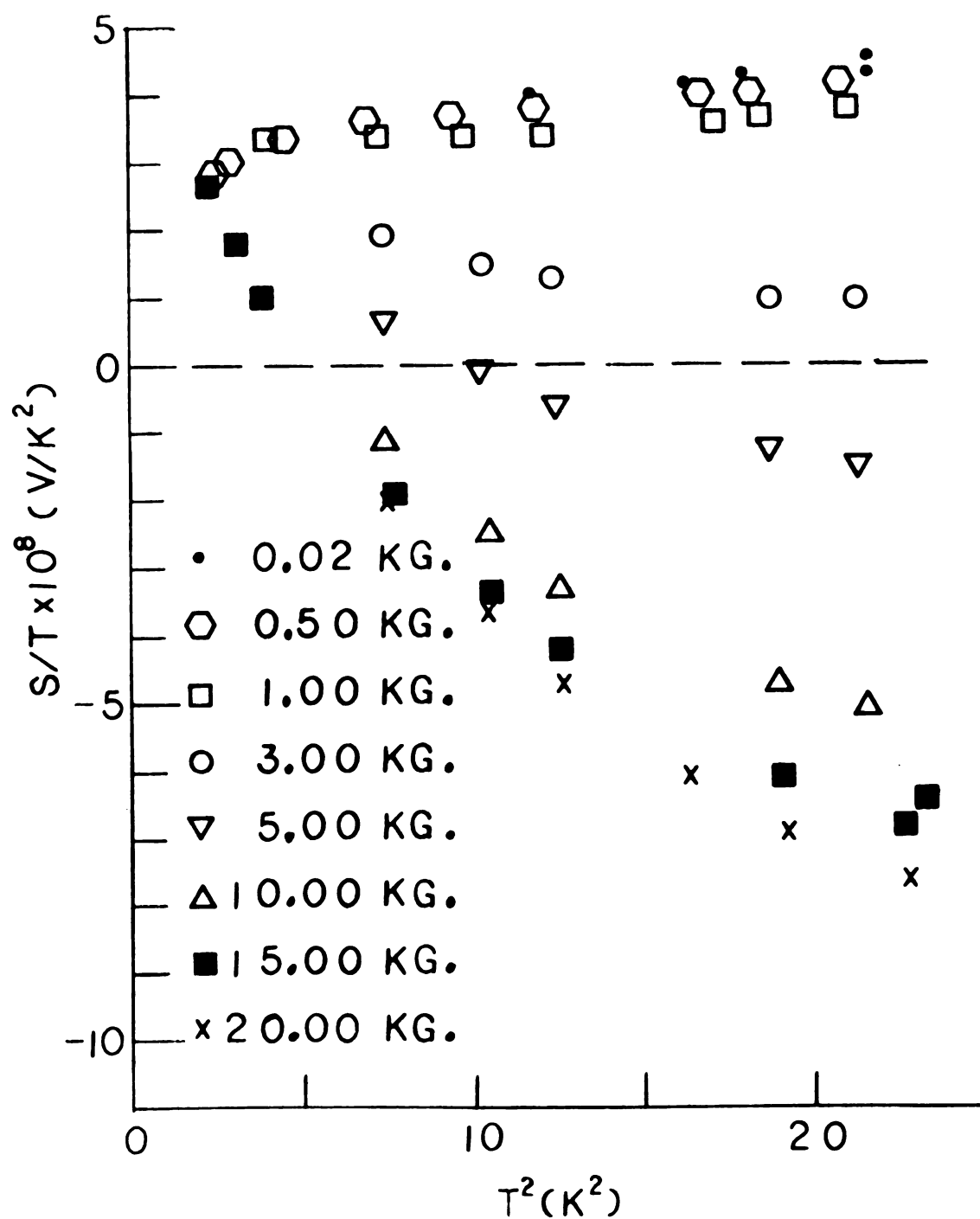


Figure IV.6: The temperature dependence of the non-oscillatory component of  $S$  for sample In(Sn)-II with  $H$  directed along  $[1\bar{1}0]$ .

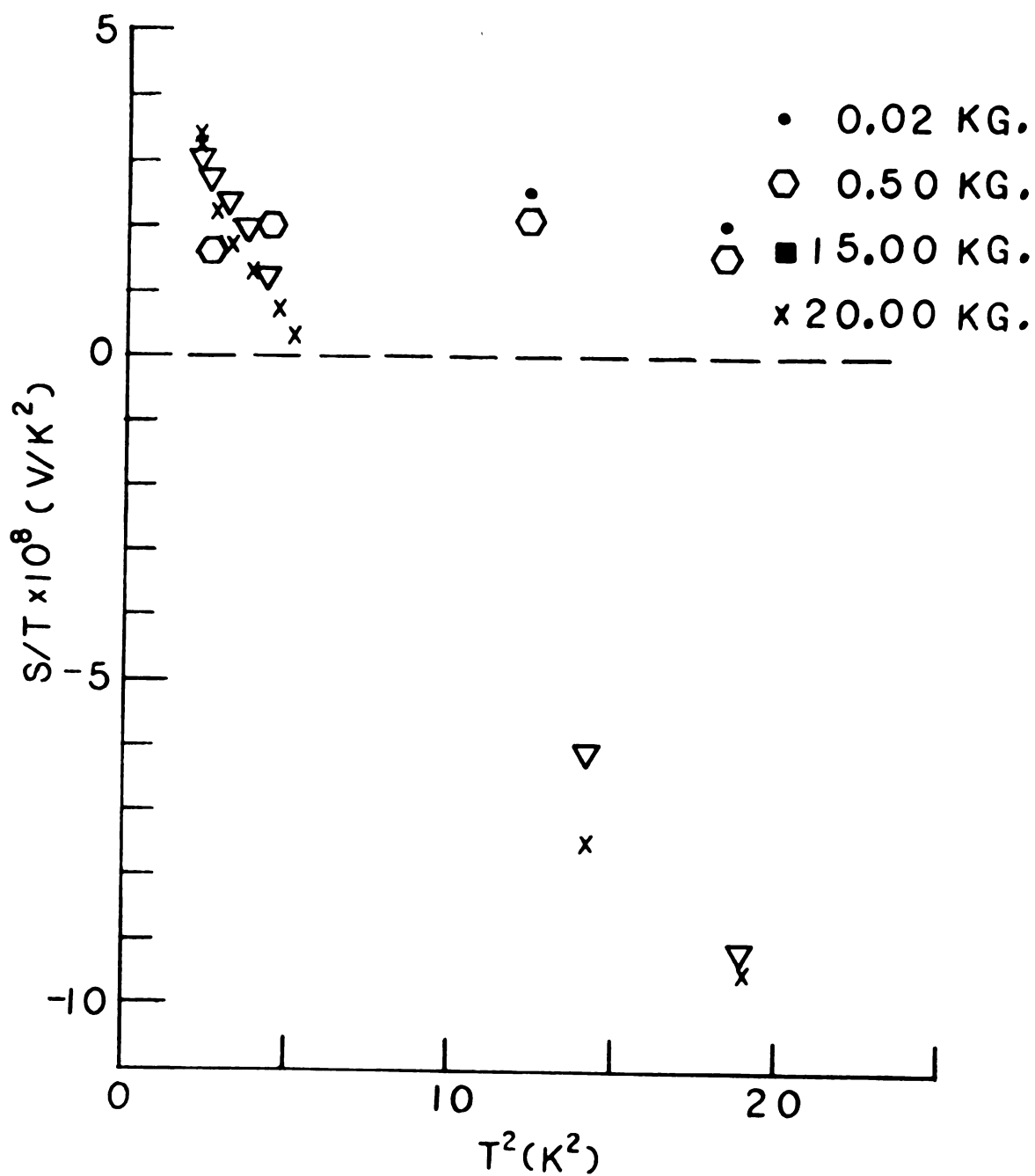


Figure IV.7: The temperature dependence of the non-oscillatory component of  $S$  for sample In(Sn)-I with  $H$  rotated  $12^\circ$  from the  $[\bar{1}01]$  in the  $(101)$  plane.

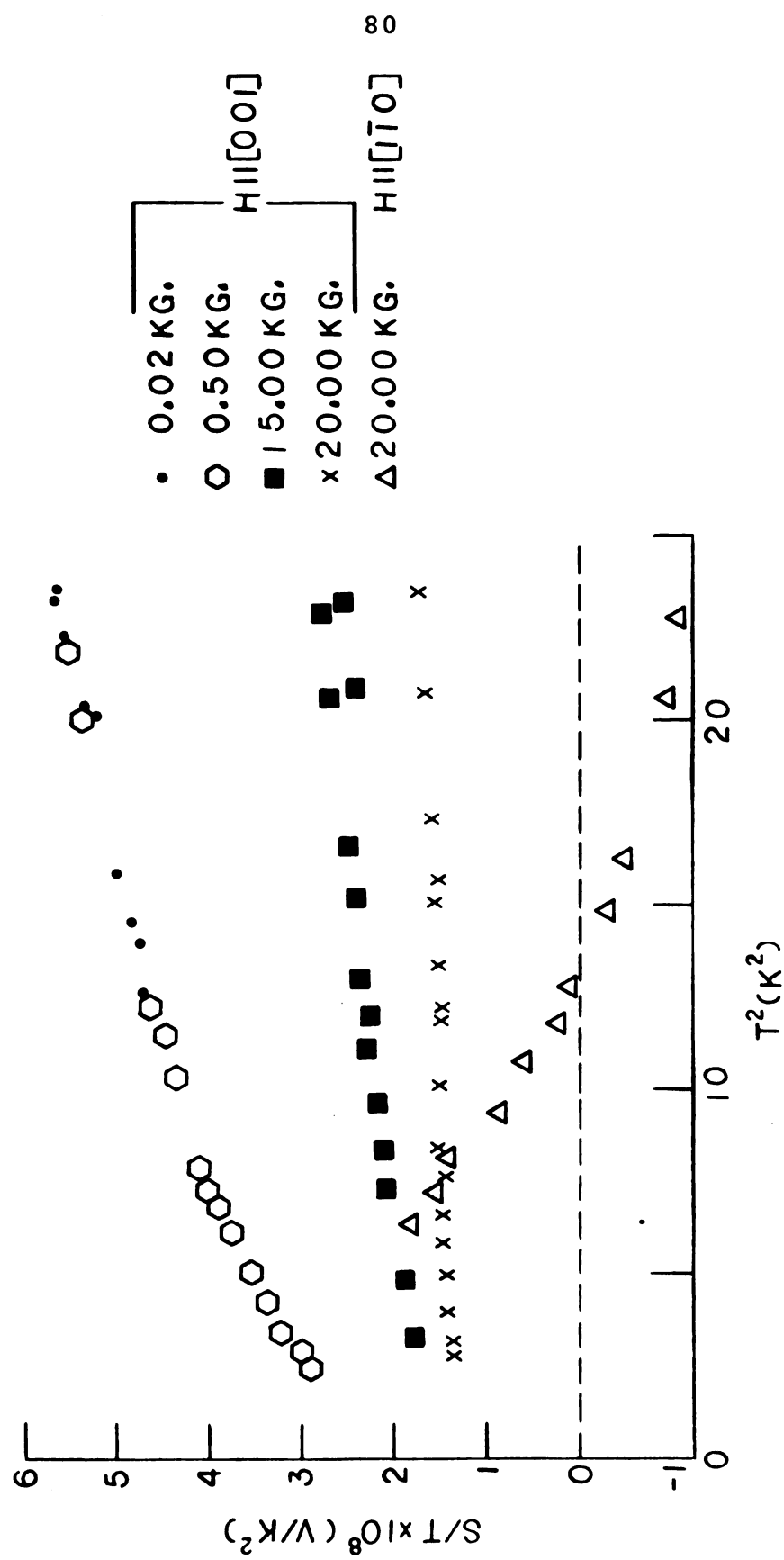


Figure IV.8: The temperature dependence of the non-oscillatory of S for sample  $\frac{\text{In(Sn)}-\text{III}}{80}$ .

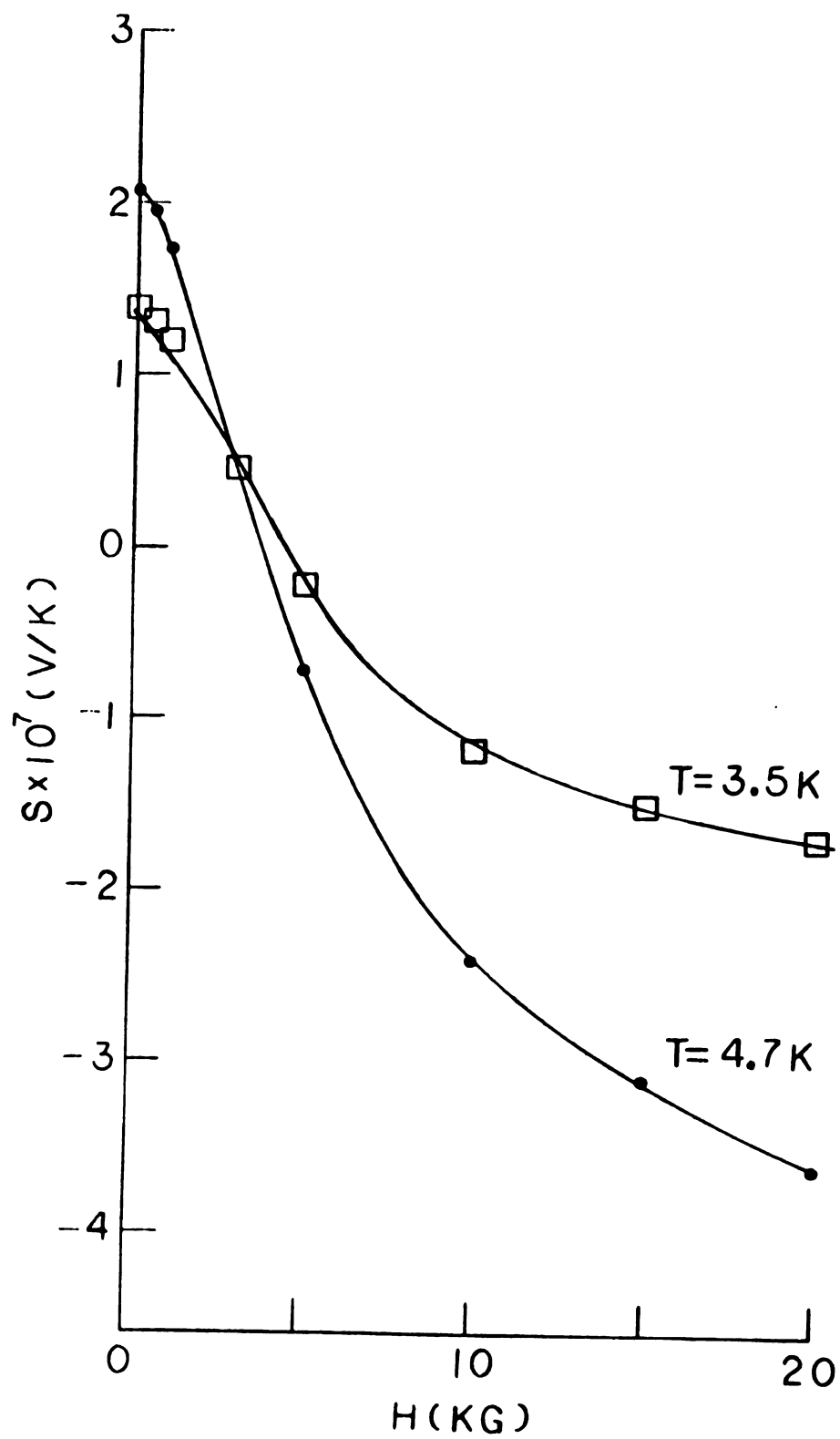


Figure IV.9: The magnetic field dependence of  $S$  for sample In(Sn)-II with  $H$  directed along  $[1\bar{1}0]$ .

performed on a sample containing 500 ppm tin in indium (In(Sn)-III). Figure IV.8 shows that the data for  $H = 15\text{kG}$  and  $20\text{kG}$  with  $H$  directed along the  $[001]$  axis lie on straight lines. This tempts one to make the hypothesis that all the data for  $H > 15\text{kG}$  will also lie on straight lines. However, one must also note that for this sample  $H = 20\text{kG}$  is a relatively low field ( $\omega_c\tau < 1$ ); and as illustrated by Figure IV.6 the form of an intermediate field ( $H = 3\text{kG}$  or  $5\text{kG}$ ) curve over a limited temperature range ( $10 < T^2 < 25\text{K}^2$ ) can be quite different from the high field curves ( $H > 15\text{kG}$  in Figure IV.6). In fact these intermediate field curves over this limited temperature range are quite similar to the curves for  $H = 15$  and  $20\text{kG}$  with  $H$  directed along the  $[001]$  axis of Figure IV.8. Therefore, since intermediate field curves are not reliable indicators of the high field curves, and also because the  $H = 0.50\text{kG}$  data do not lie on a straight line, we believe that  $S$  will not fit the simple form of eq. (IV.1) at higher fields over our available temperature range. Figure IV.8 shows that the data for  $H$  directed along the  $[1\bar{1}0]$  axis deviate strongly from a straight line already at  $20\text{kG}$ . So it is concluded that for an arbitrary  $H$ ,  $S$  will not fit the simple form of eq. (IV.1) throughout the temperature range 1.5 to  $5\text{k}$  for indium samples with impurity concentrations less than 500 ppm.



The nonlinearity of Figures IV.3 - IV.8 is most pronounced in the temperature region above 3K ( $T^2 = 9K^2$ ). The experimental data of Caplin, et. al. show a strong negative peak in the vicinity of 10K. They ascribe this peak to phonon drag. It seems likely that the available temperature range is too close to the phonon drag peak and therefore  $S_g$  cannot be adequately described by the low temperature approximation ( $S = BT^3$ ). As a rule of thumb, the phonon drag peak occurs between  $\theta_D/5$  and  $\theta_D/7$  ( $\theta_D$  is the Debye temperature). Averbach and Bass tentatively attributed the inadequacy of the low temperature description in the temperature region above 3K, to the low Debye temperature of indium ( $\theta_D = 110K$ ); aluminum which has a much higher Debye temperature ( $\theta_D = 425K$ ), begins to deviate from the simple form:  $S(T) = AT + BT^3$  above about 6K. (42)

The other apparent cause of the non-linear  $S/T$  vs.  $T^2$  plots for indium concerns the effects of the inelastic scattering on  $S_d$ . For this case, it would be expected that a sample with a significant amount of inelastic scattering would produce a different  $S/T$  vs.  $T^2$  plot when compared with that of a sample with a smaller amount of inelastic scattering. Figure IV.10 shows the Lorenz ratio as a function of  $T$  for a few samples. The deviation of  $L/L_0$  from 1 gives an indication of the amount of inelastic scattering present. This deviation is

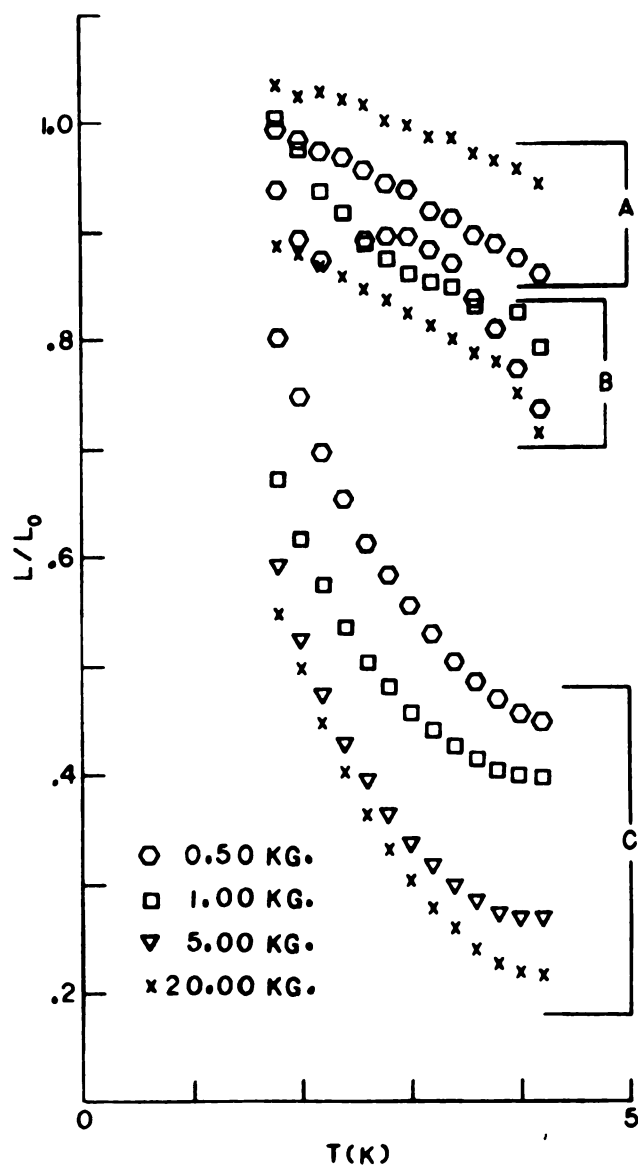


Figure IV.10: The temperature dependence of the Lorenz ratio  $L$  divided by the ideal Lorenz ratio  $L_0$  for samples:  
 A) In(Sn)-III, with  $H$  directed along  $[001]$ ;  
 B) In(Sn)-II, with  $H$  directed along  $[001]$ ;  
 C) In(Ga), with  $H$  directed along  $[010]$ .

largest in our purest sample, In(Ga) (RRR = 7400). The fact that  $L$  deviates most from  $L_0$  is expected since this sample should have the least electron-impurity (elastic) scattering. Figure IV.10 also shows that sample In(Ga) exhibits significantly more inelastic scattering than sample In(Sn)-II. However, Figures IV.3 - IV.6 show that these two samples produce similar  $S/T$  vs.  $T^2$  plots. Thus it is concluded that the major cause of the nonlinearity of Figures IV.3 - IV.8 in the region  $T > 3K$  is the breakdown of the low temperature description of  $S_g$ , rather than the influence of inelastic scattering on  $S_d$ .

Probably the most interesting region in Figures IV.3 - IV.8 is below 2.5K ( $T^2 < 6K$ ). For all samples except In(Sn)-III, the high field set of data ( $H > 10kG$ ) either becomes more positive than the 0.50kG set (essentially  $H = 0$ ) or it appears that this will happen at a temperature somewhat below 1.5K (the lowest temperature attainable with the present system). This behavior was not suggested by any previously published data. However, such behavior would be expected when  $S_d$  is the dominant component of  $S$ . Moreover, the only abnormal case, In(Sn)-III, can be understood by noting that this sample has not reached the high field limit by 20kG, and we previously argued that the intermediate field curves over a limited  $T$  range do not reliably predict the high field  $S/T$  vs.  $T^2$  curves. The general low temperature behavior

of these samples is qualitatively similar to that of aluminum, which is only slightly affected by phonon drag. Perhaps this low temperature region is far enough removed from the large negative phonon drag peak, so that  $S_d$  is comparable to  $S_g$ , in which case  $S$  might be described by the simple form of eq. (IV.1). However, this is only a conjecture concerning the scattering mechanisms responsible for  $S$ . The true test will come when magnetothermopower measurements are performed at still lower temperatures ( $0.3 < T < 1.5K$ ). At such low temperatures elastic, electron-impurity scattering should be dominant, so  $S_d$  should be linear in  $T$ , and moreover,  $S_g$  should be small compared with  $S_d$ .

### 3. Umkehreffect

Samples In-I and In(Sn)-I demonstrated an interesting umkehreffect. The umkehreffect is characterized by the magnetothermopower changing drastically upon reversal of  $H$ . Figures IV.11 and IV.12 show this effect. For  $H$  near  $[100]$  the magnetothermopower changes by a factor of two upon field reversal, Figure IV.12 also shows the angular variation of the electrical resistance. It is clear that the resistance, in contrast to the magnetothermopower, is well behaved, i.e. not affected by field reversal.

Such a result can be understood (at least qualitatively) by considering the properties of the  $\vec{\rho}$  and

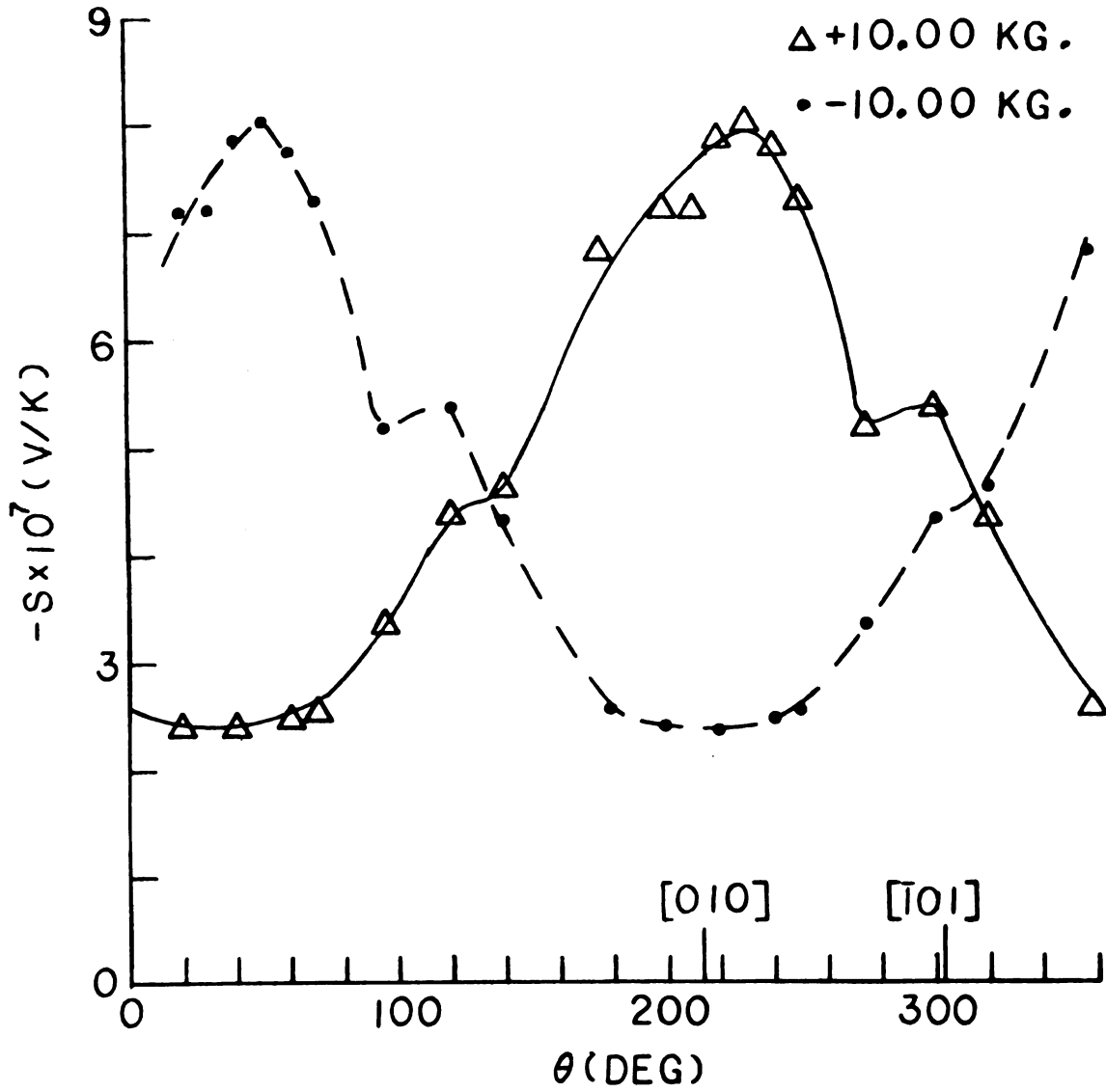


Figure IV.11: Variation of  $S$  with rotation angle  $\theta$  at  $H = 10\text{kG}$  and  $T = 4.7\text{K}$  for sample In-I.  $H$  was rotated about the  $[101]$  axis.  $\theta = 213^\circ$  corresponds to  $H$  directed along  $[010]$ .

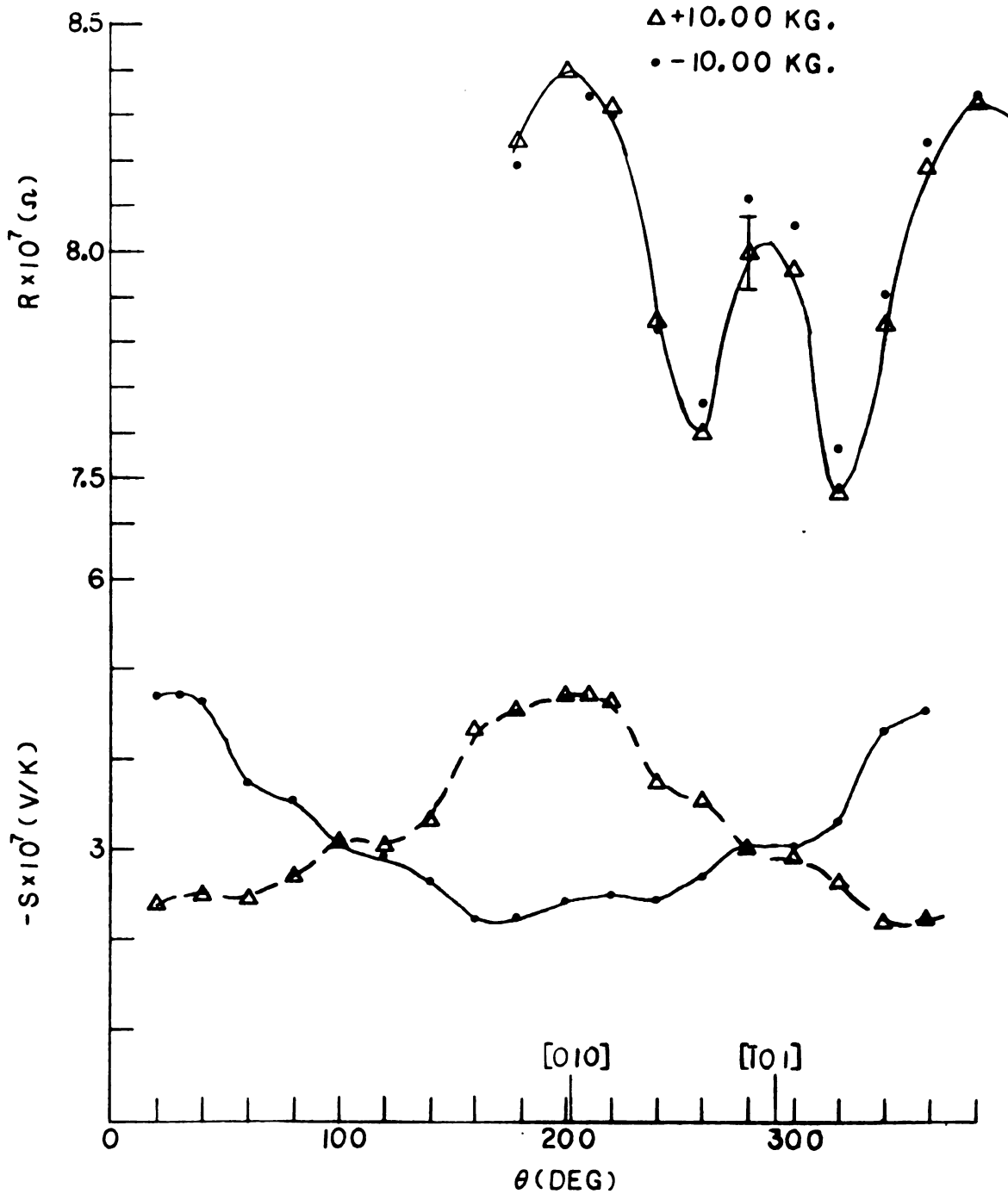


Figure IV.12: Variation of  $R$  (upper curve) and  $S$  (lower curve) with rotation angle  $\theta$  at  $H = 10\text{kG}$  for sample  $\text{In(Sn)-I}$ .  $H$  was rotated about the  $[101]$  axis.  $\theta = 202^\circ$  corresponds to  $H$  directed along  $[010]$ . The  $R$  curve was measured at  $4.2\text{K}$  and the  $S$  curve at  $4.3\text{K}$ .

the  $\overleftrightarrow{S}$  tensors. For either tensor, symmetry requires that there be no umkehreffect for H directed along a three-fold or higher symmetry axis. As a consequence of the Onsager relation  $\rho_{ik}(\vec{H}) = \rho_{ki}(-\vec{H})$  <sup>(16)</sup> there can be no magnetoresistance umkehreffect for H directed along a two-fold symmetry axis either. However, since there is no such Onsager relation connecting components of the  $\overleftrightarrow{S}$  tensor, H must be directed along a three-fold or higher symmetry axis for the magnetothermopower umkehreffect to vanish. Since the [100] axis is only a two-fold symmetric axis, it follows that the magnetothermopower may exhibit an umkehreffect. Although such symmetry arguments allow the existence of an umkehreffect, they alone do not predict its magnitude. Therefore, one cannot on theoretical grounds alone unambiguously attribute the observed magnetothermopower umkehreffect to an intrinsic property of indium as opposed to an experimental artifact (e.g. lead misalignment or sample preparation). To see if the observed umkehreffect was due to a small misalignment of the voltage leads attached to the sample, the leads were removed and reattached, aligned as accurately as possible. This had no significant effect on the measured value of S. Therefore, it is concluded that lead misalignment was not the principal cause of this irregular behavior.

Samples In-I and In(Sn)-I were both grown from the same seed. Figures IV.11 and IV.12 show that both

samples exhibit the largest umkehreffect when H is in the vicinity of [100]. H could also be aligned along [100] with sample In(Sn)-III. The umkehreffect exhibited by In(Sn)-III, as well as all other samples, was less than 20%; therefore, it is concluded that the very large umkehreffect exhibited by In-I and In(Sn)-I is not intrinsic to H along [100]. Although it seems unlikely, one cannot rule out the hypothesis that this large effect is a consequence of  $\vec{Q}$  being directed along [011]. Therefore, further measurements on independently grown single crystals are necessary to determine whether the aforementioned hypothesis is correct or whether the large umkehreffect was an experimental artifact due to sample preparation, which did not show up in the X-ray (Laue) patterns.\* It should be noted that Figure IV.7 shows data for a direction in which the umkehreffect was less than 10%.

#### 4. Summary and Conclusions for Indium

We briefly summarize the qualitative results for indium: (1) Magnetothermopower measurements performed on indium single crystals containing as much as 500 ppm impurity showed that S was not consistent with the simple

---

\* It is unclear whether or not higher quality X-ray photographs would have shown a difference between these two samples and the other indium samples.



form:  $S(H,T) = A(H)T + B(H)T^3$ , over the temperature range 1.5 to 5K. It is concluded that the deviation from this simple form is not primarily due to the effects of inelastic scattering on  $S_d$ , but rather to the influence of the large negative phonon drag peak (near  $T = 10K$ ), which causes  $S_g$  to substantially deviate from the form  $S_g = B(H)T^3$ .

(2) The magnetothermopower of samples with impurity concentrations of 100 ppm or less appear to be approaching saturation for  $H = 20kG$  and  $T < 5K$ .

(3) At high temperatures,  $3 < T < 5K$ ,  $S$  becomes more negative with increasing  $H$ . This is presumably due to  $S_g$  dominating  $S$ .

(4) At low temperatures,  $1.5 < T < 2.5K$ , the high field limit of  $S$  is more positive than the low field values. This can be understood by assuming that  $S_d$  is increasing relative to  $S_g$  with decreasing  $T$ . The temperature at which  $S$  starts becoming more positive instead of more negative with increasing field varies somewhat from sample to sample.

## V. OSCILLATORY THERMOELECTRIC PHENOMENA - THEORY

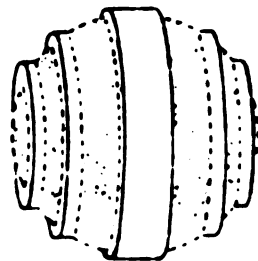
### A. Variation of the Density of States at $\epsilon_F$ with H

The state of a free non-interacting electron gas can be described by a sphere in single particle momentum space (k-space). At  $T = 0$  the interior of the sphere has an electron occupying every single particle state, while the exterior states are all empty. The Fermi surface separates the occupied and unoccupied regions.

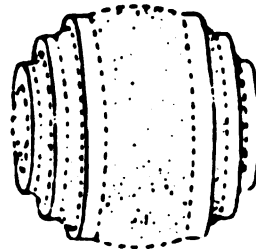
In the absence of a magnetic field the single particle states of the electrons are evenly distributed throughout all of k-space. However, the application of a magnetic field redistributes these states on to the surfaces of cylinders aligned parallel to the magnetic field. Figure V.1 shows such a redistribution of states. This figure also shows the H dependence of this redistribution. An electron, in any particular state, orbits around the circumference of the cylinder ("Landau cylinder") with an angular frequency  $\omega_c$  (the so-called cyclotron frequency), given by

$$\omega_c = \frac{eH}{m_e c} . \quad (V.1)$$

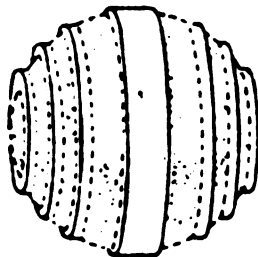
where  $m_e$  is the mass of the electron and  $c$  is the speed



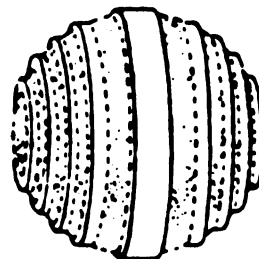
(a)



(b)



(c)



(d)

Figure V.I: Variation of the Fermi surface with field, showing the increasingly spherical shape as the field becomes weaker. The field decreases going (a) to (d) (after Adams and Holstein(43)).

of light (in a vacuum). Thus, the effect of the magnetic field is to quantize the electron orbits in k-space.

The radii of these cylinders increase with  $H$ . As the outer cylinder passes through the Fermi surface, the electrons on this cylinder "condense" back onto available states on lower energy (smaller radius) cylinders. This process repeats as each Landau cylinder passes through the Fermi surface, giving rise to an oscillatory magnetic field dependence of the density of states at the Fermi level. This dependence has been observed in measurements of a number of high field ( $\omega_c \tau \gg 1$ ) electronic properties such as magnetization (de Haas-van Alphen effect) or electrical resistivity (de Haas-Shubnikov effect).

The exact solution of the free electron gas in a uniform magnetic field is given in many solid state physics texts.<sup>(44)</sup> One finds that the oscillations in the density of states at the Fermi energy are periodic in  $1/H$ , with a period

$$\Delta(1/H) = \frac{2\pi e}{\hbar c} A \quad (V.2)$$

where  $A$  is the cross-sectional area enclosed by the electron's orbit.

What happens when we are dealing with electrons in real metals? In some metals, such as indium and aluminum, the valence electrons can be treated as nearly free electrons (NFE). The NFE approach treats the crystal

lattice potential as a perturbation. The important changes introduced by NFE treatment are:

- (1) The electron orbits (and consequently the Fermi surface) are no longer spherical.
- (2) The Fermi surface can be made up of pieces from more than one band.
- (3) The dynamics of the electrons in their orbits are described in terms of an "effective mass"  $m^*$  where

$$m^* = \frac{1}{2\pi} \frac{\partial A}{\partial \epsilon} \Big|_{\epsilon=\epsilon_F} \quad (V.3)$$

Using the Correspondence Principle, it can be shown that electrons within a single band will still exhibit an oscillatory density of states at the Fermi level which is periodic in  $1/H$ .<sup>(44)</sup> The period is still given by eq. (V.2), but now  $A$  is the extremal cross-sectional area of the Fermi surface in the plane perpendicular to the magnetic field.

#### B. Estimate of S Oscillations Due to Density of States Oscillations for Aluminum and Indium

There do not exist any rigorous calculations of the oscillatory component of the thermopower of a metal which are suitable for quantitative comparison with experiment. Only simplified calculations of limited applicability by Zil'berman,<sup>(45)</sup> Horton,<sup>(46)</sup> Grenier, et. al.,<sup>(47)</sup>

and Long, et. al.<sup>(48)</sup> are available. All of these calculations predict for the particular orbit of present interest within our experimental range of temperature and magnetic fields, that the thermopower oscillation amplitudes should consist of one or more terms of the form:

$$A_{l,n} T^l H^n \exp[-2\pi^2 k_B (T + T_D) / \beta H] \quad (V.4)$$

where  $A_{l,n}$  is independent of  $H$  and  $T$ . Here  $l$  and  $n$  are constants  $2 \leq l \leq -1$  and  $3/2 \geq n \geq -3/2$ ; and  $\beta = \frac{e\hbar}{m^* c}$ .

In this section we will estimate the size of the quantum oscillations of  $S_d$  induced by the oscillatory component of the density of states, under a series of assumptions which are necessary to allow the estimation to be performed with data that currently exist in the literature. The assumptions are indicated at the points they are made. Only one of the assumptions, if incorrect, might be expected to have a dramatic effect on the estimate; the limits of this assumption are indicated in a footnote following the assumption.

From equations (III.20) and (III.24) we see that

$$S_d(H \rightarrow \infty) = \frac{2eL_O T}{(n_e - n_h)} \frac{d}{d\epsilon} [n_e(\epsilon) - n_h(\epsilon)] \Big|_{\epsilon=\epsilon_F} - \frac{\epsilon_{YY}}{\sigma_{YY}} \quad (V.5)$$

where

$$\epsilon_{YY} = eL_O T \frac{d}{d\epsilon} \sigma_{YY} \Big|_{\epsilon=\epsilon_F}.$$

If we assume that the electrical conductivity can be described by a two band Sondheimer-Wilson model<sup>(49)</sup> then

$$\sigma_{yy} = \frac{en_e H_e}{H^2 + H_e^2} + \frac{en_h H_h}{H^2 + H_h^2} \quad (V.6)$$

where

$$H_i^2 = \frac{m_i^* c}{e \tau_i}.$$

If we further assume that  $\frac{\partial H_i}{\partial \epsilon}$  (i.e.  $\frac{\partial \tau_i}{\partial \epsilon}$ ) gives a negligible contribution to the oscillatory component of  $\epsilon_{yy}^*$ ,  $\epsilon_{yy}^{osc}$ , then

$$\epsilon_{yy}^{osc} = -e^2 L_O T \left[ \frac{H_e}{H^2 + H_e^2} \left( \frac{\partial n_e}{\partial \epsilon} \right)^{osc} + \frac{H_h}{H^2 + H_h^2} \left( \frac{\partial n_h}{\partial \epsilon} \right)^{osc} \right] \Big|_{\epsilon = \epsilon_F}. \quad (V.7)$$

If we still further assume that  $H_e = H_h = H_O$  then

$$\epsilon_{yy}^{osc} = -e^2 L_O T \frac{H_O}{H^2} \left[ \left( \frac{\partial n_e}{\partial \epsilon} \right)^{osc} - \left( \frac{\partial n_h}{\partial \epsilon} \right)^{osc} \right] \Big|_{\epsilon = \epsilon_F} \quad (V.8)$$

and

---

\* Recent measurements by Thaler, et. al.<sup>(50)</sup> on a high purity (RRR = 7000) aluminum polycrystal revealed that under conditions where S displayed substantial quantum oscillations, the Nernst-Ettingshausen coefficient (i.e.  $\epsilon_{xy}$ ) revealed none. Since  $\epsilon_{xy}$  is not dependent on  $\partial \tau / \partial \epsilon$ , and  $\epsilon_{yy}$  is dependent on  $\partial \tau / \partial \epsilon$ , any significant oscillatory component in  $\partial \tau / \partial \epsilon$  would cause oscillations in S but not in the Nernst-Ettingshausen coefficient. Therefore, Thaler et. al.'s result suggests that the assumption that  $\partial \tau / \partial \epsilon$  contributes a negligible oscillatory component may not be completely valid.

$$\sigma_{YY} = \frac{eH_o}{H^2} (n_e + n_h) . \quad (V.9)$$

Dividing eq. (V.8) by eq. (V.9) gives

$$\frac{\epsilon_{YY}^{osc}}{\sigma_{YY}} = - \frac{eL_o T}{n_e + n_h} \left[ \left( \frac{\partial n_e}{\partial \epsilon} \right)^{osc} - \left( \frac{\partial n_h}{\partial \epsilon} \right)^{osc} \right]_{\epsilon=\epsilon_F} . \quad (V.10)$$

Measurements of the electrical resistivity of the single crystal aluminum and indium samples used in the experiments comprising this thesis show that for  $H \leq 20\text{kG.}$ ,  $\frac{\rho^{osc}}{\rho} < .01$ . From these measurements it may be inferred that  $n_e^{osc}$  and  $n_h^{osc}$  are negligible compared with  $n_e$  and  $n_h$  at all fields of interest. De Haas-van Alphen results show that both aluminum<sup>(32,51)</sup> and indium<sup>(52,53)</sup> have very small third zone electron-like orbits and much larger second zone hole-like orbits. This means that the third zone orbits will produce relatively low frequency ( $\sim 10^5 - 10^7\text{G.}$ ) oscillations compared to the higher frequency ( $\sim 10^8\text{G.}$ ) oscillations due to the second zone. From an experimental viewpoint, the highest frequency of oscillation which may be observed is limited by the homogeneity of the magnetic field over the entire length of the sample. In an inhomogeneous magnetic field, different portions of the sample will oscillate out of phase with other portions. This will wash out the oscillations in the thermal emf generated over the length of the sample. The highest



frequencies observed with present apparatus were about  $5 \times 10^6$  G. Therefore, only oscillations due to density of state variations of the third zone orbits can be observed. In view of this, the estimate of the quantum oscillations in  $S_d$  will be confined to these electron-like third zone orbits. We therefore write

$$\left(\frac{\epsilon_{yy}}{\sigma_{yy}}\right)^{osc} = - \frac{eL_o T}{n_e + n_h} \left(\frac{\partial n_e}{\partial \epsilon}\right)_{\epsilon=\epsilon_F}^{osc} . \quad (V.11)$$

In both aluminum and indium the volume of the second zone hole-like portion is much larger than the volume of the third zone electron-like portion. This means that

$$n_h + n_e \cong n_h \cong n_h - n_e = 1/\text{atom} , \quad (V.12)$$

and consequently

$$\left(\frac{\epsilon_{yy}}{\sigma_{yy}}\right)^{osc} = \frac{eL_o T}{n_e - n_h} \left(\frac{dn_e}{d\epsilon}\right)_{\epsilon=\epsilon_F}^{osc} . \quad (V.13)$$

Combining equations (V.5) and (V.13) gives

$$S_d^{osc}(H, T) = \frac{eL_o T}{n_e - n_h} \left(\frac{dn_e}{d\epsilon}\right)_{\epsilon=\epsilon_F}^{osc} , \quad \omega_C T \gg 1. \quad (V.14)$$

We now must evaluate the quantity  $\left(\frac{dn_e}{d\epsilon}\right)_{\epsilon=\epsilon_F}^{osc}$ . Within the framework of the Lifshitz-Kosevich<sup>(54)</sup> theory for a NFE gas, Gold<sup>(55)</sup> obtains an expression for  $n^{osc}$ . For the fundamental frequency his expression (in MKS

units) reduces to

$$n^{\text{osc}} = \frac{1}{2\pi^3 \hbar^3} (e\hbar H)^{3/2} \left( \frac{2\pi}{\left| \frac{d^2 A}{dk_H^2} \right|} \right)^{1/2} I_1 K_1 \sin\left(\frac{\hbar A}{eH} - 2\pi\gamma \mp \frac{\pi}{4}\right) \quad (\text{V.15})$$

where  $\gamma$  is an undetermined phase factor,

$\frac{\partial^2 A}{\partial k_H^2}$  is the curvature of the extremal cross-sectional area of the Fermi surface in the direction of  $H$ ,

$$I_1 = \frac{X}{\sinh X}, \quad k_B T \ll \hbar\omega_c,$$

$$X = \frac{2\pi^2 m^* k_B}{e\hbar H} T,$$

$$K_1 = \exp\left(-\frac{2\pi^2 m^* k_B}{e\hbar H} T_D\right),$$

$T_D$  is the Dingle Temperature. (56)

The  $I_1$  factor gives the temperature dependence of the amplitude of the oscillations in the carrier density. Since  $I_1$  decreases as  $T$  increases, the effect of a non-zero temperature is to decrease the oscillation amplitude. The oscillation amplitude will be further reduced if the electrons suffer collisions. This means that the electrons will possess a finite (not infinite) relaxation time. The  $K_1$  factor gives this correction because  $T_D$  is inversely proportional to the relaxation time.

Grenier, Zebouni, and Reynolds<sup>(47)</sup> claim that

the most important term in  $\left. \frac{\partial n^{\text{osc}}}{\partial \epsilon} \right|_{\epsilon=\epsilon_F}$  arises from the derivative of the phase (recall that  $A = A(\epsilon)$ ). This

assumption gives

$$\left. \frac{\partial n^{\text{osc}}}{\partial \epsilon} \right|_{\epsilon=\epsilon_F} = \frac{m^*}{\pi \hbar^2} (\epsilon \hbar H)^{1/2} \left( \frac{2}{\left| \frac{\partial^2 A}{\partial k_H^2} \right|} \right)^{1/2} I_1 K_1 \cos\left(\frac{\hbar A}{eH} - 2\pi\gamma + \frac{\pi}{4}\right) \quad (\text{V.16})$$

In an effort to estimate an upper bound for  $S_d^{\text{osc}}$ , the effect of a finite relaxation time will be neglected, i.e. set  $K_1 = 1$ . The calculation will be performed for  $H$  aligned along the  $[010]$  axis in both aluminum and indium. For the  $\beta$ -orbit in aluminum the values:

$$m^* = 0.095 m_e \quad (32)$$

$$\left| \frac{\partial^2 A}{\partial k_H^2} \right| = 7 \quad (57)$$

$$(n_e - n_h)^{-1} = -1.63 \times 10^{-29} \text{ m}^3$$

$$H = 15.0 \text{ kG.}$$

$$T = 1.72 \text{ K}$$

give an oscillation amplitude.

$$S_d^{\text{osc}}(\text{Al}) = 0.28 \times 10^{-11} \text{ V/K.} \quad (\text{V.17})$$

For the neck orbit of the  $\beta$ -arms in indium the values:

$$m^* = 0.2 m_e \quad (58)$$

$$\left| \frac{\partial^2 A}{\partial k_H^2} \right| = 0.5 \quad (57)$$

$$(n_e - n_h)^{-1} = -2.56 \times 10^{-29} \text{ m}^3$$

$H = 15.5\text{kG}.$

$T = 1.67\text{K}$

give an oscillation amplitude

$$S_d^{\text{osc}}(\text{In}) = 1.0 \times 10^{-11} \text{V/K} . \quad (\text{V.18})$$

It is hoped that eqs. (V.17) and (V.18) give order of magnitude estimates of the amplitude of magnetothermopower oscillations arising from oscillations in the density of states at  $\epsilon_F$  of aluminum and indium. These estimates suggest that such  $S_d$  oscillations should be roughly the size of the signal noise in our measurements and much smaller than the non-oscillatory component of  $S$ .

### C. Magnetic Breakdown

Up until now we have assumed that the electrons can make transitions only between states within the same band, i.e. we have ignored interband transitions. However, in large magnetic fields electrons can tunnel between bands, giving rise to the phenomenon of magnetic breakdown. When this happens, the semi-classical quantization scheme described in section V.A breaks down. The review article by Stark and Falicov<sup>(60)</sup> gives a more comprehensive study of this phenomenon than will be presented here.

To understand magnetic breakdown we will first consider a free electron gas in a magnetic field.

Neglecting interactions among the electrons, the electron wavefunctions are those of a particle in a circular orbit in the  $(k_x, k_y)$  plane, which is normal to  $\vec{H}$ . We then introduce a lattice perturbation of the form  $V(x) = \sum_G V_G e^{iGx}$ . When an orbit passes through a zone boundary (i.e. its wavevector in the x direction,  $k_x$ , is equal to  $\pm 1/2 G$ ), there is the possibility of Bragg reflection. Using Figure V.2(a) as an example, this means that instead of continuing along AB, the orbit may switch to the direction AC, and so on.

If the strength of the perturbation is increased, then the trajectories at A will be split apart in energy, and the route AC will be favored. The electron is now moving on an ordinary (open) orbit in the repeated zone scheme. This is shown in Figure V.2(b). The part B of the circle in Figure V.2(a) has now been joined up into a separate branch of the Fermi surface, and is traversed separately.

As the magnetic field is increased, the effect of the lattice perturbation will decrease, so the circular orbit will become more and more favored. Instead of the electron going along AC, it may break through the energy gap, ("tunnel through" the region separating the two orbits in k-space) and wind up going around orbit B.

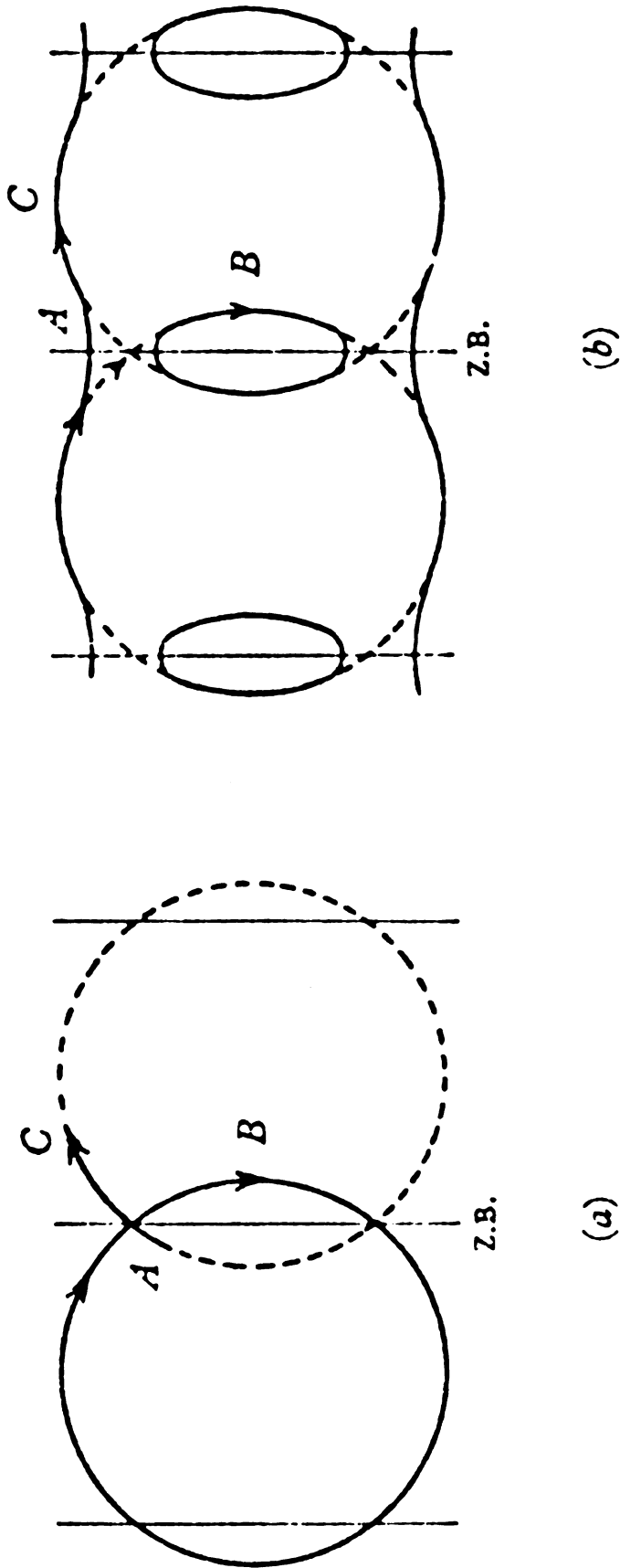


Figure V.2: (a) Free electron orbit in a magnetic field; (b) In the periodic potential of the lattice, the orbits are reconnected at the zone boundary, but in a strong magnetic field the orbit may jump back to the free electron path (after Ziman (61)).

In practice such behavior occurs at portions of the Fermi surface where the band splittings are very small ( $10^{-2}$  -  $10^{-3}$  eV.). This usually happens at symmetry points of the Brillouin zone. The best known cases correspond to splittings due to spin-orbit coupling.

The description of magnetic breakdown as illustrated by Figure V.2(b) can be extended to real metals like aluminum and indium. Figure V.3 shows the

third zone pieces of the Fermi surface of aluminum and Figure V.4 shows a central (001) section of this Fermi surface. With a magnetic field along the [001] axis, electrons travel clockwise on orbits like FABH... (of Figure V.4), thus they are hole-like. In the absence of magnetic breakdown, a hole arriving at B from A will continue to H; otherwise it could break through the energy gap and "jump" on to the small electron-like  $\beta$ -orbit and proceed to C. Here it may "jump" to the hole-like orbit and proceed to D, or remain on the  $\beta$ -orbit and continue to B, then to H or C, etc. The net result of this, ignoring complications due to the possibility of scattering while on the  $\beta$ -orbit, is that either the hole remains on its original (second zone) trajectory, or it moves across the zone boundary on to another second zone trajectory and moves in the opposite direction. When the breakdown probability is large, the hole is "reflected" near the corner W' and thus travels

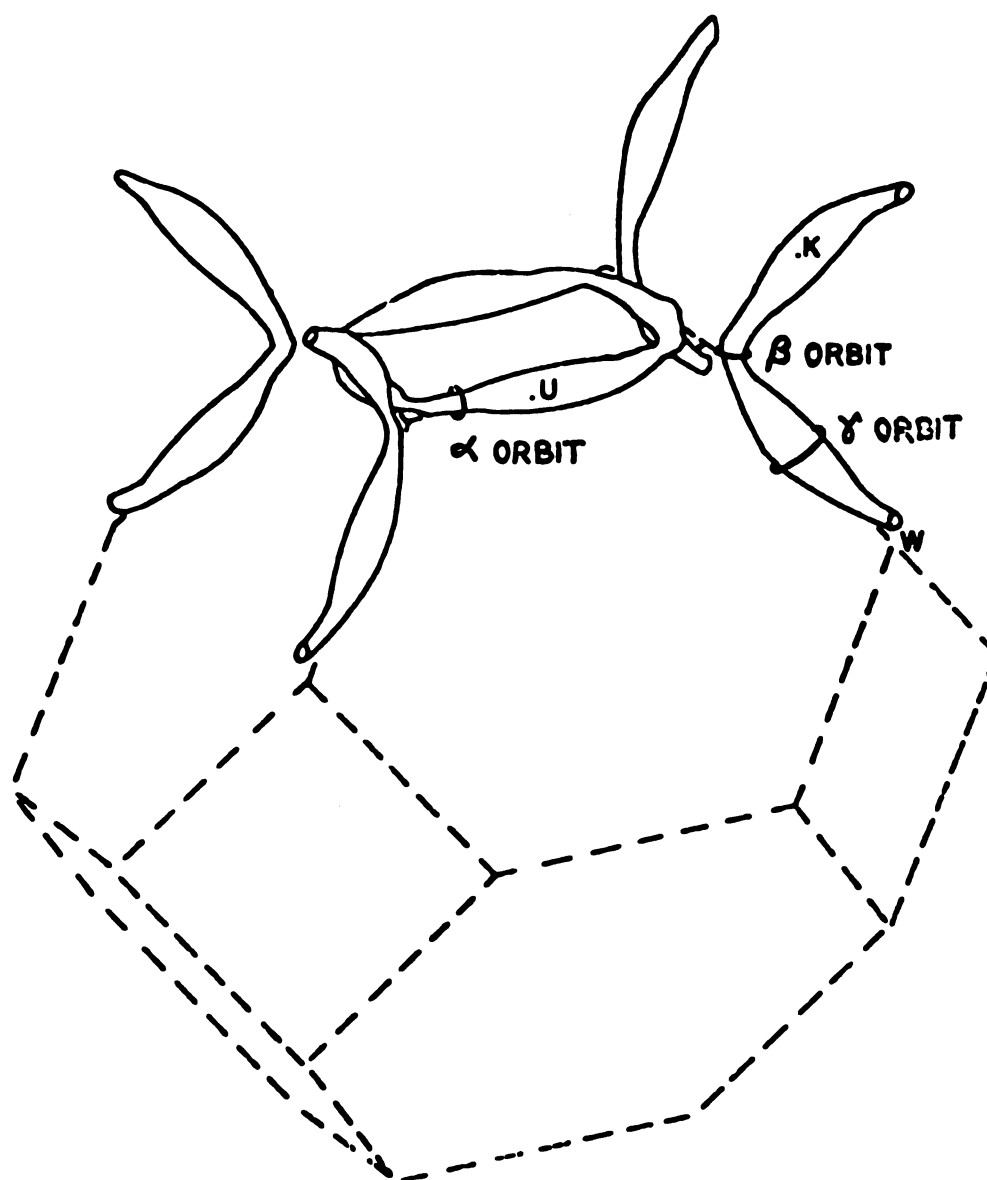
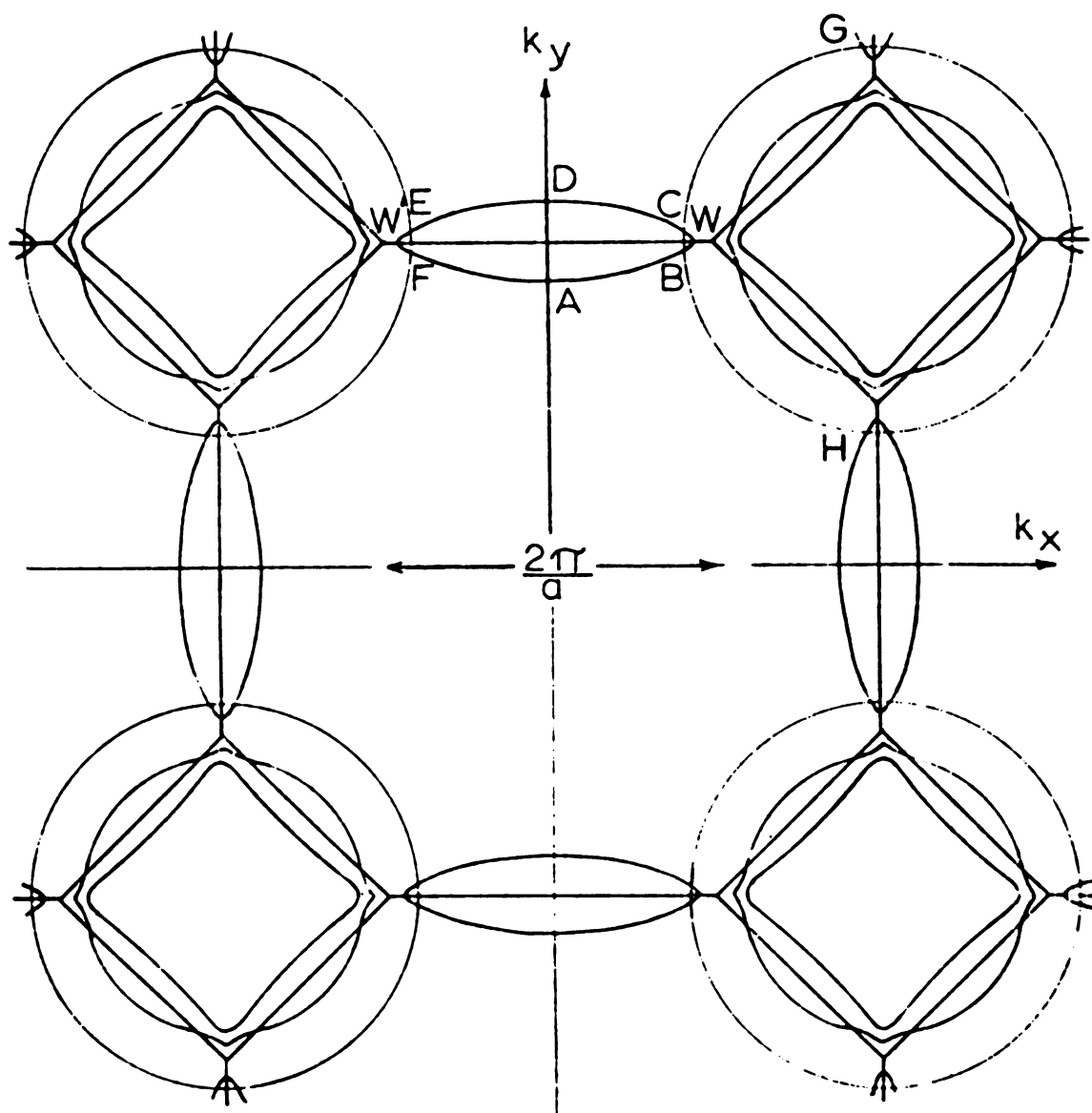


Figure V.3: Ashcroft's 4-OPW pseudopotential model for the electron-like 3rd zone of the Fermi surface of aluminum (after Abele and Blatt(62)).





**Figure V.4:** Central [100] section through the aluminum Fermi surface (after Ashcroft(63)).

over the lens shaped, electron-like orbit. Similarly a hole arriving at C from G will move to either D or B; if it reaches B, it then goes toward H or returns to C. When the breakdown probability is large the resultant orbit GCBH... is circular and electron-like.

Pippard<sup>(64)</sup> has derived an expression for the breakdown probability for a junction between orbits of the same topology as in Figure V.4. If R is the probability of a particle proceeding along CDE after arriving at B from A, or proceeding along BH after arriving at C from G, then

$$R = \frac{P^2}{1 - 2\cos\theta + Q^2} \quad (V.19)$$

where  $P = \exp(-H_0/H)$ ,  $H_0 = \epsilon_g m^* c / \epsilon_F \hbar e$ ,  $\epsilon_g$  being the energy gap between the bands at the point in k-space where the break through occurs,  $Q = 1-P$ , and  $\theta$  is defined as

$$\theta = \theta_0 + \frac{c\hbar A}{eH} \quad (V.20)$$

where  $\theta_0$  is a constant and A is the area (in k-space) through which breakdown occurs (the  $\beta$ -orbit in our case). Thus, the breakdown probability has an oscillatory component with a period (in  $1/H$ ) of  $2\pi e / c\hbar A$ . This is the same period as would be found in the ordinary (i.e. in absence of magnetic breakdown) de Haas-van Alphen oscillations associated with the small connecting orbit.

As the breakdown probability becomes alternately stronger and weaker with increasing field, the orbits of the central (001) section of the Fermi surface become alternately more and less electron-like and both the equilibrium and transport properties of the metal fluctuate accordingly.

So far we have only described a simple microscopic picture of magnetic breakdown, and have not considered the effect of this phenomenon on the macroscopic properties of the material. The equilibrium properties (e.g. de Haas-van Alphen effect) are the easiest to treat, so we will consider them first. Once the electron system's free energy is known as a function of  $H$ , all the equilibrium properties may be calculated from it via the appropriate thermodynamic relations. To calculate the free energy requires a knowledge of the magnetic field dependent density of states  $\rho(\epsilon, \vec{H})$ . Falicov and Stachowiak<sup>(65)</sup> have proposed a Green's function method for calculating the oscillatory part of  $\rho(\epsilon, H)$ . The Green's function has been exactly calculated for the free electron case, and it is believed to provide an accurate description of the NFE case (after making the appropriate changes<sup>(60)</sup>). The important result of this procedure is that oscillations, periodic in  $1/H$ , will occur in the equilibrium properties. These oscillations will have a frequency corresponding to the area of the breakdown

orbits; this frequency will be the same as that observed in the ordinary de Haas-van Alphen type oscillations. However, when the breakdown nears completion new frequencies will appear; these frequencies reflect the new and larger orbits formed by breakdown (similar to the free electron circle shown in Figure V.3(a)). Such giant orbits have been seen in a number of metals, e.g. magnesium.<sup>(66)</sup>

Currently the description of transport phenomena in the presence of magnetic breakdown is far from complete. The effects on electrical conductivity have been considered by a number of authors, some being Pippard,<sup>(67)</sup> Young,<sup>(68)</sup> and Stark and Falicov.<sup>(60)</sup> They all agree that magnetic breakdown will cause oscillations, periodic in  $1/H$ , which will have the same frequencies as those in the equilibrium properties. Stark and Falicov have performed a calculation for an idealized case, which indicates that the oscillation amplitude can be comparable to the non-oscillatory component of the transverse magnetoresistance.<sup>(60)</sup>

At the present time very little work has been done on the effects of magnetic breakdown on magnetothermopower. Young<sup>(69)</sup> has considered this problem for a different junction topology than that found in aluminum and indium. He obtains an oscillatory component of the magnetothermopower, which again exhibits the same

frequencies as those of the equilibrium properties. We might note in passing, that if parameters appropriate to the particular orbits of present interest are substituted into Young's expression, then within the experimental range of temperatures and magnetic fields, this expression may be approximated by one or more terms of the form of eq. (V.4). Young also notes that for an "opening" network (similar to the junction topology of aluminum and indium) no actual calculations have been made, because a simple expression does not arise. However, there should be an oscillatory component.

The present state of theory of the effect of magnetic breakdown on magnetothermopower oscillations is not far enough advanced to allow calculation of the amplitude of these oscillations. However, independent experimental evidence obtained prior to this thesis indicates that magnetic breakdown is present in all metals that have exhibited giant magnetothermopower oscillations\* (this will be discussed in more detail in section VI.C.1). These giant oscillations have frequencies that correspond to the small connecting orbits which facilitate the magnetic breakdown.

---

\* The fact that the oscillatory component is comparable to, or much larger than the non-oscillatory component engenders the designation "giant oscillations".

## VI. OSCILLATORY THERMOELECTRIC PHENOMENA - EXPERIMENT

### A. The Fermi Surfaces of Aluminum and Indium

The Fermi surfaces of aluminum and indium have been extensively studied; and consequently the Fermi surface dimensions are known in detail. The Fermi surfaces of both these metals consist of a large second zone hole surface and a small third zone surface which is made of "arms" of electrons. Figure VI.1 shows the Fermi surface of indium. The second zone hole surface (Figure VI.1(b)) is very adequately represented by the free-electron model, and is quite similar for both aluminum and indium. The third zone electron surface of indium shown in Figure VI.1(c), consists only of  $\beta$ -arms, and these  $\beta$  arms are joined together in four-sided rings in the (001) (but not the (100) plane) by small junctions near point T.<sup>(59)</sup> The third zone surface of aluminum is similar to that of indium, but with a few significant differences:

1. The third zone of aluminum consists of both  $\alpha$  and  $\beta$  arms (see Figure V.3).
2. The third zone of aluminum consists of four sided rings of "arms" in both the (001) and (100) planes (a consequence of cubic symmetry).

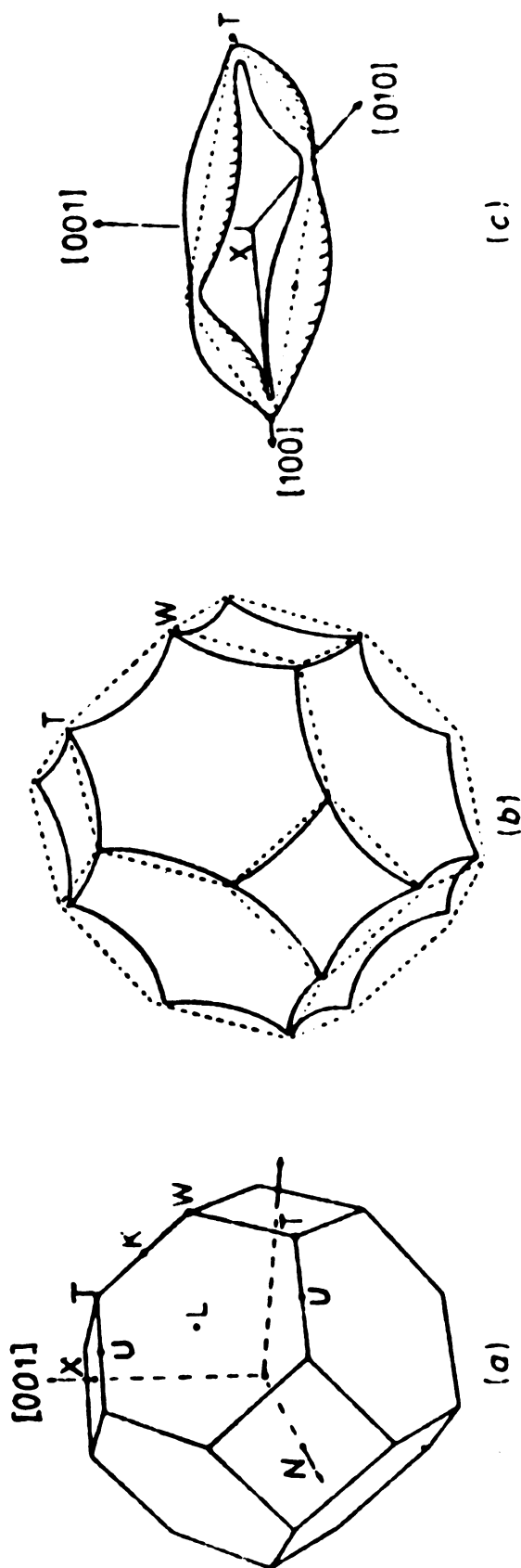


Figure VI.1: (a) The Brillouin zone for face-centered tetragonal indium; (b) the indium free-electron model hole surface; (c) the indium third zone electron  $\beta$ -arm surface (after Hughes and Shepherd(52)).

3. In aluminum there is a swelling at the junction where the  $\beta$ -arms connect; in indium this swelling is either small<sup>(52)</sup> or completely absent.<sup>(59)</sup> This is a consequence of the much stronger spin-orbit interaction present in indium.

The free electron model predicts that the second and third zones would be degenerate at certain high symmetry points of the Brillouin zone. However, a non-zero spin-orbit interaction breaks this degeneracy, thereby closing both surfaces (i.e. there are no open orbits). The oscillations observed in this thesis have frequencies which are associated with the third zone  $\beta$  and  $\gamma$ -orbits in aluminum, and the neck and belly orbits of the  $\beta$  "arm" in indium.

## B. Aluminum

### 1. Introduction

Since the spin-orbit interaction is quite small in aluminum, the second and third zones are almost but not quite degenerate at certain points in the Brillouin zone. Therefore, aluminum has a Fermi surface which is favorable to magnetic breakdown. Balcombe and Parker<sup>(34)</sup> have observed oscillations in the magnetoresistance of aluminum for H along the [010] axis. These oscillations had the same frequency as the electron-like  $\beta$  orbits. Using a simple magnetic breakdown model, which allowed



holes (second zone) to "jump" from one orbit to another in an adjacent Brillouin zone using a third zone electron-like  $\beta$ -orbit as a bridge (see section V.C), their calculated values for  $\rho_{xx}$  and  $\rho_{xy}$  agreed "tolerably well with the experimental results".

Recently, Bozhko and Vol'skii<sup>(70)</sup> have observed oscillations in the magnetoresistance of aluminum for H along the [110] axis, when the temperature was below 1K. They also attributed these oscillations to magnetic breakdown.

Concurrent with the research constituting this thesis, two other research groups: Kesternich and Papastaikoudis,<sup>(29)</sup> and Sirota, et. al.,<sup>(34)</sup> independently discovered the existence of giant quantum oscillations in the magnetothermopower of aluminum for H along the [010] direction. The oscillation frequency was the same as that observed by Balcombe and Parker.<sup>(34)</sup> Both of these groups attributed these giant oscillations to magnetic breakdown. Additionally, Kesternich and Papastaikoudis noted that the amplitude of the thermopower oscillations exhibited a simple exponential decay in  $1/H$  over the entire field range ( $H < 48\text{kG}$ ).

Both of the aforementioned groups constrained their thermopower measurements to having the cold end of the sample remaining at about 4.2K, while producing temperature differences along the sample of about 1K.

The great sensitivity of the chopper-amplifier system allowed the measurements of this thesis to be performed using relatively small temperature differences (typically 0.1 - 0.2K). Therefore, the temperature variation of the oscillations could be studied. The thermopower measurements were extended down to 1.7K.

## 2. Experimental Procedure

All measurements were performed on the Al(Ga) sample (see Table I-1). The measurements were performed using the chopper-amplifier in the field sweep mode (described in sections II.A.2 and II.F). This procedure provided a continuous record of the thermopower as a function of the magnitude of the magnetic field, while the sample temperature remained essentially fixed.

## 3. Data and Analysis

### 3.1. H parallel to {010}

Figure VI.2 displays an example of the raw data; it shows the relative magnitudes of the oscillatory and non-oscillatory (broken line) components, and indicates the precision of the data. In this figure the solid line labeled  $S = 0$  represents the recorder output when there is no temperature gradient along the sample; the oscillating curve is uncorrected for the field dependent amplification of the voltage measuring system and also for the slight increase in  $\Delta T$  along the sample as  $H$  is

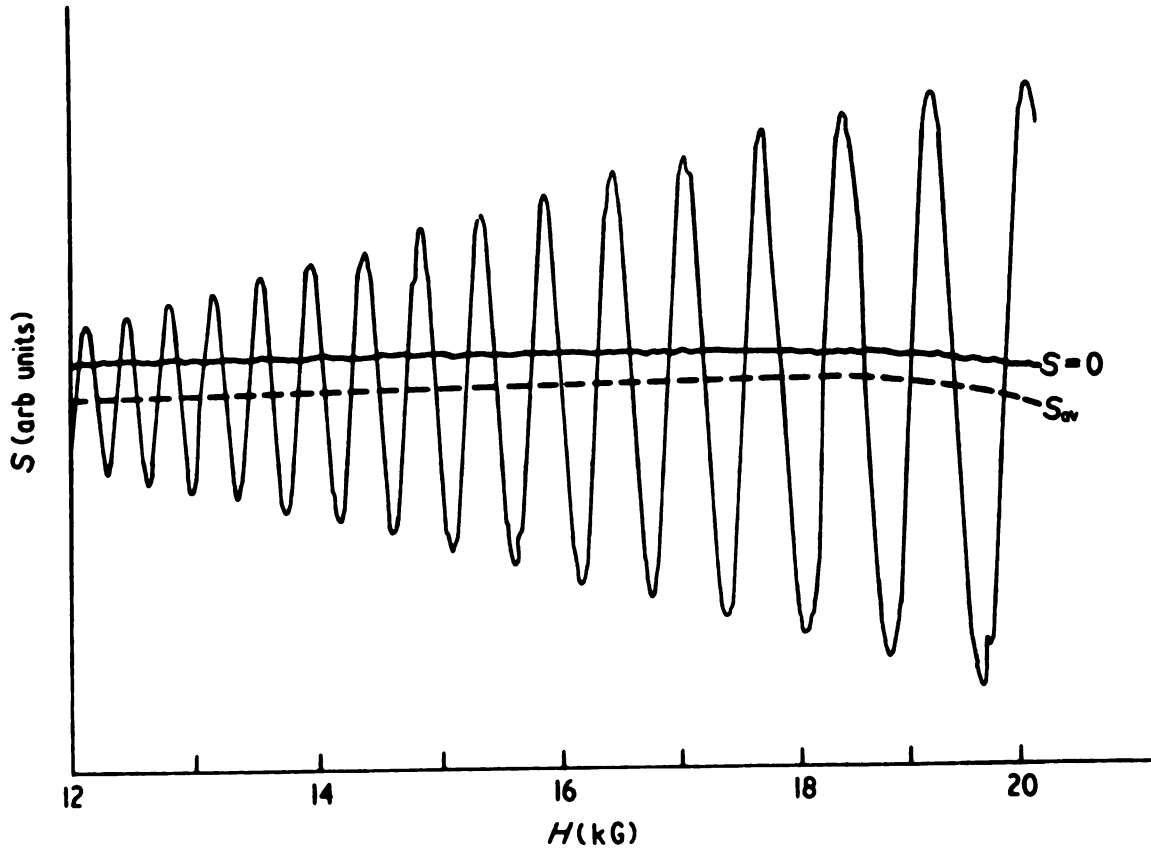


**Figure VI.2:** The variation of  $S$  with magnetic field at  $T = 3.55\text{K}$  for the  $\text{Al}(\text{Ga})$  sample.  $H$  is along the  $[010]$  axis. The solid line labeled  $S = 0$  represents the x-y recorder output when there is no applied temperature gradient. The broken line indicates the non-oscillatory component of  $S$ . The oscillating curve represents raw data, uncorrected for a field dependent amplification of the measuring system. The magnitude of this correction is indicated by the manner in which the  $S = 0$  curve and the broken line approach each other as  $H$  increases. When the data are corrected, these two curves are equidistant at all fields above about 11kG to within experimental uncertainty.

increased. One can get a feeling for the size of the corrections by noting that after correction, the  $S = 0$  curve and the broken line remained equidistant at all fields above 11kG to within experimental accuracy. The oscillations in Figure IV.2 are described by a single frequency, characteristic of the third zone  $\beta$ -orbit of aluminum. This is consistent with all previous measurements of oscillatory transport properties. (29,30,34) The oscillation pattern was insensitive to small misalignments ( $\sim 1^\circ$ ) of H relative to [010].

In section V.B the amplitude of oscillation in S due to variation of the density of states at the Fermi energy was estimated, and it was concluded that these oscillations should be smaller than the signal noise inherent in the voltage measuring system. The variation in the  $S = 0$  curve in Figure VI.2 gives a measure of this noise. It is quite clear from this figure that the oscillation amplitude estimate of section V.B is much too small to explain the data. In fact at 15.0kG, the experimental oscillation amplitude was more the four orders of magnitude larger than the estimate given by eq. (V.17).<sup>\*</sup> However, previous oscillatory magnetoresistance data<sup>(34)</sup> suggest that magnetic breakdown is

---

<sup>\*</sup> For comparison with experiment the value of  $S_d^{osc}$  (Al) given in eq. (V.17) must be multiplied by four, because there are four independent  $\beta$  orbits which contribute to S.

present in this direction in aluminum. If we assume that breakdown is also the cause of the magnetothermopower oscillations then we should expect a discrepancy between the calculation of section V.B and experiment; and indeed the discrepancy is large.

In section V.A it was noted that all calculations predict for the orbit of interest within the experimental range of temperatures and magnetic fields, that the thermopower oscillation amplitudes should consist of one or more terms of the form of eq. (V.4). If only one term is present or dominant, then the data can be directly analyzed in terms of eq. (V.4). According to this expression, if  $\ln(SH^{-n})$  is plotted against  $1/H$  for a series of fixed temperatures, straight lines with slopes  $2\pi^2 k_B (T + T_D)/\beta$  should result. Figures VI.3 - VI.5 show such plots for  $n = -3/2, 0, +3/2$  respectively. The best straight lines are for  $n = 0$  and  $n = -3/2$ . Continuing in the spirit of eq. (V.4), plotting these slopes against  $T$  should also yield a straight line with slope  $2\pi^2 k_B m^* c / e \hbar$  and intercept at  $T = 0K, 2\pi^2 k_B T_D m^* c / e \hbar$ . Thus, from knowledge of the slope and intercept both  $m^*$  and  $T_D$  can be experimentally derived. Figure VI.6 shows such a plot for  $n = 0$ ; similar plots are obtained for  $n = \pm 3/2$ . Table VI-1 contains the values obtained for  $m^*$  and  $T_D$  for two perpendicular (but crystallographically equivalent) directions of  $H$ .

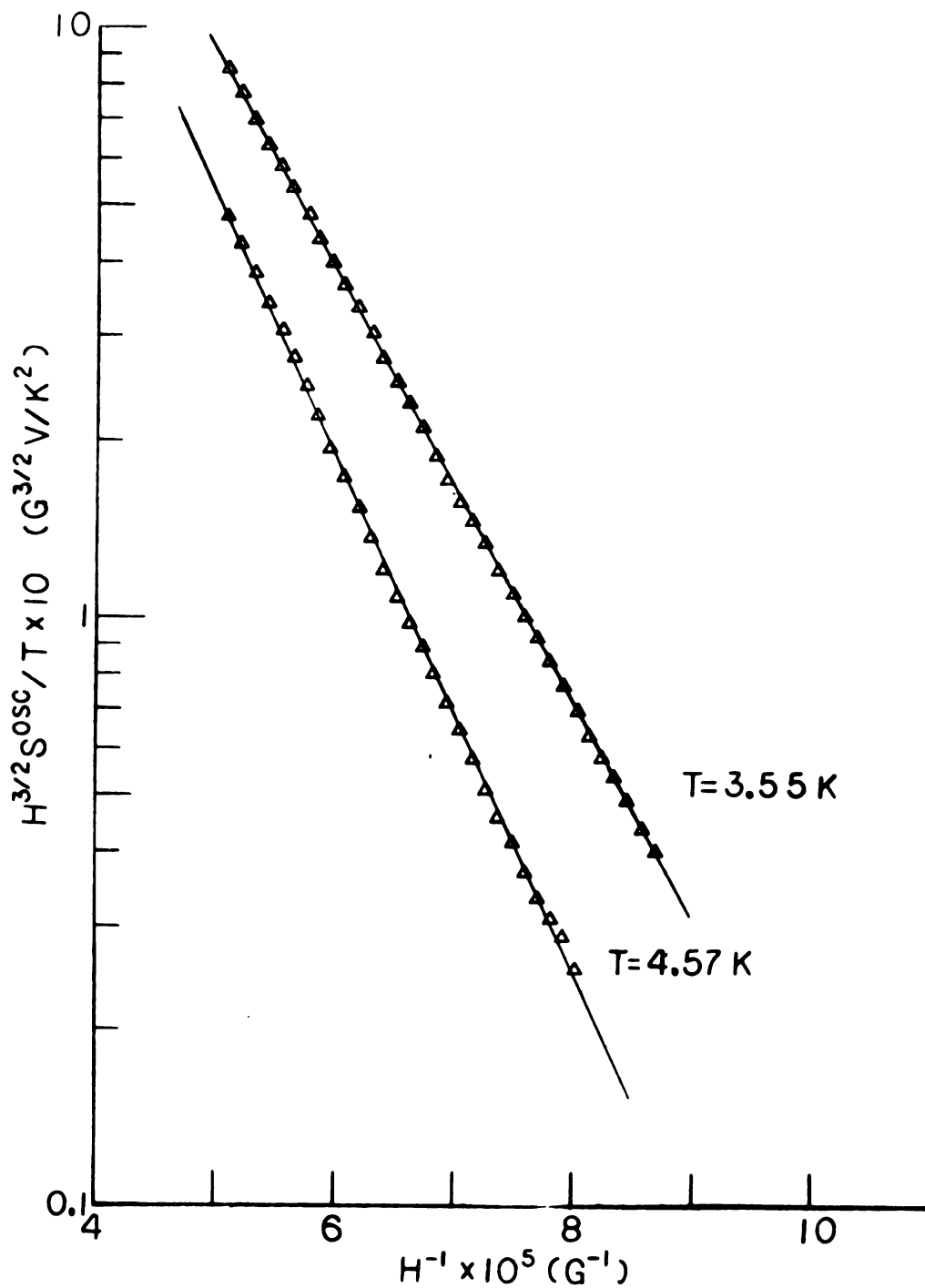


**Figure VI.3:** The variation of the quantity  $H^{3/2} S^{osc} / T$  (plotted on a logarithmic scale) with  $H^{-1}$  for a series of temperatures for sample Al(Ga).  $H$  was directed along [010].

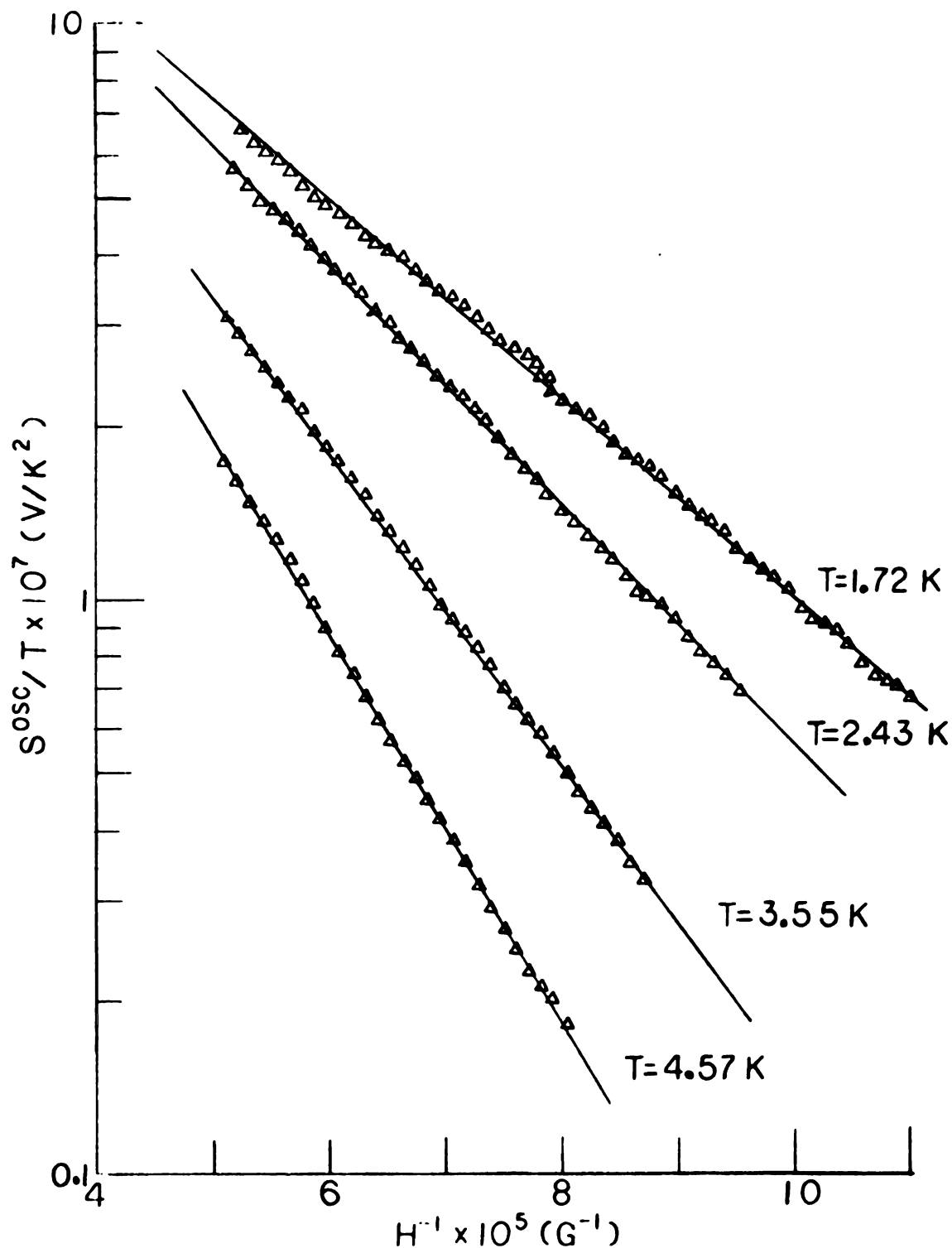


Figure VI.4: The variation of the quantity  $S^{\text{osc}}/T$  (plotted on a logarithmic scale) with  $H^{-1}$  for a series of temperatures for sample Al(Ga).  $H$  was directed along [010].

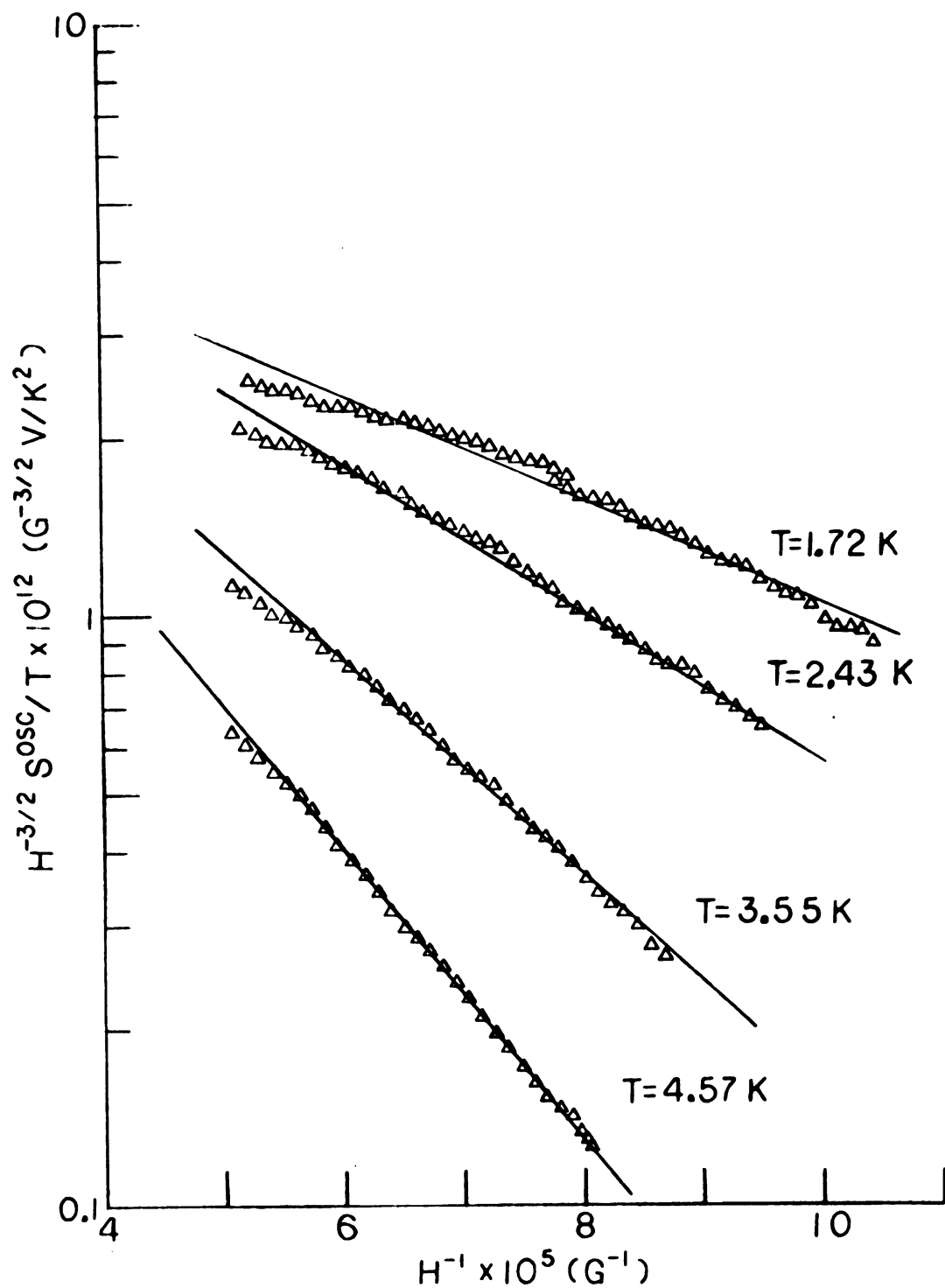


Figure VI.5: The variation of the quantity  $H^{-3/2} S^{osc}/T$  (plotted on a logarithmic scale) with  $H^{-1}$  for a series of temperatures for sample Al(Ga).  $H$  was directed along [010].



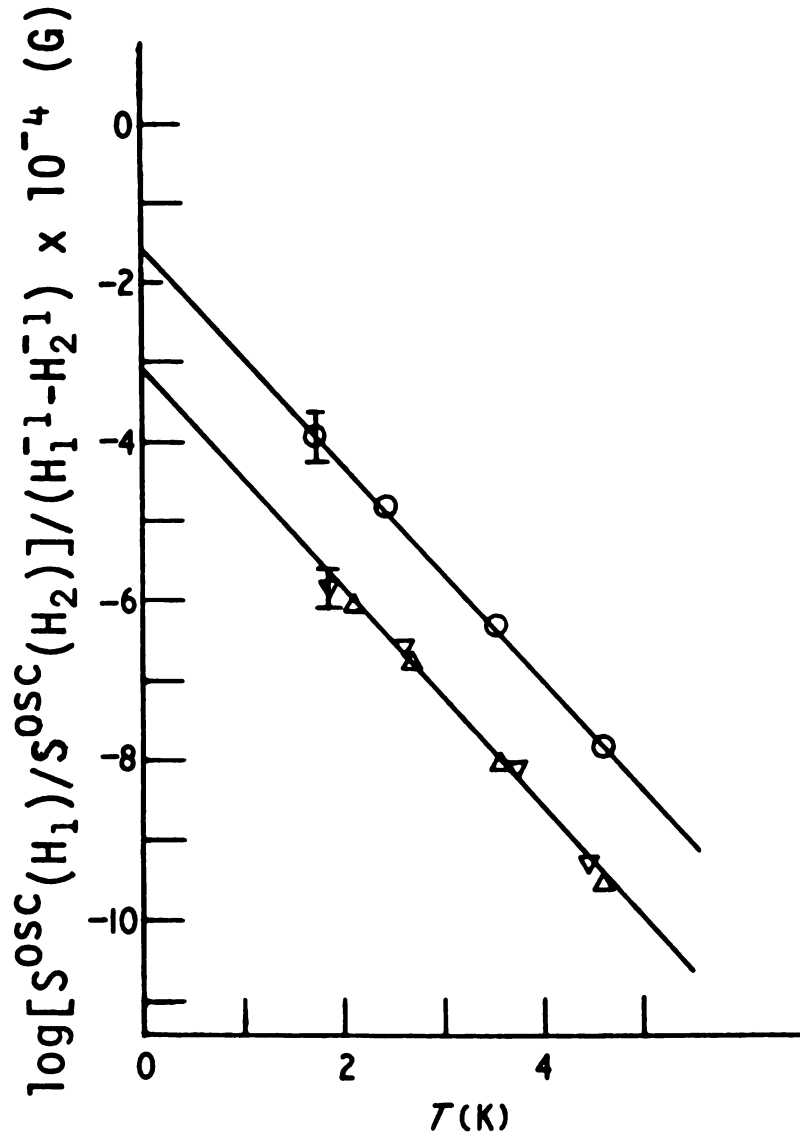


Figure VI.6: The variation with temperature of the slopes of the lines shown in Figure VI.4 for H parallel to [010] (circles) and of similar slopes of similar lines for H parallel to [100] (triangles). The upright triangles represent initial measurements with H parallel to [100]. To evaluate the effects of changes in sample treatment and alignment, after these initial measurements were completed the sample was removed from the holder, its potential leads were removed, it was reannealed, the potential leads were reattached and the sample was returned to the holder. The resulting data are indicated by inverted triangles.

Table VI-1: Values of  $m^*/m_e$  and  $T_D$  for two orthogonal directions of the magnetic field H and for different assumed values of n for Al(Ga)

	n	$m^*/m_e$	$T_D$ (K)
H parallel to [010]	-3/2	$0.096 \pm 0.01$	$2.5 \pm 0.6$
	0	$0.093 \pm 0.01$	$1.1 \pm 0.6$
	+3/2	$0.086 \pm 0.02$	$\sim 0 \pm 0.6$
H parallel to [100]	-3/2	$0.093 \pm 0.01$	$4.2 \pm 0.6$
	0	$0.092 \pm 0.01$	$2.4 \pm 0.6$
	+3/2	$0.095 \pm 0.01$	$0.7 \pm 0.6$

We see that the values of  $m^*$  are the same to within the specified uncertainties for both directions of H and for all values of n in the predicted range, whereas the values of  $T_D$  are not in agreement. This demonstrates that  $T_D$  can only be determined for an assumed value of n, but reliable values of  $m^*$  may be determined without such an assumption. Additional studies showed that  $m^*$  did not change significantly when the magnetic field was reversed or when the sample was removed from the holder, re-annealed and returned.

From Table IV-1 it is concluded that  $m^* = (0.93 \pm .01)m_e$ . The only other measurements of  $m^*$  for the  $\beta$ -orbit of aluminum are de Haas-van Alphen measurements.<sup>(32)</sup> These give  $m^* = (0.102 \pm .006)m_e$ , in agreement to within the specified uncertainties with the value

derived from thermopower measurements. We might note in passing that theory predicts the  $m^*$  derived from de Haas-van Alphen data to be phonon-enhanced by about 50% over the bare band mass.<sup>(71,72)</sup> Therefore, the  $m^*$  derived from thermopower measurements is similarly enhanced.

Finally, the thermopower data shows  $1 \leq \nu \leq 2$ , again in accordance with available predictions.

### 3.2. H along other directions in the (001) plane

Magnetic breakdown in aluminum is expected to be greatest for H directed along [010]. In this section data will be presented for H in directions other than [010].

As previously noted, the S oscillation pattern was insensitive to small rotations ( $\sim 1^\circ$ ) of H from [010]. However, the oscillation amplitude did decrease as H was rotated away from [010]. Figure VI.7 shows that the oscillation amplitude has been reduced to about the size of the non-oscillatory component (at  $T = 2.4\text{K}$ ,  $H \sim 17\text{kG}$ ) when H is rotated  $20^\circ$  from [010] axis in the (001) plane. Figure VI.8 shows that the oscillation amplitude has become much smaller than the non-oscillatory component of S when H is directed along [110]. Thus, it may be concluded that although magnetic breakdown via the  $\beta$ -orbit exists for H aligned along any direction in (001), the probability of magnetic breakdown decreases as H is rotated away from [010] (i.e. the energy gap between the

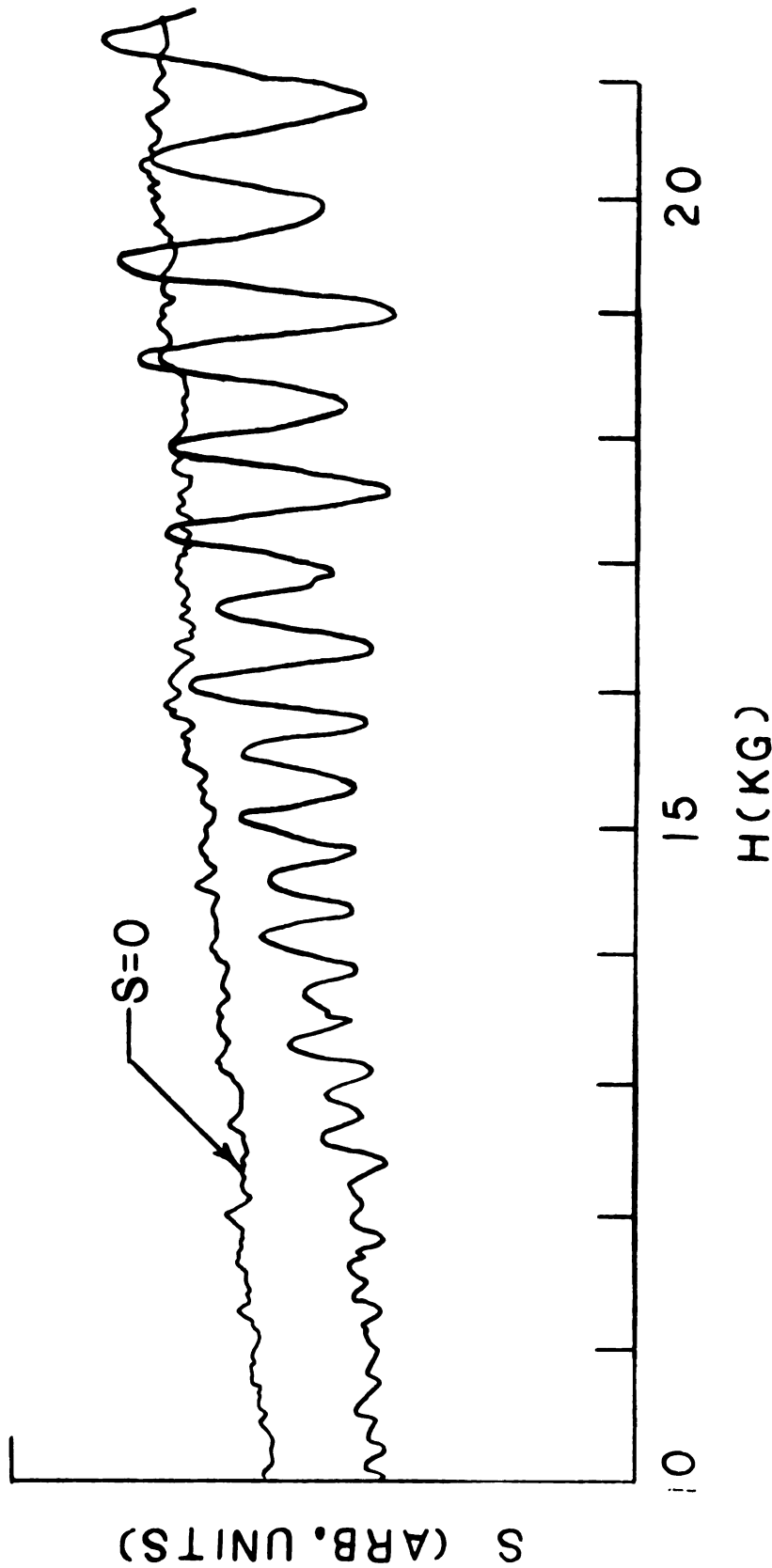


Figure VI.7: The variation of  $S$  with magnetic field at  $T = 2.4\text{K}$  for the  $\text{Al(Ga)}$  sample.  $H$  is rotated  $20^\circ$  from the  $[010]$  axis in the  $(001)$  plane. The solid line labeled  $S = 0$  represents the x-y recorder output when there is no applied temperature gradient. The oscillatory curve represents raw data, uncorrected for the field dependent amplification of the measuring system.

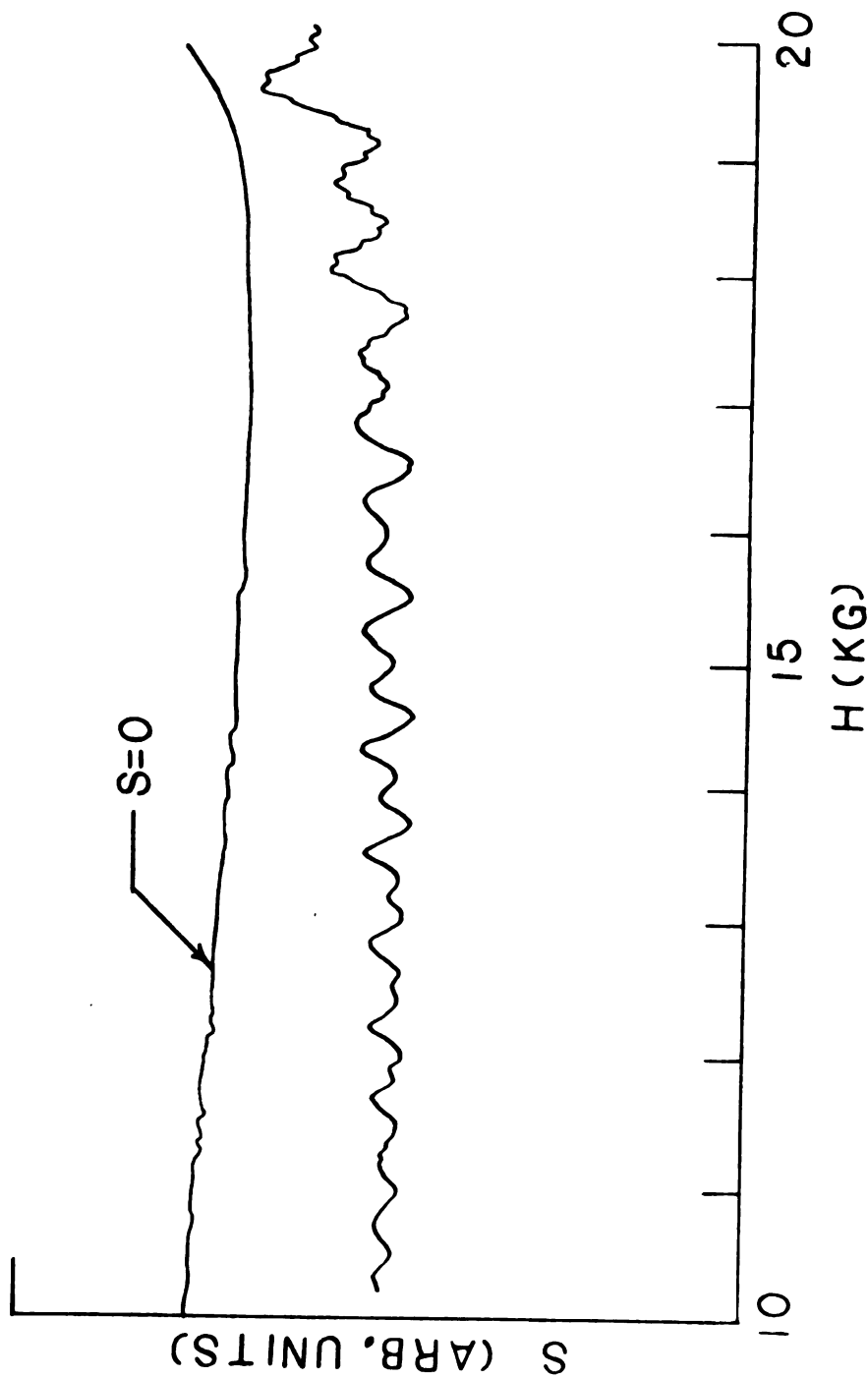
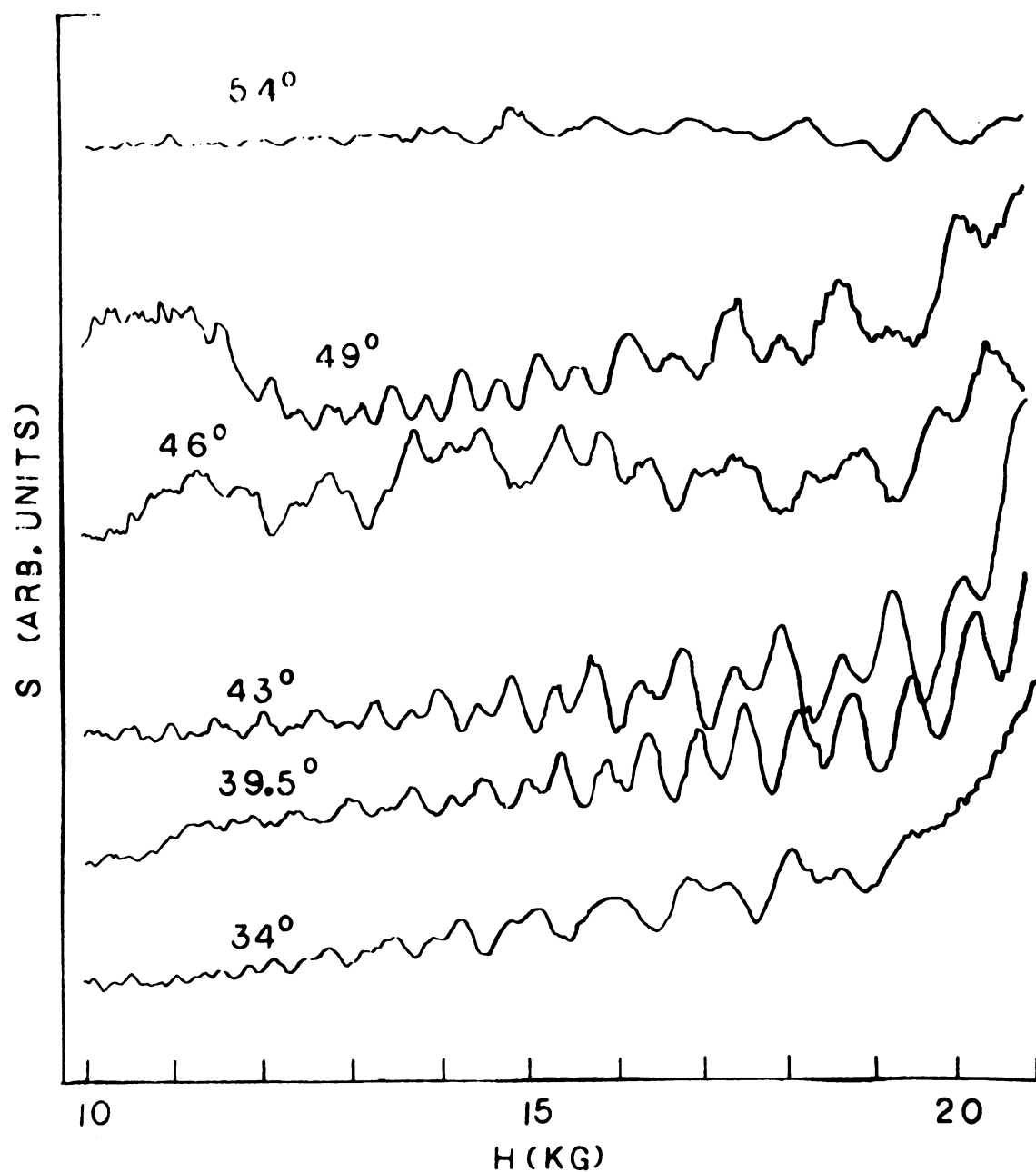


Figure VI.8: The variation of  $S$  with magnetic field at  $T = 2.8\text{K}$  for the  $\text{Al(Ga)}$  sample.  $H$  is along the  $[110]$  axis. The solid line labeled  $S = 0$  represents the x-y recorder output when there is no applied temperature gradient. The oscillating curve represents raw data, uncorrected for the field dependent amplification of the measuring system.

second and third Brillouin zones increases as  $H$  is rotated away from  $[010]$ ).

For a particular orbit, a magnetic field directed in an arbitrary direction in the  $(010)$  plane will in general intersect different extremal cross-sectional areas (normal to  $H$ ) on the individual third zone "arms" which form the ring of arms. Since the cross-sectional area determines the oscillation frequency, the general oscillation pattern due to a particular orbit will be composed of oscillations of several frequencies. Also the oscillation amplitude is expected to be frequency dependent. Thus, the oscillation pattern for the magnetic field in an arbitrary direction may be quite complicated, as shown in Figure VI.9. Only for  $H$  along either  $[010]$  or  $[110]$  will the frequencies of all  $\beta$ -orbits be equal, so that the oscillation pattern may be described by a single frequency.

Figure VI.10 shows frequencies of the major low frequency oscillations obtained from S data. Also shown in Figure VI.10 are the frequencies obtained from de Haas-van Alphen measurements<sup>(32)</sup> and Ashcroft's predicted frequencies for the  $\beta$ -orbits based on a pseudopotential calculation<sup>(63)</sup> which was fit to de Haas-van Alphen data. This figure shows that the frequencies for a particular orbit obtained from either de Haas-van Alphen or magnetothermopower oscillation measurements agree to within their



**Figure VI.9:** The variation of  $S$  with magnetic field at  $T = 2.3\text{K}$  for  $H$  along a series of directions in the (001) plane of the  $\text{Al(Ga)}$  sample.  $0^\circ$  corresponds to  $H$  directed along  $[100]$ .

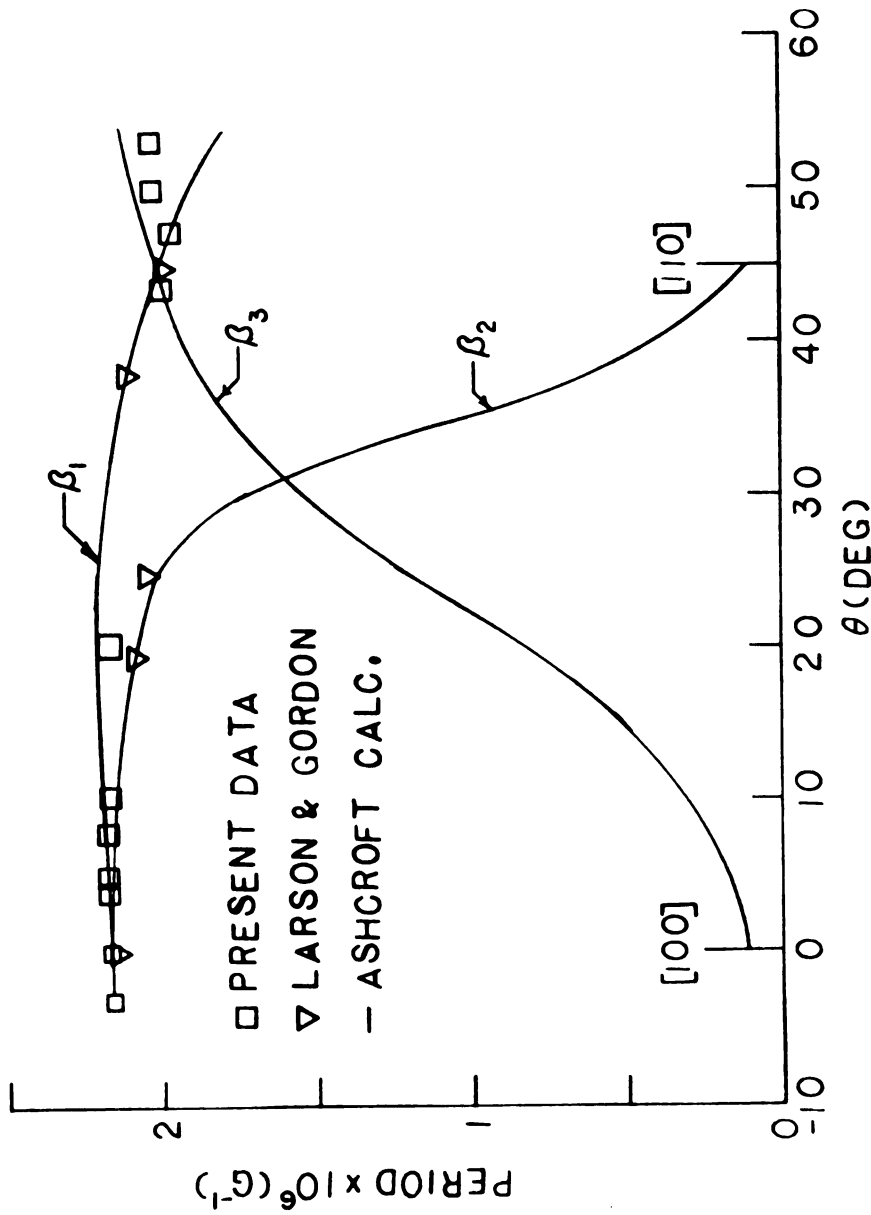


Figure VI.10: Variation of the oscillation period of the third zone  $\beta$ -orbit with rotation angle in the (001) plane. This figure displays our present magnetothermopower data, the de Haas-van Alphen data of Larson and Gordon, (32) and the results of a pseudopotential calculation by Ashcroft (63).



mutual uncertainties. It is interesting to note that the magnetothermopower oscillations for  $\theta$  between  $0^\circ$  and  $20^\circ$  appear to be due to  $\beta_1$  orbits, in contrast to the de Haas-van Alphen measurements which are sensitive to the  $\beta_2$  orbits in this range of angles.\* Thus, magnetothermopower oscillations apparently provide information regarding the shape of the Fermi surface which is complementary to that obtained from de Haas-van Alphen measurements.

If one carefully looks at the  $46^\circ$  and  $49^\circ$  oscillation patterns of Figure VI.9, one discerns a small, high frequency component above 17kG. The period of this high frequency component is  $(3.4 \pm .3) \times 10^{-7} \text{G}^{-1}$ . This is in agreement with the value  $3.5 \times 10^{-7} \text{G}^{-1}$ \*\* obtained from de Haas-van Alphen measurements<sup>(32)</sup> of the larger  $\gamma$ -orbits of the third zone Fermi surface of aluminum (see Figure V.3). We might note in passing that Bozhko and Vol'skii<sup>(70)</sup> have observed magnetoresistance oscillations with a period characteristic of the  $\gamma$  orbits of aluminum for H along the [110] axis.

---

\*The geometrical arrangement of the  $\beta_1$  orbit with respect to the  $\beta_2$  orbit is shown in Figure 5<sup>1</sup> of C.O. Larson and W. L. Gordon, Phys. Rev. 156, 703 (1967).

\*\*This frequency is actually due to the  $\gamma_1$  orbit. The geometrical arrangement of the  $\gamma_1$  with respect to the other orbits is shown in Figure 5<sup>1</sup> of C.O. Larson and W.L. Gordon, Phys. Rev. 156, 703 (1967).

### C. Indium

#### 1. Introduction

It is apparent from pseudopotential models of the Fermi surface of indium, (52,53,59,73,74) that magnetic breakdown could occur for a sufficiently large magnetic field along the [010] axis. However, until now, no experimental evidence of such breakdown has been obtained. In this section experimental data showing giant, low frequency magnetothermopower oscillations are presented. The oscillations are attributed to magnetic breakdown. This attribution is supported by a detailed comparison between the indium data and similar data for the [010] breakdown orbit in aluminum (presented in section VI.B).

Aluminum is one of only four metals (aluminum, (29-31) magnesium, (75) tin, (69,76) and zinc (47)) for which giant magnetothermopower oscillations have been observed. In all four metals, these oscillations have been attributed to magnetic breakdown. In each case, this attribution is supported by independent magnetoresistance (34,77,78) or de Haas-van Alphen (66,79) measurements and also by analysis of the known Fermi surface of the metal. Aluminum was chosen for the comparison because its electronic structure and Fermi surface are most nearly similar to those of indium.

In addition to the giant oscillations for H along [010], large, low frequency magnetothermopower oscillations

for H along  $[\bar{1}01]$  and  $[1\bar{1}0]$ , and small, medium frequency oscillations for H along  $[1\bar{1}0]$  were also observed. These low frequency oscillations are also tentatively attributed to magnetic breakdown, but the medium frequency ones are not.

## 2. Experimental Procedure

Oscillatory behavior was found in samples In-II, In(Sn)-I, In(Sn)-II, and In(Sn)-III. As the temperature was raised the oscillation amplitude fell off rapidly, becoming comparable to the measuring uncertainty at about 2.5K. Searches for oscillatory magnetothermopower were not performed on samples In-I and In(Ga); presumably these samples would have exhibited this behavior when H was aligned along the proper crystallographic axis.

The measurements were performed using the chopper-amplifier in the field sweep mode (see sections II.A.2 and II.F).

## 3. Data and Analysis

Figure VI.11 shows the output of the x-y recorder (essentially a plot of S vs H) for samples In(Sn)-I and In(Sn)-II for H along  $[\bar{1}01]$ ,  $[1\bar{1}0]$ , and  $[010]$ . No oscillations were observed for H along  $[001]$ . In Figure VI.11 four sets of oscillations are present, each periodic in  $1/H$ . The oscillation frequencies are  $1.4 \pm 0.1 \times 10^5 \text{ G}$  for H parallel to  $[\bar{1}01]$ ;  $1.55 \pm 0.1 \times 10^5 \text{ G}$  and  $4.6 \pm 0.1 \times 10^6 \text{ G}$  for H parallel to  $[1\bar{1}0]$ ; and

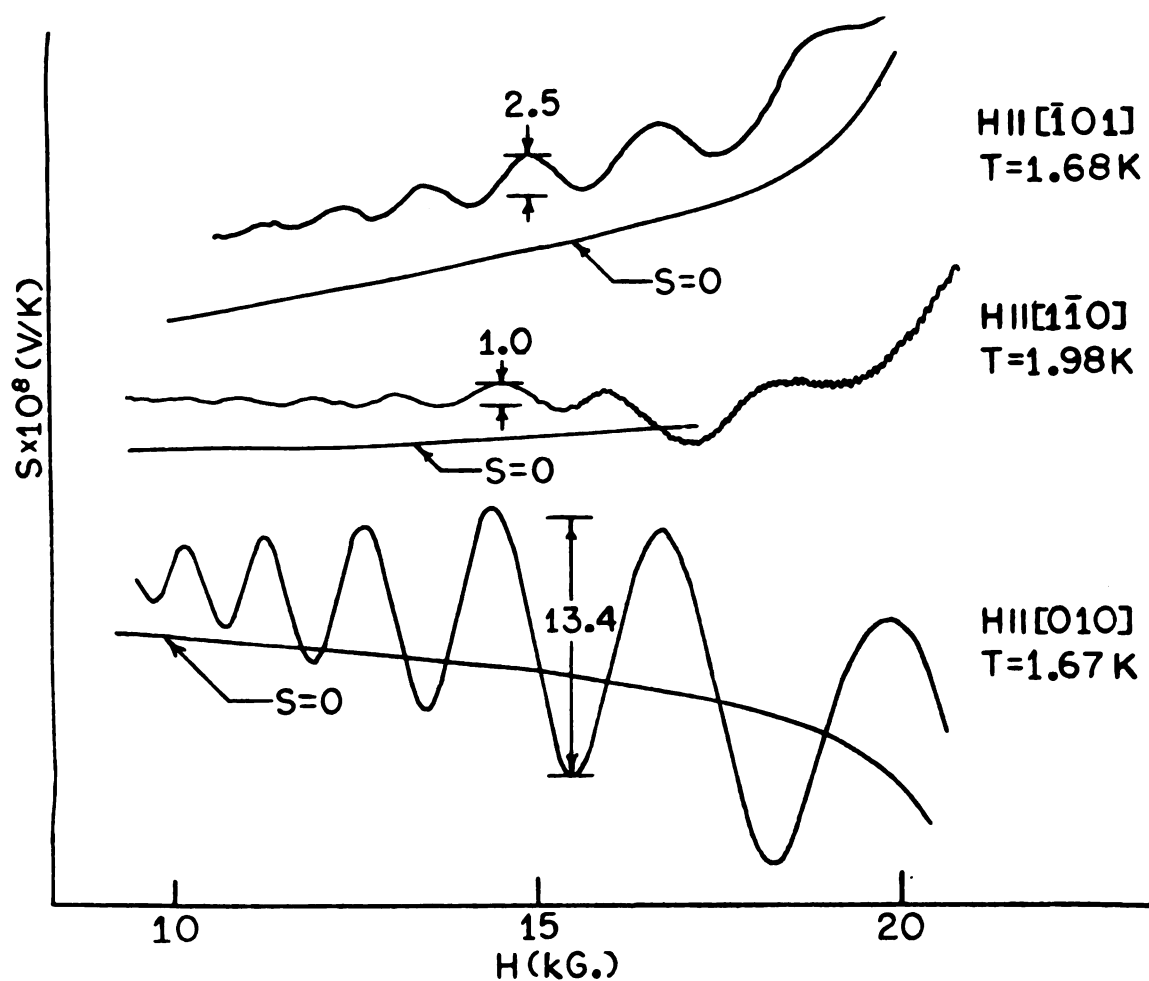


**Figure VI.11:** The magnetic field dependence of  $S$  for  $H$  aligned along the indicated crystallographic axes. The lines labeled  $S = 0$  represent the recorder output when there is no applied temperature gradient. The oscillating curves represent raw data, uncorrected for the field dependent amplification of the measuring system. The amplification decreases by about 30% over the field range shown. The curves for  $H$  aligned along  $[\bar{1}01]$  and  $[010]$  are from sample  $\text{In}(\text{Sn})\text{-I}$  and the curve for  $H$  along  $[\bar{1}\bar{1}0]$  is from sample  $\text{In}(\text{Sn})\text{-II}$ .

$1.04 \pm .04 \times 10^5 \text{ G}$  for H parallel to [010]. All four frequencies agree to within mutual uncertainties with values obtained for indium from de Haas-van Alphen<sup>(52,80)</sup> and ultrasonic absorption<sup>(81)</sup> measurements; measurements which can be understood without invoking magnetic breakdown.

In an effort to see whether the oscillation amplitudes were consistent with eq. (V.4), graphs of  $\ln(H^n S^{\text{osc}}/T)$  vs  $1/H$  with  $n = 0,1$  were plotted for H along the [010] axis. Figure VI.12 shows a typical graph. The data clearly diverge from a straight line. Thus, in contrast to aluminum, the oscillation amplitudes in indium are not consistent with eq. (V.4). The relatively small signal to noise ratio for H along either  $[\bar{1}01]$  or  $[1\bar{1}0]$  precluded any similar oscillation amplitude analysis for these directions.

Samples In-II and In(Sn)-III also exhibited oscillations for H directed along the [010] and  $[1\bar{1}0]$  axes respectively. For H along the [010] direction, the data for the purer sample In-II were similar to those for In(Sn)-I, but the oscillation amplitude was about 25% smaller for a field of about 15kG. at 1.7K. One also obtains a similar comparison with the data of the purer In(Sn)-II with those of In(Sn)-III for a magnetic field of about 15kG. directed along the  $[1\bar{1}0]$  axis at 1.9K. Therefore, it is concluded that the oscillation

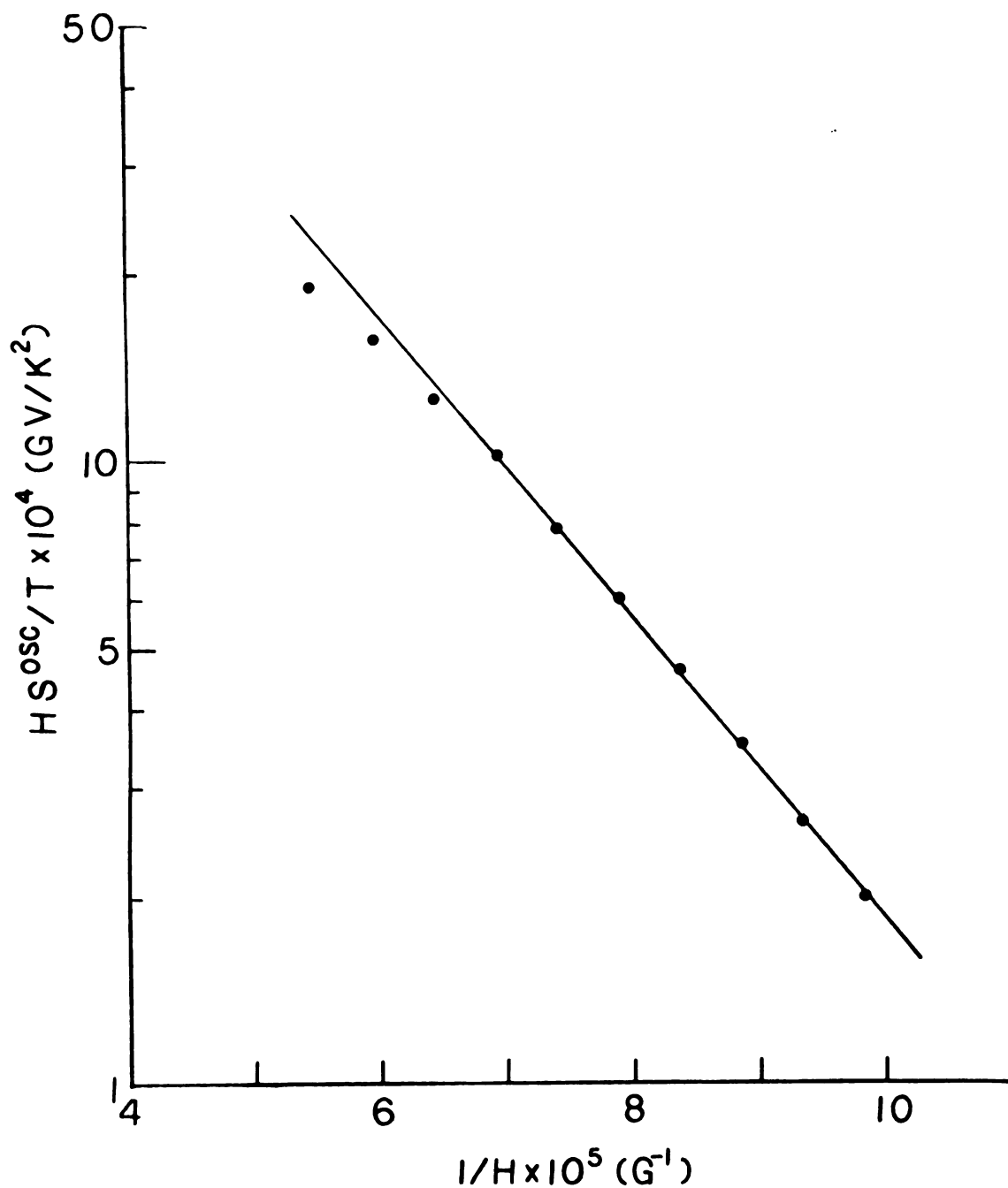


Figure VI.12: The variation of the quantity  $HS^{\text{osc}}/T$  (plotted on a logarithmic scale) with  $1/H$  for sample In(Sn)-I at  $T = 1.67\text{K}$ .  $H$  was directed along  $[010]$ .

amplitudes were limited by extended crystal lattice imperfections (mosaic structure, lattice dislocations, etc.) rather than by impurity scattering. Such a result is reasonable since indium is a very soft material which can be easily damaged.

Like aluminum, the oscillation pattern for these indium crystals were not significantly affected by  $1^\circ$  rotations of H relative to the major symmetry directions; and similarly the oscillation amplitudes gradually decreased as H was rotated away from the major symmetry directions.

The remainder of this section will concentrate on the giant oscillations for H along [010], both because these are the largest oscillations and because they can be compared directly with breakdown oscillations in aluminum for the same field orientation.

As noted earlier, electronic transport oscillations are expected to arise from either magnetic breakdown or oscillations in the density of states at  $\epsilon_F$ . Clearly, the most convincing proof that the giant thermopower oscillations which are observed are a result of magnetic breakdown would be a demonstration that their amplitude could be predicted from theory. Unfortunately, the theory of the effect of magnetic breakdown on the thermopower of metals is not sufficiently far advanced to allow direct quantitative comparison with experiment.

Therefore, the breakdown hypothesis was indirectly tested in two ways involving comparison of the indium data with similar data for the [010] breakdown orbit in aluminum.

First, the estimation of the oscillation amplitude due to the other mechanism which might cause oscillations: the variation with  $H$  of the density of states at the Fermi energy in the absence of magnetic breakdown given by eqs. (V.17) and (V.18), was compared with the experimentally measured amplitudes for both aluminum and indium. For aluminum the calculated oscillation amplitude for  $H$  along [010] was four orders of magnitude smaller than the experimental amplitude, and for indium it was three orders of magnitude smaller. Since the oscillations in aluminum result from breakdown, a discrepancy between this calculation and experiment is expected and indeed it is very large. The fact that indium also exhibits a very large discrepancy is taken as evidence in favor of magnetic breakdown in indium. The large oscillations for  $H$  parallel to  $[\bar{1}01]$  and  $[1\bar{1}0]$  are also two or more orders of magnitude larger than the calculated value of eq. (V.18),\*

---

\* In eq. V.18, the values of  $|\frac{\partial^2 A}{\partial k_H^2}|$  and  $m^*$  appropriate to  $H$  along [010] was used. Proper calculations would use the  $|\frac{\partial^2 A}{\partial k_H^2}|$  and  $m^*$  appropriate to  $H$  along either  $[\bar{1}01]$  or  $[1\bar{1}0]$ .

However, it seems unlikely that these changes will significantly reduce the discrepancy between calculation and experiment.



making them candidates for breakdown too. On the other hand, the small medium frequency oscillations for  $H$  parallel to  $[1\bar{1}0]$  are within one order of magnitude of the value predicted by this simple model, and it is therefore unnecessary to invoke breakdown to explain them.

Second, the angular variation of the thermopowers of the two indium samples was compared with that of the aluminum single crystal as  $H$  was rotated away from the  $[010]$  direction. Agreement between the forms of these two angular variations might provide additional evidence for magnetic breakdown in indium. The angular variations are shown in Figure VI.13. The field was rotated around the  $[001]$  axis of the aluminum sample and of sample In-II, and around the  $[101]$  axis of sample In(Sn)-I. Indeed, the forms of the rotation patterns are nearly the same for both aluminum and indium. Similar patterns were also obtained for rotations with  $H$  near  $[1\bar{0}1]$  and  $[1\bar{1}0]$ .

Having shown that the low frequency data can be plausibly attributed to magnetic breakdown, this section will be concluded by considering the ramifications of the presence of such breakdown for the most recent pseudopotential model of the Fermi surface of indium by Holtham.<sup>(59)</sup> For  $H$  along  $[010]$ , this model yields a breakdown field  $H_0$  in the range of 200-400kG,<sup>(57)</sup> more than an order of magnitude larger than the largest field

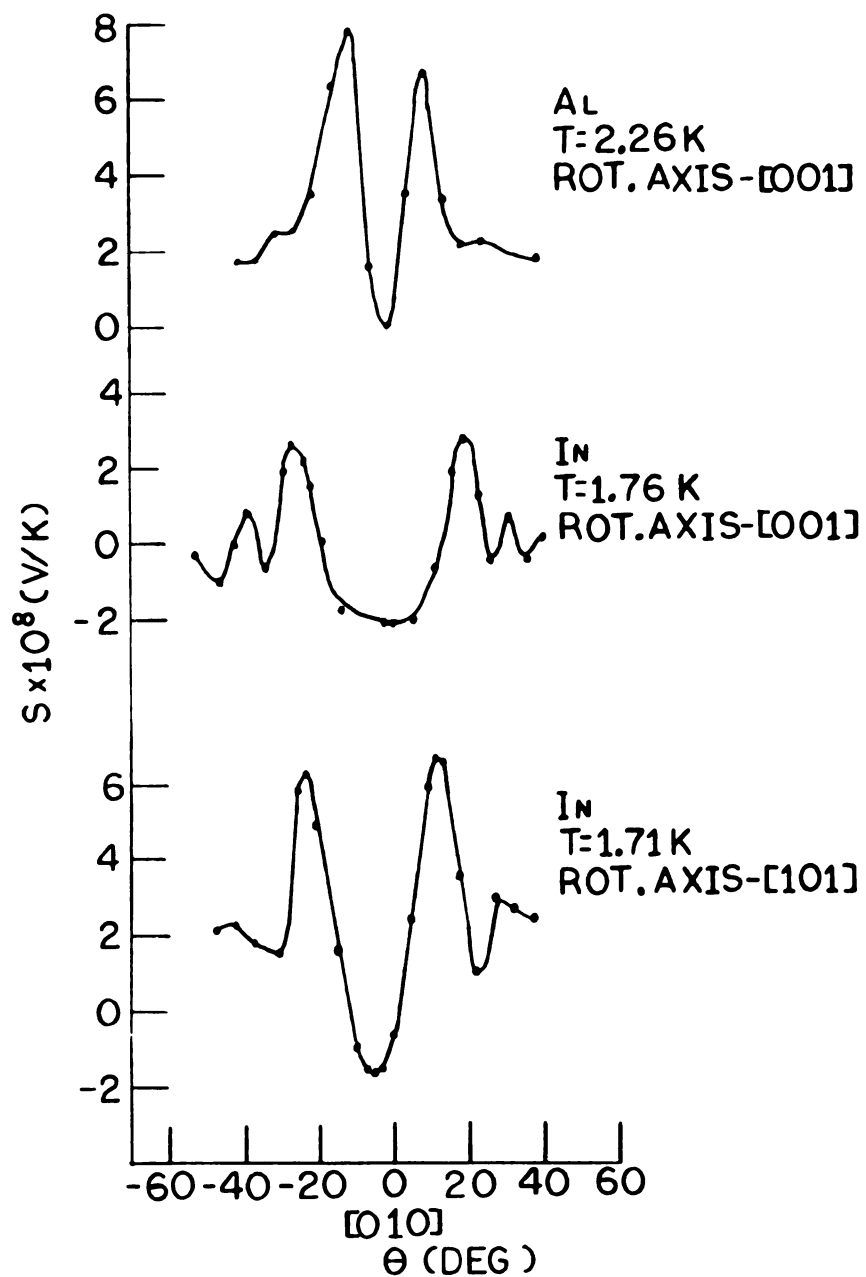


**Figure VI.13:** Variation of  $S$  with rotation angle measured from the  $[010]$  axis, at  $H = 15 \text{ kG}$  for aluminum and indium single crystals. The aluminum data are from sample Al(Ga). The indium data for  $H$  rotated about the  $[001]$  axis are from sample In-II and the data for  $H$  rotated about the  $[101]$  axis are from sample In(Sn)-I.

used here. In view of the exponential dependence of breakdown probability on the ratio  $H/H_0$ ,<sup>(64)</sup> it seems unlikely that the experiments performed in this thesis would show significant effects of breakdown for such a large  $H_0$ . The experiments suggest that  $H_0$  is roughly an order of magnitude smaller. As Holtham points out,<sup>(59)</sup> this would imply that the second and third zones are closer together than in his model.

In conclusion, large, low frequency oscillations have been found for  $H$  along the  $[010]$ ,  $[\bar{1}01]$ , and  $[1\bar{1}0]$  axes, while small, medium frequency oscillations are found for  $H$  along the  $[1\bar{1}0]$  axis. All frequencies agree to within mutual uncertainties with the values obtained by de Haas-van Alphen and ultrasonic absorption measurements on indium. Arguing by analogy with aluminum, a metal for which there is independent evidence that magnetic breakdown exists in directions where there are giant magnetothermopower oscillations, the large, low frequency oscillations are attributed to magnetic breakdown. This attribution implies that the energy gap between the second and third zones is smaller than predicted by the latest pseudopotential model of indium.<sup>(59)</sup>

To confirm the existence of magnetic breakdown in indium, it is suggested that a search for its effects on other properties be begun. Because of the apparent sensitivity of magnetothermopower oscillations to

breakdown, <sup>(29)</sup> other properties are likely to require both magnetic fields well above 20kG. and temperatures below 2.5K. This dual requirement is the probable reason for the lack of prior evidence of magnetic breakdown in indium, since measurements of less sensitive properties such as magnetoresistance have only been made at either high fields or comparably low temperatures, but not both at once.

## REFERENCES

# LIST OF REFERENCES

1. J.M. Ziman, Electrons and Phonons, (Oxford University Press, London, 1960).
2. see for example K.R. Symon, Mechanics, (Addison-Wesley Publishing Co., Inc., Reading, Massachusetts, 1960), 2nd ed., p. 408 ff.
3. R.S. Averback, Ph.D. Thesis, Michigan State University, 1971 (unpublished).
4. R.S. Averback, C.H. Stephan, and J. Bass, J. Low Temp. Phys. 12, 319 (1973).
5. R.S. Averback and D.K. Wagner, Sol. State Comm. 11, 1109 (1972).
6. R.E. Prange and L.P. Kadanoff, Phys. Rev. 134, A566 (1964).
7. R.S. Sorbello, J. Phys. F: Metal Phys. 4, 1665 (1974).
8. J.L. Opsal and D.K. Wagner, J. Phys. F: Metal Phys. 6, 2323 (1976).
9. H.A. Fairbank and J. Wilks, Proc. Roy. Soc. (London) A231, 545 (1955).
10. J.A. Rayne, Aust. J. Phys. 9, 189 (1956).
11. A.C. Anderson, Rev. Sci. Instr. 39, 605 (1968).
12. T.J. Tiedema, Acta Crystallogr. 2, 261 (1949).
13. G.K. Williamson and R.E. Smallman, Acta Met. 1, 487 (1953).
14. J. Bass and J.L. Opsal, Proceedings of European Study Conference on the Transport Properties of Normal Metals and Alloys Well Below  $\theta_D$  (to be published).

15. C. Kittel, Introduction to Solid State Physics (Wiley, Inc., New York, 1971), 4th ed., p. 210-1.
16. A.A. Abrikosov, Introduction to the Theory of Normal Metals (Academic Press, New York, 1972).
17. J.L. Opsal, B.J. Thaler, and J. Bass, Phys. Rev. Lett. 36, 1211 (1976).
18. S.K. Lyo, Phys. Rev. Lett. 39, 363 (1977).
19. G. Grimvall, Physica Scripta (Sweden) 14, 63 (1976).
20. T. Holstein, Ann. Phys. 29, 410 (1964).
21. D.K.C. MacDonald, Thermoelectricity: an introduction to the Principles (Wiley, Inc., New York, 1962).
22. I.I. Hanna and E.H. Sondheimer, Proc. Roy. Soc. (London) A239, 247 (1957).
23. R.D. Barnard, Thermoelectricity in Metals and Alloys (Taylor and Francis Ltd., London, 1972), p. 132.
24. M. Bailyn, Phys. Rev. 157, 480 (1967).
25. J.M. Ziman, Adv. Phys. 10, 1 (1961).
26. R.J. Griphover, J.B. Van Zytveld, and J. Bass, Phys. Rev. 163, 598 (1967).
27. R.S. Blewer, N.H. Zebouni, and C.G. Genier, Phys. Rev. 174, 700 (1968).
28. J.L. Opsal, to be published.
29. W. Kesternich and C. Papastaikoudis, Phys. Stat. Solidi 64, K41 (1974).
30. N.N. Sirota, V.I. Gostishchev, and A.A. Drozd Dokl. Akad. Nauk, SSSR 220, 818 (1975). (English translation: Sov. Phys.-Dokl. 20, 116 (1975).)
31. B.J. Thaler and J. Bass, J. Phys. F: Metal Phys. 5, 1554 (1975).
32. C.O. Larson and W.L. Gordon, Phys. Rev. 156, 703 (1967).
33. D.A. Dicke and B.A. Green, Phys. Rev. 153, 800 (1967).

34. R.J. Blacombe and R.A. Parker, Phil. Mag. 21, 533 (1970).
35. R. Fletcher, J.L. Opsal, B.J. Thaler, J. Phys. F: Metal Phys. (in press).
36. W.B. Willot, Phil. Mag. 16, 691 (1967).
37. P.E. Nielson and P.L. Taylor, Phys. Rev. Lett. 21, 893 (1968).
38. A.D. Caplin, C.K. Chiang, J. Tracy, and P.A. Schroeder, Phys. Stat. Solidi 26A, 497 (1974).
39. R.S. Averback and J. Bass, Phys. Rev. Lett. 26, 882 (1971).
40. R.S. Averback and J. Bass, Phys. Rev. Lett. 34, 631 (1975).
41. F.J. Blatt, A. Burmester, and B. LaRoy, Phys. Rev. 155, 611 (1967).
42. A.R. DeVroomen, C. Van Baarle, A.J. Cuelenaere, Physica (Utrecht) 26, 19 (1960).
43. N.E. Adams and T.D. Holstein, J. Phys. Chem. Solids 10, 254 (1959).
44. see for example J.M. Ziman, Principles of the Theory of Solids (Cambridge University Press, New York, 1972), 2nd ed.
45. G.E. Zil'bermann, Zh. Exp. Teor. Fiz, 29, 762 (1955). (English translation: Sov. Phys.-JETP 2, 650 (1956).)
46. P.B. Horton, Ph.D. Thesis, Louisiana State University, 1964 (unpublished).
47. C.G. Grenier, J.M. Reynolds, N.H. Zebouni, Phys. Rev. 129, 1088 (1963).
48. J.R. Long, C.G. Grenier, and J.M. Reynolds, Phys. Rev. 140, A187 (1965).
49. A.H. Wilson, Theory of Metals (Cambridge University Press, New York, 1953), 2nd ed.
50. B.J. Thaler, R. Fletcher, and J. Bass, J. Phys. F: Metal Phys. (in press).



51. M.G. Priestley, Phil. Mag. 7, 1205 (1962).
52. A.J. Hughes and J.P.G. Shepherd, J. Phys. C: Solid St. Phys. 2, 661 (1969).
53. J.H.P. vanWeeren and J.R. Anderson, J. Phys. F: Metal Phys. 3, 2109 (1973).
54. I.M. Lifshitz and A.M. Kosevich, Zh. Exp. Teor. Fiz. 29, 730 (1955). (English translation: Sov. Phys.-JETP 2, 636 (1956).)
55. A.V. Gold, Solid State Physics: Electrons in Metals, Ed. J.F. Cochran and R.R. Haering (Gordon and Breach, New York, 1968), v.1, p. 39.
56. R.B. Dingle, Proc. Roy. Soc. (London) A211, 517 (1952).
57. P.M. Holtham, private communication.
58. This is an estimate (expected to be slightly high) based on Holtham's calculated value for  $m^*$ .<sup>(59)</sup> Holtham's calculation neglects the electron-phonon mass enhancement.
59. P.M. Holtham, J. Phys. F: Metal Phys. 6, 1457 (1976).
60. R.W. Stark and L.M. Falicov, Progress in Low Temperature Physics, Ed. C.J. Gorter (North-Holland Publishing Co., Amsterdam, 1967), v. 5, p. 235.
61. J.M. Ziman, Principles of the Theory of Solids (Cambridge University Press, New York, 1972), 2nd ed., p. 327.
62. J.C. Abele and F.J. Blatt, Phys. Rev. B1, 1298, (1970).
63. N.W. Ashcroft, Phil. Mag. 8, 2055 (1963).
64. A.B. Pippard, Proc. Roy. Soc. (London) A287, 165 (1965).
65. L.M. Falicov and H. Stachowiak, Phys. Rev. 147, 505 (1966).
66. M.G. Priestly, L.M. Falicov, and G. Weisz, Phys. Rev. 131, 617 (1963).
67. A.B. Pippard, Phil. Trans. Roy. Soc. (London) A256, 317 (1964).

68. R.C. Young, J. Phys. C: Solid St. Phys. 4, 458 (1971).
69. R.C. Young, J. Phys. F: Metal Phys. 3, 721 (1973).
70. V.I. Bozhko and E.P. Vol'skii, Zh. Exp. Teor. Fiz. 20, 703 (1974). (English translation: JETP Lett. 20, 325 (1974).)
71. N.W. Ashcroft and J.W. Wilkins, Phys. Lett. 14, 285 (1965).
72. A.B. Meador and W.E. Lawrence, Phys. Rev. B15, 1850 (1977).
73. N.W. Ashcroft and W.E. Lawrence, Phys. Rev. 175, 938 (1968).
74. W.J. O'Sullivan, J.E. Schirber, and J.R. Anderson, Phys. Lett. 27A, 144 (1968).
75. C. Papastaikoudis and W. Kesternich, J. Low Temp. Phys. 21, 517 (1975).
76. J.A. Woolam and P.A. Schroeder, Phys. Rev. Lett. 21, 81 (1968).
77. R.W. Stark, Proc. IX<sup>th</sup> Int. Conf. Low Temperature Physics, Ohio 1964 (Plenum Press, New York, 1965), p. 712.
78. R.C. Young, J. Phys. C: Solid St. Phys. 4, 474 (1974).
79. F.A. Buot, P.L. Li, and J.O. Strom-Olsen, J. Low Temp. Phys. 22, 535 (1976).
80. G.B. Brandt and J.A. Rayne, Phys. Rev. 132, 1512 (1963).
81. J.E. Cowey, R. Gerber, and L. Mackinnon, J. Phys. F: Metal Phys. 4, 39 (1974).
82. R.S. Sorbello, private communication.
83. E.M. Purcell, Electricity and Magnetism (McGraw-Hill, New York, 1964), p. 55.

## **APPENDICES**

## APPENDIX I

### CALCULATION OF ANISOTROPY OF $\tau(\vec{k})$ FOR Al(Ga)

We will use Sorbello's approximate phase shift model<sup>(7)</sup> to calculate the anisotropy of  $\tau(\vec{k})$  of Al(Ga). Within the Born approximation ( $\delta_\ell \ll \pi$ ) the average value of  $1/\tau_0(\vec{k})$  around an orbit on the Fermi surface,  $\langle 1/\tau_0(\vec{k}) \rangle$ , may be written

$$\langle 1/\tau_0(\vec{k}) \rangle = \frac{4\pi c\hbar}{mk_F\Omega_0} \sum_{\ell=0}^{\infty} (2\ell + 1) (\delta_\ell^{\text{BA}})^2 \langle F_\ell(\vec{k}) \rangle \quad (\text{AI.1})$$

$\delta_\ell^{\text{BA}}$  are the phase shifts obtained from the Born approximation, and depend only on the impurity scattering potential. The quantity  $F_\ell(\vec{k})$ , called the "amplitude factor", measures the square of the magnitude of the  $\ell$  component of  $\phi_{\vec{k}}(\vec{r})$  ( $\phi_{\vec{k}}(\vec{r})$  is the pseudowavefunction associated with the Bloch state  $\vec{k}$ ) when  $\phi_{\vec{k}}(\vec{r})$  is expanded in spherical harmonics about a lattice site. In the free electron (F.E.) approximation  $F_\ell(\vec{k}) \equiv 1$  for all  $\ell$ .

Using the  $\delta_\ell^{\text{BA}}$  obtained from the Heine-Abarenkov-Animalu form factors in the Born approximation, which are given in Sorbello's table 1; and the average amplitude factors  $\langle F_\ell(\vec{k}) \rangle$  for orbits on the Fermi surface of

aluminum, which are given in Sorbello's table 3, we can calculate the ratio  $\langle 1/\tau_0(\vec{k}) \rangle / (1/\tau_0)_{F.E.}$  for Al(Ga). Table AI-1 shows the results for the third zone  $\gamma$ ,  $\alpha$ ,  $\beta$  and orbits and second zone [110] orbit on the Fermi surface of aluminum.

Table AI-1: Average reciprocal relaxation times for Al(Ga) obtained from Sorbello's approximate phase shift model<sup>(7)</sup>

	ORBIT			
	$\gamma$	$\alpha$	$\beta$	[110]
$\langle 1/\tau_0 \rangle / (1/\tau_0)_{F.E.}$	1.10	1.10	1.19	1.08

Table AI-1 shows that the average reciprocal relaxation times of the third zone of Al(Ga) are isotropic to within 10%. Sorbello also claims that the average reciprocal relaxation times of the second zone should be more isotropic than the third zone times.<sup>(82)</sup> Therefore from table AI-1 it is concluded that the average relaxation time is nearly isotropic (to within an accuracy of about 10%) over the entire Fermi surface (which only consists of second and third zone pieces) of dilute Al(Ga) alloys.

APPENDIX II  
DETERMINATION OF  $\frac{\partial \sigma(\epsilon)}{\partial \epsilon}$

From eq. (III.31a) we see that

$$\sigma_{ij}(\epsilon) = \frac{e^2}{4\pi^2\hbar} \int_{S(\epsilon)} dS \frac{v_i}{v} \tau v_j,$$

which may be rewritten as

$$\sigma_{ij}(\epsilon) = \frac{e^2}{4\pi^2\hbar} \int_{S(\epsilon)} dS \frac{\vec{v}}{v} \cdot \hat{e}_i \tau v_j, \quad (\text{AII.1})$$

where  $\hat{e}_i$  is a unit vector in the  $i^{\text{th}}$  direction. Applying the divergence theorem <sup>(83)</sup> to eq. (AII.1) gives

$$\begin{aligned} \sigma_{ij}(\epsilon) &= \frac{e^2}{4\pi^2\hbar} \int d^3\vec{k} \vec{v}_k \cdot (\hat{e}_i \tau v_j) \\ &= \frac{e^2}{4\pi^2\hbar} \int_0^\epsilon d\epsilon' \int_{S(\epsilon')} \frac{dS}{\hbar v} \vec{v}_k \cdot (\hat{e}_i \tau v_j). \end{aligned} \quad (\text{AII.2})$$

So it follows that

$$\frac{\partial \sigma_{ij}(\epsilon)}{\partial \epsilon} = \frac{e^2}{4\pi^2\hbar} \int_{S(\epsilon)} \frac{dS}{\hbar v} \vec{v}_k \cdot (\hat{e}_i \tau v_j). \quad (\text{AII.3})$$

We recognize that  $\vec{v} \cdot (\hat{e}_i \tau v_j) = [\vec{v}(\tau \vec{v})]_{ij}$  so

$$\frac{\partial \sigma_{ij}(\epsilon)}{\partial \epsilon} = \frac{e^2}{4\pi^2\hbar} \int_{S(\epsilon)} \frac{dS}{\hbar v} [\vec{v}_k(\tau \vec{v})]_{ij}. \quad (\text{AII.4})$$

For cubic symmetry eq. (AII.4) becomes

$$\frac{\partial \sigma(\epsilon)}{\partial \epsilon} = \frac{e^2}{12\pi^2 \hbar} \int_{S(\epsilon)} \frac{dS}{hv} \vec{v}_k \cdot (\tau \vec{v}). \quad (\text{AII.5})$$





